UNIVERSITY OF CALIFORNIA

Santa Barbara

Band Engineering of Epitaxial Semimetal Films

A dissertation submitted in partial satisfaction of the

requirements for the degree Doctor of Philosophy

in Materials

by

Hadass S. Inbar

Committee in charge:

Professor Chris J. Palmstrøm, Chair

Professor Ram Seshadri

Professor John W. Harter

Professor Ania C. Bleszynski Jayich

December 2023

The dissertation of Hadass S. Inbar is approved.

_____

Professor Ram Seshadri

_____

Professor Ania C. Bleszynski Jayich

_____

Professor John W. Harter

_____

Professor Chris J. Palmstrøm, Committee Chair

October 2023

Band Engineering of Epitaxial Semimetal Films

ACKNOWLEDGEMENTS

The completion of this work would not have been possible without the help and support of many, many people. First and foremost, I would like to acknowledge my advisor, Prof. Chris Palmstrøm. He has taught me so much about vacuum science and technology, often leading by example. Thank you for all your guidance, but also for believing in me and giving me the academic freedom to explore new research directions and career paths. I would like to thank my other doctoral committee members, Prof. Ram Seshadri, Prof. Ania Bleszynski Jayich, and Prof. John Harter all of whom have given me valuable advice throughout my PhD and offered practical suggestions for new experiments to consider. Their questions helped me understand better the fundamental physical behavior of the systems I was studying.

I have told every prospective graduate student interested in UCSB that one of the main reasons I joined the Palmstrøm lab was because of the group members. Though working on ultrahigh vacuum equipment is tough physically and mentally, I've learned that as a team, even arduous tasks were manageable and eventually made for many good memories from graduate school. I would like to thank past and present Palmstrøm lab members: Aaron, Alex, Aranya, Collin, Connor, Dan P., Dan R., Elliot, Jason D., Joon Sue, Max, Michael, Mihir, Paul, Sean, Shinichi, Shouvik, Sukgeun, Taozhi (George), Teun, Tobias, Tony and Wilson. Specifically, I would like to thank Mihir and Shouvik for being very knowledgeable and supportive mentors I was fortunate to have. They have taught me how to grow, measure devices, and perform ARPES measurements. Mihir, thank you for all the years you have dedicated to building excellent team dynamics and for training me and other generations in the Palmstrom lab on a wide range of topics. I appreciate your continuing support also well after graduating from

UCSB, and of course all the fun memories goofing around in the lab. Shouvik, I owe you much of my professional development, scientific approach and progress in research. Thank you for helping me find a balance between research focus, data analysis and design of experiments and MBE upkeep responsibilities. I have also learned so much from other senior and junior lab members including Aaron, Connor, Dan, Jason, Sean, Tobias, and Tony.

Much of the computational work in this thesis has been accomplished through close collaboration with Prof. Anderson Janotti's group at the University of Delaware: Dai Ho, Muhammad Zubair, and Shoaib Khalid. Their DFT calculations provided valuable insight into the electronic properties of the materials we were studying. I am also very grateful for the opportunity to work in synchrotron facilities during my PhD. I would like to thank beamline staff scientists at ALS (Alexei Fedorov) and SLAC (Makoto Hashimoto and Donghui Lu) for all their effort and work leading up to our beamtime experiments.

UCSB's MBE community has given me a great chance to learn about epitaxy in other materials systems. I hope this collaborative atmosphere inspired by the ex-Bell Labs founding groups will live on and that we will build on the amazing institutional knowledge present at UCSB. I would like to thank Kurt Olsson and John English for all their help and advice while tackling my experimental challenges. I would like to thank Doug Rehn at the UCSB Physics Machine Shop for all his clever solutions to UHV hardware issues.

I would also like to thank my funding sources throughout my PhD: the Department of Energy, Office of Naval Research, and the Quantum Foundry (National Science Foundation). In particular, I would like to thank the Quantum Foundry research groups and staff for enriching my PhD journey with new learnings and collaborations.

As I navigated my graduate studies and career goals, I learned an important lesson: the strength of close friends and family. I would like to thank my friends in Israel and Santa Barbara for their support and for adding balance to my life. The love and encouragement of my parents and in-laws, siblings (with my amazing sister Daphne also defending her PhD this year), and husband Ohad have made me stronger and helped me prioritize my physical and mental health. Ohad, I am fortunate to be married to such an intelligent and supportive man who would go to great lengths to move across the world with me. You have read (and understood!) all my papers, given me feedback on presentations, accepted all the late nights and long weekends away from home, and helped me become a better scientist. Finally, I would like to thank my daughter Noga. Though you are only 4-months-old you have waited patiently for your due date while I wrote this thesis and defended my PhD. You have already taught me so much, brought me so much joy, and helped me gain a whole new improved perspective on life.

Curriculum Vitae

Hadass S. Inbar

EDUCATION

PhD in Materials with specialization in electronic & photonic materials, 2023
University of California, Santa Barbara
Advisor: Christopher J. Palmstrøm

BSc in Materials Science and Engineering & BSc in Chemistry, 2017
Technion - Israel Institute of Technology, Haifa, Israel

PROFESSIONAL EMPLOYMENT

11/2021-05/2022: R&D Engineering Intern
PsiQuantum, Palo Alto, CA

09/2017 – 10/2023: Graduate Student Researcher
University of California Santa Barbara, Santa Barbara, CA

SELECT PUBLICATIONS

Inbar, H. S., Ho, D. Q., Chatterjee, S., Pendharkar, M., Engel, A. N., Dong, J. T., ... & Palmstrøm, C. J. (2022). Epitaxial growth, magnetoresistance, and electronic band structure of GdSb magnetic semimetal films. *Physical Review Materials*, *6*(12), L121201.

Inbar, H. S., Ho, D. Q., Chatterjee, S., Engel, A. N., Khalid, S., Dempsey, C. P., ... & Palmstrøm, C. J. (2022). Tuning the Band Topology of GdSb by Epitaxial Strain. APL Materials (in press) 10.1063/5.0155218 *arXiv preprint arXiv:2211.15806*.

Inbar, H. S., Zubair, M., Dong, J. T., Engel, A. N., Dempsey, C. P., Chang, Y. H., ... & Palmstrøm, C. J. (2023). Inversion Symmetry Breaking in Epitaxial Ultrathin Bi (111) Films. *arXiv preprint arXiv:2302.00803*.

SELECT AWARDS

- 2020-Present: NSF Quantum Foundry Graduate Associate (2020-2021) and Fellow (2021-Present)
- 2020: Young Scientist Award, 47th Conference on Physics & Chemistry of Surfaces & Interfaces
- 2017: SPIE Optics and Photonics Education Scholarship
- 2017: Shenkar Award for best poster presentation, MSE departmental undergraduate poster competition, Technion
- 2015-2016, 2013-2014, and 2012-2013: President's Award for Excellence and Schulich Award for top 3% in MSE and Chemistry Departments (respectively), Technion

Abstract

Band Engineering of Epitaxial Semimetal Films

by

Hadass S. Inbar

This dissertation explores epitaxial growth and modifications to the electronic band structure of topological semimetal materials through heteroepitaxy, biaxial strain, and reduced dimensionality. High-quality thin films are grown via molecular beam epitaxy (MBE) and studied using a combination of angle-resolved photoemission spectroscopy (ARPES), density functional theory (DFT), and low-temperature magnetotransport.

Recent predictions of topological phases and observations of extremely large magnetoresistance in the class of rare-earth monopnictides, and specifically GdSb, have opened up a new research front aimed at studying the interplay between magnetoresistance, topology, and magnetic ordering. The first part of the dissertation focuses on magnetoresistance and band topology evolution in lattice-matched and biaxially strained GdSb (001) thin films. Lattice-matched GdSb films show a mobility and carrier concentration imbalance, deviating from the commonly assumed compensated charge carrier densities seen in bulk rare-earth monopnictides. Next, we established a clear connection between biaxial strain in GdSb films and the affected band dispersions based on their orbital composition. As

biaxial strain is tuned from tensile to compressive strain, the gap between the hole and the electron bands dispersed along [001] decreases.

The second part of this dissertation reports the first ARPES investigation conclusively assigning the topological character of bismuth as a trivial $\mathbb{Z}_2$ state by studying ultrathin Bi (111) films grown on InSb (111)B. Bismuth films hold promise for potential applications in spintronic devices and topological one-dimensional edge transport. Yet synthesizing high-quality, wafer-scale ultrathin bismuth films on non-metallic substrates remains challenging. We achieved large-area Bi (111) films with a single epitaxial domain orientation and mapped the dispersion of surface states and quantum well states. Strong film-substrate interactions were found to promote epitaxial stabilization of the (111) orientation and lead to inversion symmetry breaking. Our results demonstrate that interfacial bonds prevent the semimetal-to-semiconductor transition predicted for freestanding bismuth layers, highlighting the importance of controlled functionalization and surface passivation in two-dimensional materials.

Finally, the growth parameters of biaxially strained LuPtBi films on InSb were explored. The half-Heusler compound LuPtBi belongs to a unique group of superconductors with a topologically nontrivial band structure, and very low carrier densities ($<10^{20}$ cm^{-3}). A suitable growth window could not be identified for (111) oriented LuPtBi. Room-temperature nucleation of LuPtBi on LuPtSb/InSb (001) allowed higher incorporation of Bi in LuPtBi and produced smooth, coherently strained films.

Table of Contents

1 Introduction

1.1 Topological materials: discovery, synthesis, and applications

In 2016, the Nobel Prize in physics was awarded to David J. Thouless, F. Duncan M. Haldane, and J. Michael Kosterlitz for theoretical discoveries of topological phase transitions and topological phases of matter. Topology is a mathematics branch that studies the properties and relationships of objects and spaces, particularly concerning their continuity and connectivity. The topological classification of insulators/semimetals depends on the symmetry preserved (time-reversal, crystalline symmetry, rotation, inversion symmetry, etc.) and the type of band inversion (even/odd parity) or band crossing (accidental degenerate points, mirror planes, high symmetry points, etc.) [1]. In the case of topological insulators, one of the first classes of three-dimensional (3D) topological materials studied theoretically [2–4] and experimentally [5], the topological classification is given by the $\mathbb{Z}_2$ topological invariant [2].

A topological invariant is a quantity that does not change under continuous deformation (see Figure 1.1A) unless a topological phase transition occurs. For example, the passage from an even to an odd band parity at the highest occupied band in Figure 1.1B used to calculate the $\mathbb{Z}_2$ invariant is considered a topological quantum phase transition [6]. The $\mathbb{Z}_2$ topological invariant in an inversion-symmetric material preserving time-reversal symmetry is evaluated from the product over $\xi_m(\Lambda_i) = \pm 1$, the parity eigenvalue of the m occupied energy band at the time-reversal invariant momenta (TRIM) point Λ_i [4]:

$$\delta_i = \prod_m \xi_m(\Lambda_i)$$

In a 3D topological insulator, the strong topological index, v_0, and weak indices (v_1, v_2, v_3) are calculated from the product of all δ_i:

$$(-1)^{v_0} = \prod_{n_j=0,1} \delta_{n1n2n3} \qquad (-1)^{v_{i=1,2,3}} = \prod_{n_j=0,1} \delta_{n1n2n3}$$

Where $v_0 = 1$ yields a strong topological insulator phase which should host an odd number of surface state band crossings between two surface TRIMs. These surface states should remain robust against non-magnetic perturbations. For v_0 =0, $v_i = 1$, $i = 1,2,3$ a weak topological insulator phase is obtained and v_i =0 $i = 0,1,2,3$ results in an ordinary insulator phase.

One can draw an analogy between the $\mathbb{Z}_2$ invariant and other geometric topological invariants by examining the possible structures shown in Figure 1.1A. Each object cannot be continuously deformed into the next item without abruptly popping a new hole. Similarly, a material with a nontrivial inverted band structure (Figure 1.1B) cannot be transformed into a trivial band order (that is present in vacuum or any other trivial 'ordinary' insulator) without an abrupt transition, which takes place at the boundaries of the topological material. The sharp transition at the outer limits of a topological material leads to the formation of protected metallic surface/edge states at that critical point. Since these metallic boundaries originate from the topological invariant, they are called topological surface or edge states (TSS/TES), and unlike normal surface states that form at the surfaces of a trivial band-order material, the TSS/TES arise from the bulk structure and cannot be eliminated by nonmagnetic perturbations. The spin-momentum locking of topological surface states in a 3D topological insulator and exotic transport characteristics of topological semimetals due to the relativistic nature of charge carriers hold great promise for applications in spintronic devices [7,8], for example in efficient spin generation and spin-charge conversion.

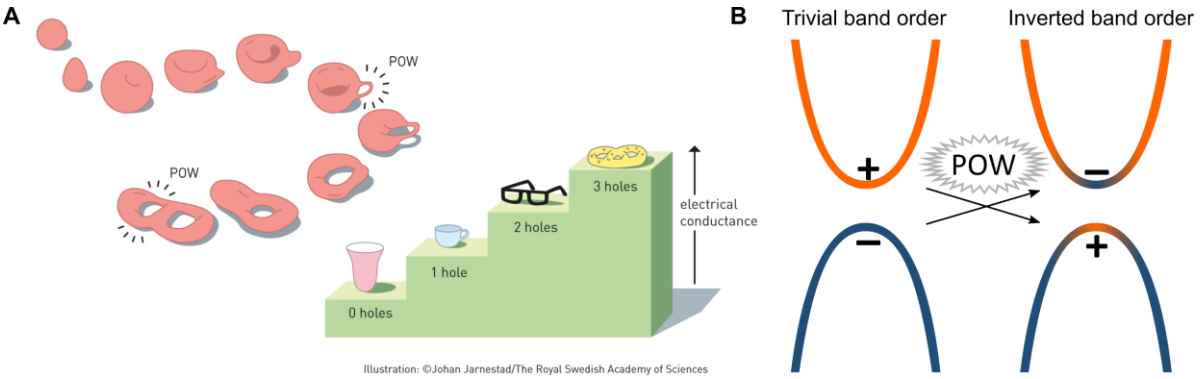

Figure 1.1. (A) An illustration of topological transitions between surfaces differing by their genus, a topological invariant that counts the number of holes. Quantized Hall conductivity in the integer quantum Hall effect arises from the Chern topological invariant (analogous to the number of holes), distinguishing the quantum Hall state from the band insulating state. Adapted from [9] (B) Schematic of a topological phase transition in a material's electronic band structure. Two bands swap the order of their orbital characters and parity, resulting in band inversion.

Bi_xSb_{1-x} [5] and Bi_2Se_3 [10] were the early 3D topological insulators to be experimentally verified using angle-resolved photoemission spectroscopy (ARPES). The accelerated timeline in the experimental discovery of new topologically nontrivial compounds owes much of its progress to ARPES as the technique of choice in identifying new topological materials [11]. One of the main reasons ARPES has proven to be a very useful tool in the early exploration of a material's electronic structure is the ability to directly interpret a material's band structure with minimal use of *ab-initio* calculations if one relies instead on principles from band topology. Moreover, in ARPES it is possible to discern surface states from bulk bands and resolve spin polarization. Besides ARPES, alternative techniques are also used to explore topological materials, such as the study of nonlinear optical response [12], quasiparticle interference patterns [13], and magnetotransport characteristics [14].

In recent years it was found that topological materials are surprisingly ubiquitous [15,16], and their various categories and applications have been studied extensively for the past two decades. Topological antiferromagnets are one such class, where the coupling between antiferromagnetic order and relativistic quasiparticles offers new possibilities to control the

symmetry of topological states and their spin-polarized currents by manipulating the magnetization orientation [17,18]. New spin-orbitronic devices based on current-induced Néel spin-orbit torques could dissipate less energy and perform at high switching rates [19]. Applications of antiferromagnetic topological crystals and magnetic topological heterostructures include spin valves [20,21], THz photodetectors [22–24], and recent studies are also exploring the design of heterogeneous catalysts leveraging the robust metallic surface states and spin polarization in electron transfer reactions [25–27].

The synthesis of topological materials as epitaxial thin films is desirable both for device applications and for studying their physics and engineering electronic properties. For example, heterostructure designs have been studied for interfacing superconductors or ferromagnets with topological materials [28]. In this dissertation, we address one significant degree of freedom influencing the electronic structure of topological materials prepared as thin films: epitaxial strain. Strain engineering of low-dimensional topological quantum materials serves as a powerful approach to manipulating electronic band structures, thereby controlling topological phase transitions and transport behavior [29]. For example, strained HgTe quantum wells grown in the tensile and compressive regimes were shown to transition from a semimetallic to a two-dimensional topological insulator (TI) system, respectively [30]. Despite the promise of topological state tuning, strain studies of quantum materials thin films are typically restricted either to local, defect-induced strain gradients [31–33] or to strain levels below 1% strain [34,35] in the case of uniform strain in lattice-mismatched growths. In TIs such as the group V-chalcogenides (X_2Z_3, X=Bi, Sb; Z=Te, Se), unstrained growths occur even on substrates with high lattice mismatch due to the low bonding energies between van der Waals layers [28,36]. In addition to the challenge of stabilizing highly strained pseudomorphic

topological materials, visualizing the band structure modifications as a function of strain/pressure has been difficult in both bulk single crystals and thin films. In bulk single crystals, large pressure cells are difficult to implement, and when using mechanical strain tuning apparatus, special care is needed to ensure the application of uniform strain [37–40]. For thin films, there are limited reports combining strained film growth with direct spectroscopic tools such as ARPES, with a few exceptions in oxide films [41,42].

1.2 Rare earth monopnictides

Rare-earth monopnictides (RE-Vs) are a class of semimetals (or semiconductors in the case of RE-N) that are composed of the lanthanide series (and Sc and Y due to the high similarities) and group-V elements (Figure 1.2). Unlike most elemental metals which tend to react with III-Vs, in RE-Vs the wide range of lattice constants, high thermodynamic stability, and the similarity of the rocksalt structure of RE-Vs with zincblende III-V semiconductors allows epitaxial incorporation and processing into scalable devices [43–45]. The growth of RE-V on III-Vs proceeds as embedded nanoparticle [46], or as thin films [47] depending on the RE-III-V flux conditions and temperature window. RE-V thin films are typically synthesized via molecular beam epitaxy growth due to the high oxidation tendency of the lanthanide elements requiring ultrahigh-vacuum conditions to avoid unintentional rare-earth oxides.

RE-V thin films and embedded particles can be integrated with III-V semiconductors [43,47,48] and in bulk crystals were shown to present nontrivial topology (see Figure 1.3A-B) [49], extreme magnetoresistance (XMR) (Figure 1.3C-E) [50], Fermi arcs [51], and unique magnetic phase diagrams [52] due to strong *p-f* and *d-f* electron coupling. Coupled to III-Vs, RE-Vs have potential device applications, including buried metallic

contacts, THz emitters and detectors, thermoelectrics, plasmonic heterostructures, and specifically for Heusler compounds, they perform as excellent diffusion barriers [45]. III-V/RE-V magnetoresistive hybrid structures could utilize the geometric contribution to the extraordinary magnetoresistance found in high-mobility III-V–metal interfaces [53] and the tunability of conductivity in RE-Vs to optimize the heterostructure material parameters [54].

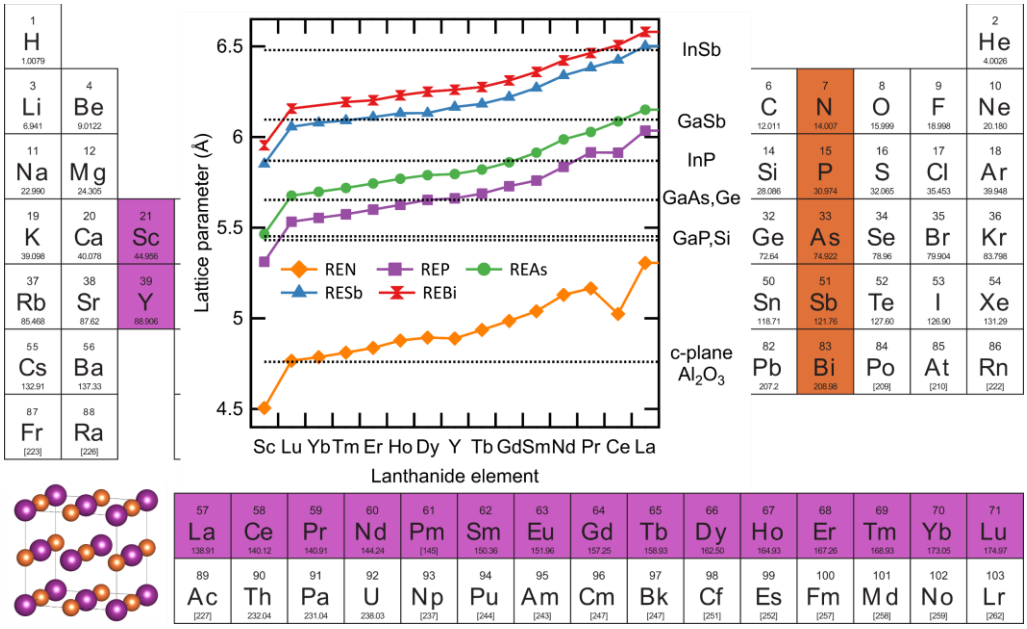

Figure 1.2. A periodic table highlighting the row of rare earth (RE) elements and column-V elements, which form a rocksalt crystal structure (bottom left) typically present in RE-Vs. Inset: Lattice parameters of RE-V compounds spanning common III-V substrates.

Many bulk RE-V crystals possess large nonsaturating magnetoresistance (Figure 1.3C-E), attributed to charge-carrier compensation and the nearly-equal electron and hole high mobilities leading to a parabolic rise in magnetoresistance based on a classical two-band model [55,56]. To date, most thin-film reports of magnetoresistance values in RE-V [57,58] and other XMR semimetals [59] are significantly lower than their bulk crystal counterparts, potentially due to diminished mobilities as a result of surface and defect scattering, as well as possible deviations from exact mobility matching and carrier compensation.

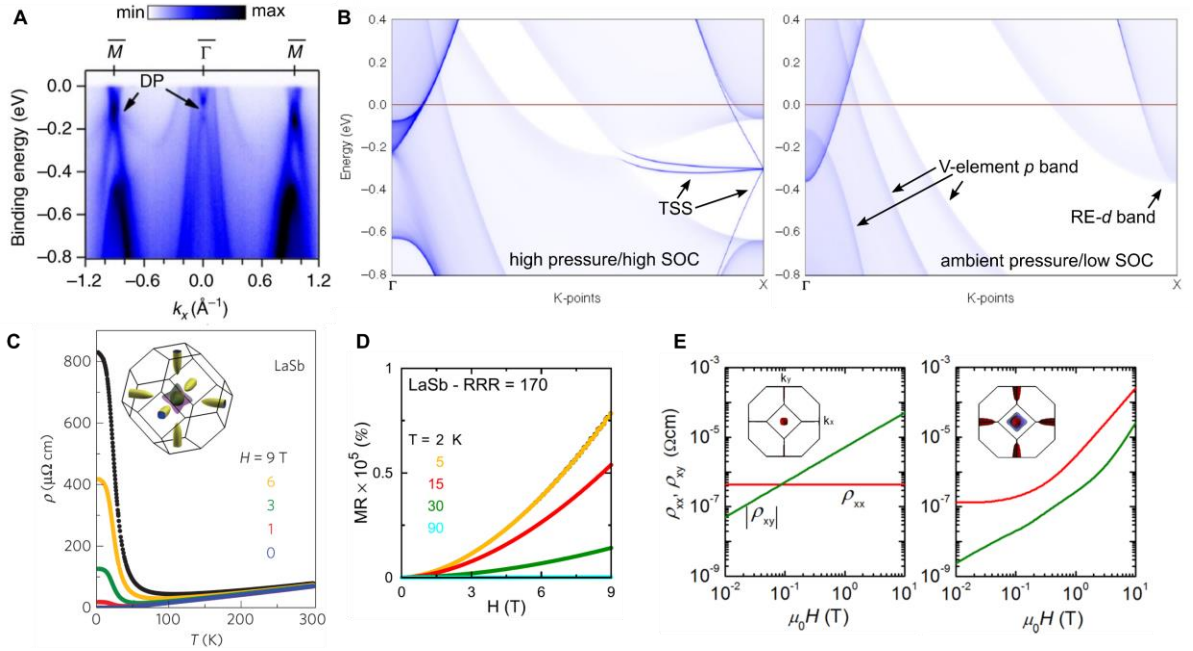

Figure 1.3. (**A**) ARPES spectra of LaBi (001) surface measured along $\bar{M} - \bar{\Gamma} - \bar{M}$ providing evidence of a Dirac point (DP) at $\bar{\Gamma}$ and two Dirac nodes at $\bar{M}$. Adapted from [49]. (**B**) Effect of pressure/group-V element on band inversion in RE-V compounds. Left: RE-V with band inversion at the *X* high symmetry point, and emergence of topological surface states (TSS) connecting the RE-*d* band and V-element *p* band. Band inversion is typically present for RE-V with large SOC/lattice parameters (heavy group-V element, light RE element). Right: RE-V with a trivial band order at the *X* point (no crossing of the valence band *p*-orbital and conduction band *d*-orbital). Adapted from [60]. (**C-D**) Longitudinal resistivity as a function of (**C**) temperature and (**D**) magnetic field in LaSb, showing the onset of XMR at low temperatures and high magnetic fields. In (**C**) the inset shows the Fermi surface of LaSb, a typical RE-V Fermi surface with two hole pockets centered at the Brillouin zone center Γ point and 6 electron pockets at the Brillouin zone edge *X* point. Adapted from [61]. (**E**) Calculated Hall (ρ_{xy}) and longitudinal (ρ_{xx}) resistivity in YSb using a multicarrier anisotropic model. Left: finite ρ_{xx} for a single band modeled, right: non-saturated ρ_{xx} and kinks in ρ_{xy} when accounting for the multiple hole and electron pockets. Adapted from [56].

1.3 Bismuth

Scientists have studied strain and quantum size effects in bismuth (Bi) (111) films for decades, which provide a rich platform for tuning topological order [62], semimetal to semiconducting transitions [63], and quantum-well states [64] (see Figure 1.4). The low carrier density, long mean free path, large spin-orbit coupling, and presence of spin-polarized surface states [65] have made Bi films a promising system for future applications in spintronics [66]. Group-V elemental two-dimensional (2D) layers have also attracted interest in classical electronic and optoelectronic device applications due to their high carrier mobilities and

potential bandgap tunability [67]. The large mass anisotropy in the surface state and the bulk band valleys in the band structure of Bi (Figure 1.4C) allow valley degeneracy to be controlled by the orientation of an applied magnetic field, a feature that can be used in valleytronic devices which encode information through valley-polarized currents [68].

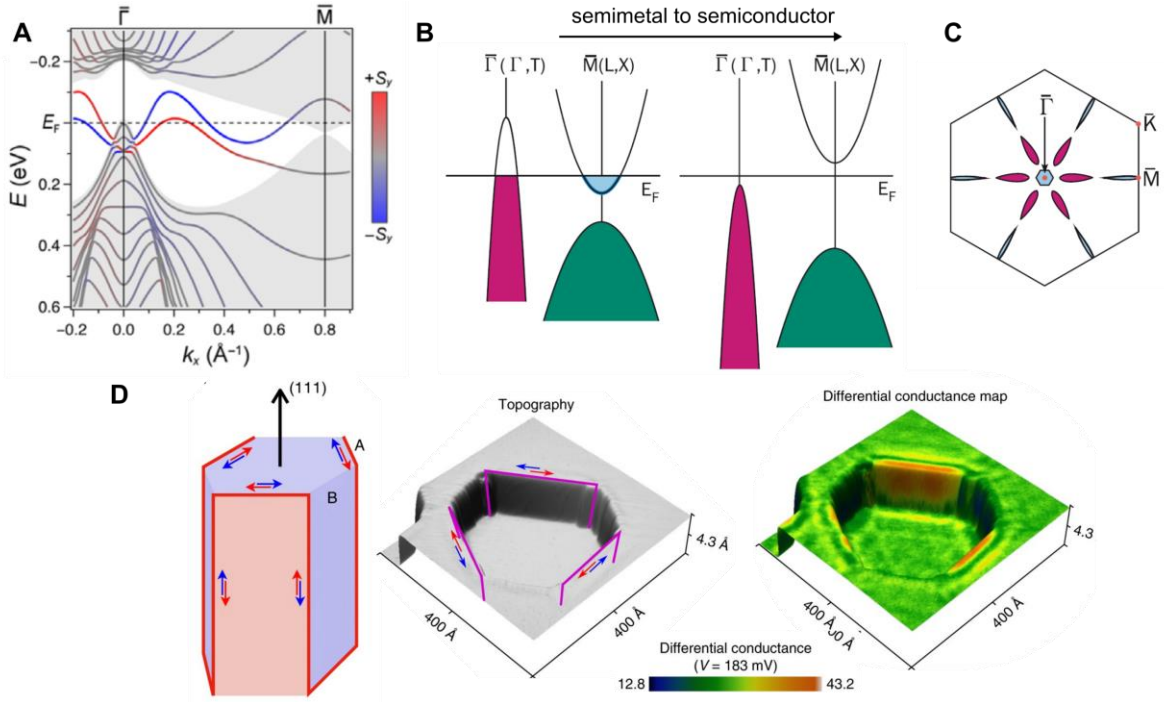

Figure 1.4. (**A**) Band structures obtained by a tight-binding calculation for a 14 bilayer Bi(111) slab. The color scale shows the in-plane spin polarization of each state at the top surface in the direction perpendicular to $\bar{\Gamma} - \bar{M}$. Adapted from [69]. (**B**) Schematic drawing of the Bi bulk band projection near the Fermi level E_F before (left) and after (right) the predicted semimetal to semiconductor transition. (**C**) Schematic drawing of the Fermi surface of ultrathin B(111) films in the surface Brillouin zone. (**B** and **C**) Adapted from [70]. (**D**) Schematic of the 1D hinge states of a hexagonally shaped HOTI oriented along the trigonal [111] axis, and experimental observation of the alternating edge states on a bismuth (111) surface perpendicular to its trigonal axis. (**D**) Adapted from [71].

In the field of topological materials, there is an ongoing effort to classify the $\mathbb{Z}_2$ invariant of Bi experimentally [32,72], which also proves challenging to calculate computationally [73]. A single Bi (111) bilayer (BL) with a nontrivial $\mathbb{Z}_2$ topological number is predicted to behave as a quantum spin Hall insulator [74]. Along the Bi (111) step edges, one-dimensional (1D) helical modes were also observed [71,75], an ingredient in one proposed platform to construct Majorana zero modes [76].

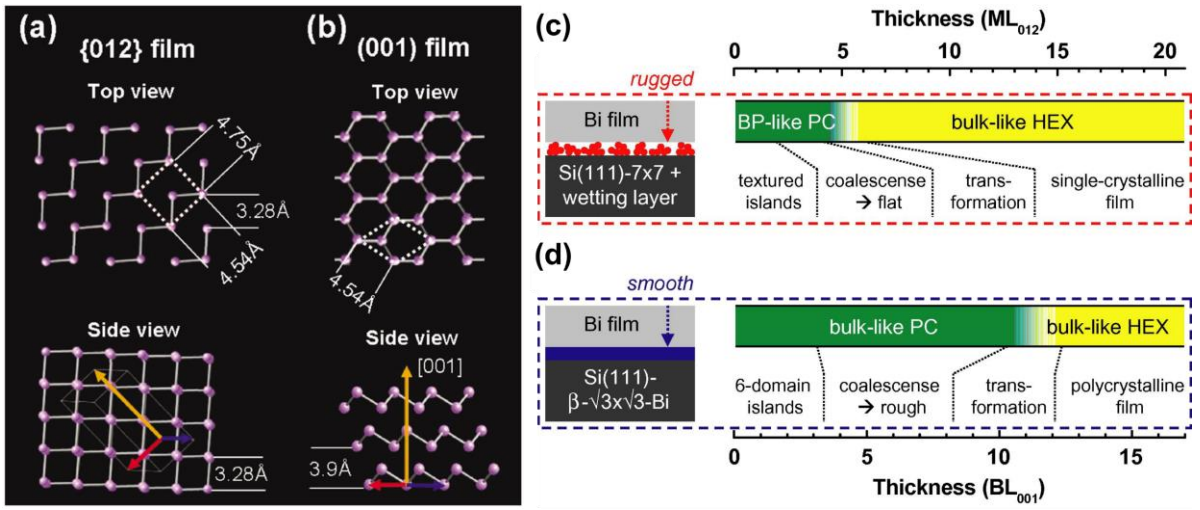

Figure 1.5. (**a**-**b**) Top and side view schematics of different bismuth allotropes, the orange arrow pointing at the trigonal c axis ($<001>_h$) red and blue at $<100>_h$ axes. (**a**) The pseudocubic (PC){012} phase (semi-infinite $(110)_r$ in the rhombohedral A7 structure of bulk Bi). The {012} PC structure is similar to the orthorhombic A17 structure of bulk black phosphorus (BP). Adapted from [77]. (**b**) The hexagonal (HEX) $(0001)_h$ structure, $(111)_r$ in the rhombohedral notation. (**c** and **d**) Bi thin film growth on two different surface reconstructions of Si (111) and the minimum nominal thickness required to transition to a coalesced hexagonal film. Adapted from [78].

The synthesis of large-area single-domain ultrathin (<6 BL) buckled Bi (111) on conventional semiconducting substrates has remained a challenge, with only planar bismuthene wetting layers on SiC [79] and GaAs [80] reported thus far. On weakly interacting substrates, such as highly oriented pyrolytic graphite, Bi nucleates typically in the black phosphorus (BP)-like phase [81,82], and transforms later to the rhombohedral $(111)_r$ oriented phase, see Figure 1.5. The topological properties of the BP-like phase of Bi depend on the degree of buckling in the structure, where a single flat layer of BP-like Bi was proposed to be a quantum spin Hall insulator, and even-layer BP-like films with a flat surface are topological insulators [83].

For Si or Ge (111) substrates, weak film-substrate van der Waals (vdW) interactions [84,85] also lead to the nucleation of a nearly freestanding Bi layer, starting at the BP phase and transforming to a $(111)_r$ orientation only after a 6-8 BL thick film coalesces [77]. Ultrathin Bi (111) films were nucleated on the topological insulator substrate Bi_2Te_3 [86–89], where in-plane contraction [90,91] is suggested to stabilize a topologically insulating phase.

However, compressive strain and band hybridization with the Bi_2Te_3 substrate, along with low correspondence between the experimental data and the calculations at the ultrathin limit [87], make it difficult to study the topological classification of unstrained Bi and the semimetal to semiconducting transition predicted for ultrathin Bi films [92].

Bulk Bi is a low-carrier density semimetal with a valence-band maximum at the time-reversal invariant momentum (TRIM) T point (projecting to $\bar{\Gamma}$ for the (111) surface) and a conduction-band minimum at the L TRIM point (projecting to $\bar{M}$), see Figure 1.6A. The small direct bandgap at the L point is only of a few meV and determines whether Bi is a topological insulator (an inverted bandgap at L) or a higher-order topological insulator (no band inversion at L).

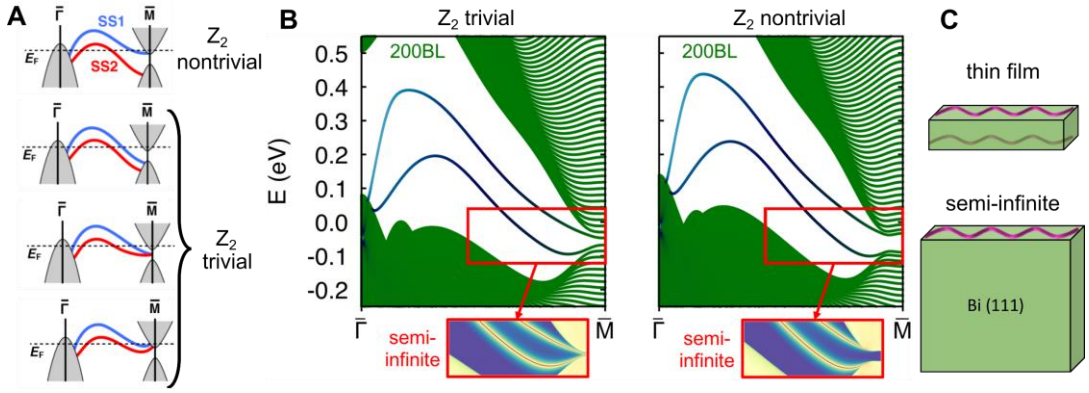

Figure 1.6. (**A**) Possible surface state connectivity to the bulk band structure along the $\bar{\Gamma} - \bar{M}$ direction for the two spin-split surface state (SS) dispersions. Adapted from [72]. (**B**) Calculated band structure of a finite film and semi-infinite Bi crystal for the $\mathbb{Z}_2$ trivial and nontrivial case. Adapted from [73]. (**C**) Hybridization between neighboring surface states in a thin film vs a single surface measured from a semi-infinite crystal.

Bi is predicted to lie at the border of a topological phase transition between a higher-order topological insulator and a topological insulator phase [32]. Calculations have shown that the indirect T-L gap ($\bar{\Gamma} - \bar{M}$ for the (111) surface) and the direct inversion bandgap at L depend on electron doping [93], biaxial and shear strain [32,62,87], and bulk alloying in $Bi_{1-x}Sb_x$ [4]. Yet despite the challenge of estimating the gap size at the L point, most DFT calculations [62,73] predict a trivial band order at the L point for unstrained bulk Bi crystals.

More accurate quasiparticle self-consistent *GW* (*QSGW*) calculations also yield nontrivial behavior, with a gap at L of 13 meV compared to 86 meV in standard DFT [62].

ARPES measurements [69,72,94] of Bi thin films have nonetheless shown surface states gapped at the $\bar{M}$ point, which in the past were attributed to a $\mathbb{Z}_2$ nontrivial band topology (Figure 1.6A). Since the surface states near the Brillouin-zone edge penetrate deep into the film bulk, on the order of 100s of bilayers [73,95,96], crosstalk between surface states on neighboring surfaces could lead to the formation of a hybridization gap and the appearance of a topological-like signature even in the trivial semimetal case (Figure 1.6B-C). ARPES spectra of films as thick as 200 BL grown on Ge (111) still show gapped surface states lying close to each other [72], obscuring the direct determination of a surface state gap/degeneracy even for relatively thick films.

1.4 Topological half-Heusler compounds

Heusler compounds have emerged as an exciting material system where the realization of functional and tunable novel topological phases might be possible [97–99]. Interest in Heuslers stems from the broad structural basis, with thousands of members holding identical crystal symmetries and tunable electronic properties [100,101]. Half-Heuslers are intermetallics with a C_{1b} structure that may be thought of as being composed of three interpenetrating face-centered cubic lattices. The Slater-Pauling rule provides a simple model to predict their saturation magnetization (*M*) and carrier density based on the valence electrons per formula unit (N_V): $M \propto N_V - 18$ where a closed shell configuration of 18 valence electrons in half-Heuslers is found in semiconductors or low carrier semimetals such as LuPtBi, whereas a

deviation from the 18 valence electron number produces a ferromagnet with a higher carrier density and a net magnetic moment proportional to the valence count.

Several 18 valence half-Heusler compounds with elements having high nuclear charge behave as topologically nontrivial compounds [97–99], and among them, LuPtBi has the highest predicted band inversion (Figure 1.7A). Though ARPES studies conducted on LuPtBi have shown evidence supporting the compound's topological nature [99,102], there are still open questions regarding the dispersion and position of topological and trivial surface states for various possible surface orientations and terminations of topological half-Heuslers [102]. Early calculations of band inversion in Heusler compounds [97–99] have suggested biaxial strain as a method to open a bandgap in semimetals (see Figure 1.7B). To date, no experimental study shows trends in bandgap opening for strained Heusler films.

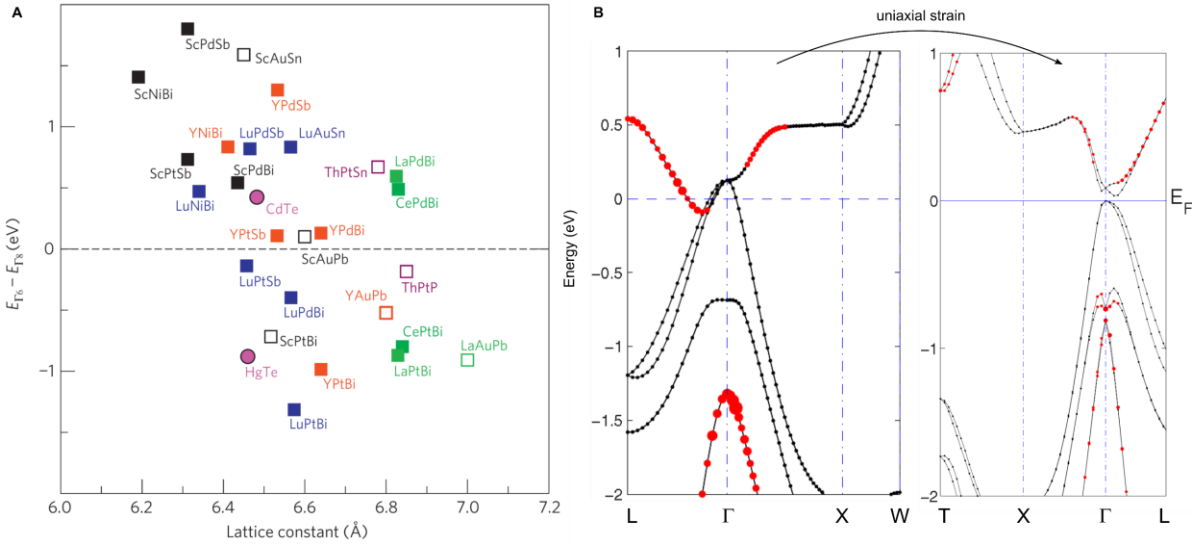

Figure 1.7. (**A**) Topological band inversion strength in half-Heusler compounds plotted as a function of the lattice constant. Negative values denote the presence of inversion. Adapted from [97]. (**B**) Band structure of LuPtBi unstrained (left) and under uniaxial strain along the [111] direction (right) opening a gap. Red markers indicate the contribution of *s*-like orbitals, and their size represents their strength. Adapted from [98].

Previous experimental studies of predicted topological half Heuslers such as LuPdBi [103], LuPtSb [104], YPtSb, and LaPtBi [105] showed zero-gap semiconductor behavior. Moreover, in other compounds such as LuPtBi and YPtBi [102], the Dirac point of the TSS appears

several eV below the Fermi level. Early studies of REPtBi (RE=Dy, Gd, Lu) [106] compounds showed only a topological trivial behavior, possibly due to TSS appearing only deep in the valence band. Ideally, one would want a topological insulator without trivial surface states or bulk conduction paths crossing the Fermi level so that transport would be TSS dominated. Possible approaches to obtaining the goal of a bandgap would be the application of epitaxial strain or possibly inducing uniaxial strain and symmetry breaking by exploiting other possible tetragonal or hexagonal phases that can also be formed through alloying [107] or magnetization [108]. Bulk doping schemes of epitaxial Heusler films [109] were also shown to assist in shifting the chemical potential to match the Dirac point of the TSS.

One challenge the single-crystal and thin-film Heusler community has faced for many years is the appearance of point defects leading to lower symmetry disordered states [110]. The most prominent types of disordered states occurring in the half-Heusler structure are CaF_2 and NaTl [100]. Other typical defects that can appear in Heuslers include anti-site defects (mostly swapping sites in the rocksalt substructure) [111] and interstitial atoms in off-stoichiometry compounds such as $Ni_{1+x}ZrSn$ [112]. Charged defects can lead to unintentional shifting of the chemical potential, whereas neutral defects can also produce unwanted filled bands which lower the observed bandgap.

1.5 Thesis overview

This dissertation explores the epitaxial growth, surface, and electronic properties of three novel materials systems, all of which have a semimetallic band structure and are either topological or closely related to topological materials in their structural class. Our work seeks to explore routes to increase the functionality of these semimetals through epitaxial integration

with a III-V semiconducting platform and advance our basic understanding of the electronic properties of these materials in thin film form through quantum size effects, heteroepitaxy, and strain engineering. Chapter 2 provides an overview of the experimental methods used in the presented research. The scientific principles behind materials growth via molecular beam epitaxy, and surface science and electronic structure characterization are discussed. Chapter 3 will explore the growth and electronic structure characterization of GdSb thin films. The chapter focuses on comparing multiple experimental and computational approaches to studying the electronic structure of RE-V thin films. Chapter 4 follows the evolution of the band topology in strained GdSb thin films. In chapter 5, we discuss the growth, surface structure and electronic structure of ultrathin Bi (111) films and their topological assignment. Chapter 6 outlines the growth window of LuPtBi thin films and their electronic properties. Conclusions and suggested future work will be addressed in Chapter 7.

2 Methods: materials growth and characterization

The epitaxial films studied in this dissertation were grown via molecular beam epitaxy (MBE) in the ultrahigh vacuum (UHV, base pressure <1 10^{-9} Torr [113]) interconnected setup of MBEs and characterization tools in the Palmstrøm Laboratory at the University of California, Santa Barbara (see Figure 2.1). The facility includes 7 MBE chambers, 4 surface preparation, metal and dielectric deposition transfer chambers, angle-resolved and X-ray photoemission spectroscopy (ARPES, XPS) chambers, 3 scanning tunneling microscopy chambers, a magneto-optic Kerr effect (MOKE) magnetometer, one experimental chamber for effusion cell deposition and multiple vacuum suitcases used for transporting films under vacuum.

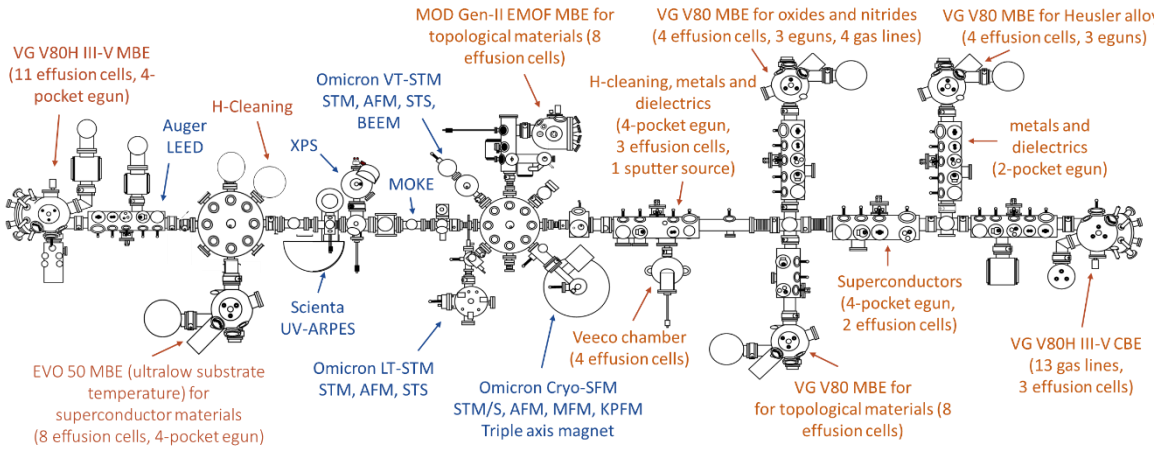

Figure 2.1. UHV interconnected deposition and analysis facility in the Palmstrøm lab at the University of California, Santa Barbara, as of April 2023. Growth chambers are listed in brown, and characterization capabilities are listed in blue.

2.1 Molecular beam epitaxy

MBE is a physical vapor deposition technique performed at UHV that provides high-quality epitaxial structures and films. The term epitaxy means that the deposited layer has a crystallographic order and registry dictated by the underlying crystal plane of the substrate

used for growth. MBE as a technique for the growth of single crystal films was originally developed for semiconductor research in the 1960-70s [114]. Since then, it has been used for a wide variety of materials, including semiconductors such as Si/Ge, III-V, II-VI, and IV-VI compounds and, more recently, oxides, transition metal compounds, two-dimensional materials, and quantum materials. A key advantage of MBE is the ability to achieve atomic-level control over composition; structural ordering; quantum confinement in 0/1/2D structures; metastable phase formation; impurity concentrations; and strain. Finally, being a UHV technique, MBE offers not only synthesis benefits but also *in situ* film characterization and monitoring. This makes MBE a powerful tool for fabricating electronics and optoelectronics and exploring novel phases of matter.

In MBE chambers, molecular beams are typically composed of atoms or clusters of atoms that are thermally evaporated from effusion cells or electron guns, as demonstrated in Figure 2.2. Assuming an ideal gas behavior, the mean free path of the molecular beam, L (defined as the average travel traversed by molecules between successive collisions) equals [113]:

$$L = \frac{\sqrt{2}k_B T}{2\pi P d^2}$$

Were k_B notes the Boltzmann constant, d is the molecular diameter, and P and T are the gas pressure and temperature. The UHV environment enables molecular beams to travel over kilometers with minimal scattering. For example, an Aluminum atom with a diameter of 2.86 Å, evaporated at 1000 ^{o}C and operational chamber of 10^{-8} Pa would have a mean free path of L=4840 km. When the evaporated atoms reach the substrate surface, they can diffuse kinetically and order across the surface without the adsorption of impurities for days.

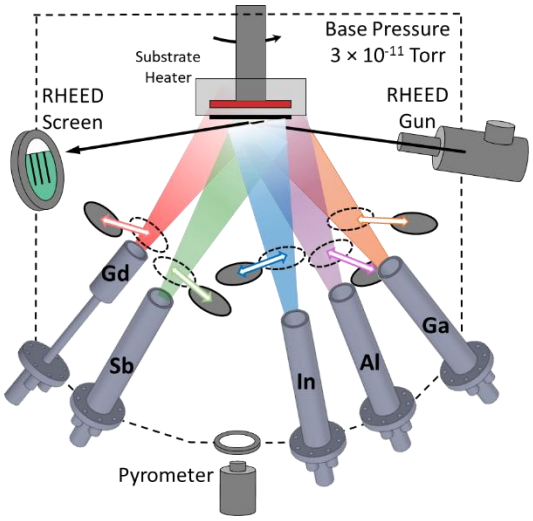

Figure 2.2. Schematic of the essential parts of an MBE chamber in a UHV environment. Shutters control the substrate exposure time to molecular beams evaporated from effusion cells or electron-beam guns. The substrate can be heated with a resistive wire, and the temperature is monitored with a thermocouple in close contact with the substrate and with a pyrometer. The substrate can be rotated for better uniformity and to access various azimuth angles of the surface probed by *in situ* RHEED.

The rate of residual gas species of type i (R_i) striking the surface of the substrate, or the molecular beam flux (J_i) is given by [113]:

$$R_i = J_i = p_i \sqrt{\frac{N_A}{2\pi k_B M_i T}}$$

N_A is the Avogadro constant, M_i is the molecular weight, and p_i is the gas partial pressure or the molecular beam pressure. Based on this equation, one can estimate the time it would require for the molecules hitting the surface to build up a single monolayer of adsorbates. Assuming a sticking coefficient, S, of 1 (that is all atoms that impinge the surface remain on it), and $T = 300\ K, M_i = 28\ amu$ and a substrate surface density of ~10^{-15} molecules/cm^2, then at a pressure of approximately 10^{-6} Torr one monolayer of molecules builds up every second [115]. The dosage unit of Langmuir: $1\ L = 10^{-6}\ Torr \cdot sec$ is therefore commonly used by surface scientists to describe the gas exposure time of a surface.

One of the most common characterization measurements used *in situ* during MBE crystal growth is reflection high-energy electron diffraction (RHEED) [116]. The method consists of

a collimated electron beam at a high energy of E=10-30 keV irradiating the sample surface at a grazing angle, after which it is scattered to display a diffraction pattern on a fluorescent screen (Figure 2.2). RHEED can provide information on the atomic surface reconstruction, epitaxial relation between the film and substrate, the surface topography (Figure 2.3), and the growth rate (Figure 2.4).

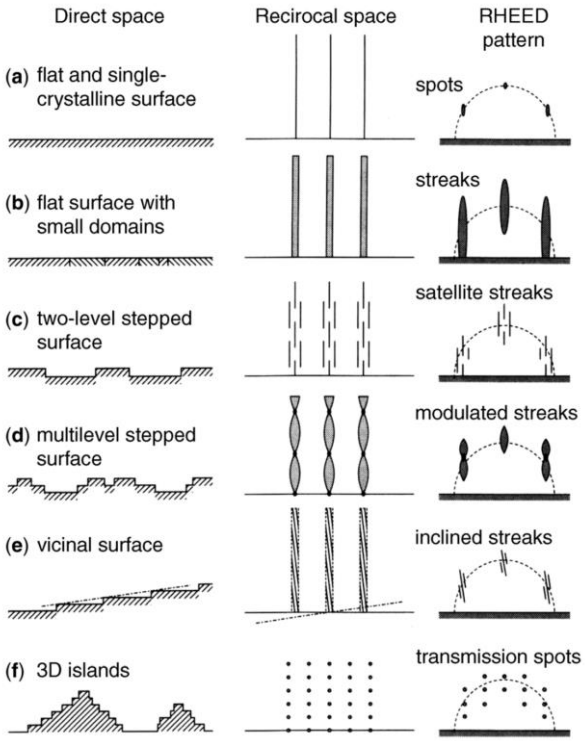

Figure 2.3. Schematics of various surface topographies in real space, their reciprocal space ordering, and the resulting RHEED pattern at the Ewald sphere intersection. Figure reprinted with permission from [117].

The diffraction pattern obtained in RHEED can be thought of as the intersection between the Ewald sphere and the surface reciprocal space lattice. The radius of the Ewald sphere is defined by an electron wave-vector, k_0[3]:

$$|k_0| = \frac{1}{\hbar}\sqrt{2m_eE + \frac{E^2}{c^2}}$$

m_e being the electron rest mass in vacuum and c the speed of light. The Ewald sphere of keV electrons is orders of magnitude larger than the most in-plane distances between reciprocal

lattice rods generated in a perfect 2D surface, yielding a nearly planar cut through the first few Brillouin zones of the reciprocal lattice. Therefore, a perfectly flat and ordered surface should have spots lying on circular arrays (see Figure 2.3(a)). Any surface non ideality will be reflected in the reciprocal space construction, and consequently the RHEED pattern. For example, short-range lateral ordering of the surface (i.e. small domain size) will lead to broadening of the reciprocal lattice rods, resulting in wider and longer streaks, (see Figure 2.3(b)). For a rough three-dimensional surface (Figure 2.3(f)) transmission of the electron beam through the islands will lead to the appearance of three-dimensional spots.

2.1.1 The MBE growth window

The MBE growth window refers to the pressure and temperature conditions at which a certain surface reconstruction, or a compound of a given phase/stoichiometry, can be stabilized (whether kinetically or thermodynamically). The pressure conditions typically include absolute growth rates and their ratios (in multi-element systems), and the substrate temperature is controlled typically through active infrared radiation heating with a resistive wire heater or conductive cooling through a conductive heating with a cold finger. Additional approaches to altering the growth window include modulated beam techniques through control over the shutter sequence [118], photoassisted deposition [119], and the use of surfactants [44], which influence surface energies, atom reactivity, and surface mobility.

The growth rate of epitaxial films in MBE chambers is of the order of sub-Angstroms per second to several microns per hour. Growth rates are often controlled by adjusting the effusion cell temperature, which impacts the partial pressure of the molecular beam reaching the

sample. The growth rate in an MBE chamber can be monitored using several common *in situ* tools, such as –

RHEED oscillations: during layer-by-layer growth, the intensity of the RHEED diffraction pattern oscillates over the period corresponding to the growth of one layer. As the film coverage evolves from a flat plane (layer *n*) with complete coverage, θ=0, to a fractional new plane (layer *n+1, 0*<θ<1) back to full atomic coverage (layer *n+1,* θ=0), the RHEED pattern oscillates due to constructive/destructive interference from the same plane/multiple levels in a partially covered film, respectively. In Figure 2.4 an example of RHEED oscillations is provided for a heteroepitaxial nucleation of a lattice mismatched film. Multiple oscillation periods are observed with decreasing amplitude as the growth proceeds due to the gradual roughening of the sample surface (due to film relaxation and decreased adatom mobility).

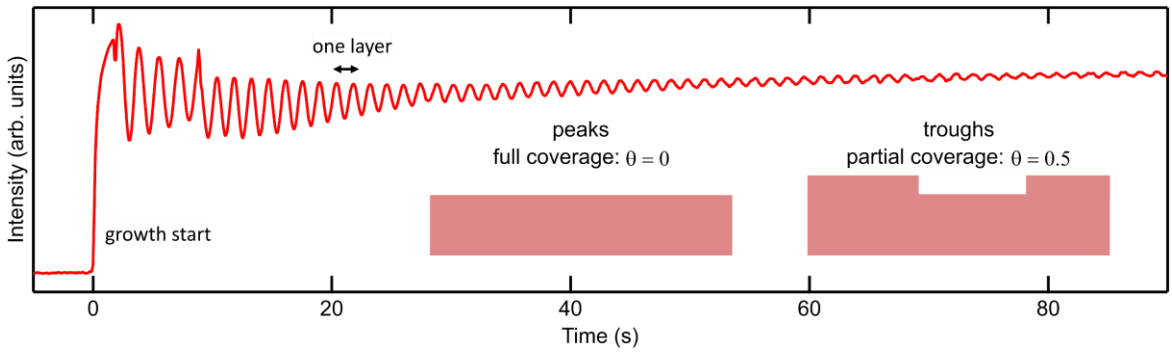

Figure 2.4. RHEED oscillations measured during MBE growth of $In_{0.244}Al_{0.756}Sb$ nucleated at 340 °C on GaSb (001) at a growth rate of 0.7 bilayers /sec (2 bilayers per unit cell). The intensity of the specular RHEED spot is measured as a function of deposition time, where the oscillation period corresponds to the completion of a single bilayer.

Beam flux monitor: A beam flux monitor is a hot cathode ion gauge introduced near the substrate in a position that intercepts the molecular beam. As atomic clusters/atoms are ionized, the current in the ion gauge relates to the relative pressure produced, but it cannot distinguish between the different atomic species that are produced. A beam flux monitor can be used to calibrate most molecular beams as long as their adsorption does not change the cathode work

function, an effect called ion gauge poisoning [120]. Furthermore, beam flux monitor readings are position sensitive and are affected by chamber design. Therefore, it is not an absolute gauge and is typically calibrated with other *ex situ* techniques.

Quartz crystal microbalance (QCM): The mechanical resonance frequency of a quartz crystal depends on the mass of material deposited on the surface. A QCM is a device that measures the resonance frequency change as a function of deposition to determine the deposition rate. Similar to the beam flux monitor, the QCM is inserted near the substrate to obtain accurate readings of the beam flux. Because the QCM frequency is sensitive to mechanical vibrations and temperature, active cooling and stable temperatures are required. QCMs are particularly useful when measuring growth rates of elements evaporated with an electron gun since the stray magnetic field generated by the electron beam deflectors affect both ion gauge readings and electron beam paths in nearby RHEED electron guns. Similar to the beam flux monitor, the QCM does not provide an absolute reading. Additional *ex situ* calibration methods are needed to account for the geometry and position sensitivity of the QCM through a tooling factor correction.

It is also common to perform *ex situ* thickness calibrations of MBE-grown films. Characterization approaches include Rutherford backscattering spectrometry (RBS), X-ray diffraction and reflectivity, ellipsometry, transmission electron microscopy, profilometry, and more.

In addition to determining the molecular beam flux, the substrate temperature in an MBE chamber is another parameter that can be tuned to control the growth kinetics such as bulk/surface diffusion, and could even influence the growth rate through partial evaporation of the impinging atoms. The fraction of incoming species remaining adsorbed on the substrate

is referred to as the sticking coefficient. For the materials studied in this dissertation, the sticking coefficient can be considered as equal to unity for most metal sources (Gd, Lu, Pt, Al, In, Ga) and less than one for group-V sources (Sb, Bi) depending on the surface temperature.

By adjusting the substrate temperature, and source material flux, the growth regime can be changed from a statistical growth regime (where there is minimal surface diffusion of impinging atoms) to a diffusional step-flow growth mode (maximum diffusion length of surface adatoms) [121]. Substrate temperatures are typically monitored with a thermocouple adjacent to the substrate, but depending on where the thermocouple is place, real temperature offsets could be as high as 100-150 ^{O}C degrees, or more. Therefore, additional *in situ* thermometry tools are used in MBE growth, among them thermal reconstructions/phase changes monitored with RHEED/pressure gauges, band-edge measurements in semiconductors, and pyrometry in metals and narrow-gap semiconductors. Band-edge thermometry in semiconductors relies on the temperature dependence of the bandgap and pyrometers are based on changes in black-body radiation of a sample with a known surface emissivity.

Oxide thermal desorption temperatures on chemically prepared surfaces of III-V semiconductors (epi-ready) are commonly used to calibrate thermometry tools in III-V MBEs. The transition can be monitored both with RHEED and flux-gauge readings. Besides known desorption temperatures of layers, surface reconstructions occurring at known pressure and temperature windows can also be used to monitor substrate temperature. Finally, phase transition temperatures such as melting/sublimation points can also be employed for sample/heater calibrations. In all cases, systematic temperature ramp rates need to be employed due to the kinetic nature of many of these phase changes/chemical reactions. The temperature

ranges provided in this work were calibrated using multiple approaches, mainly relying on oxide thermal desorption, surface reconstruction changes, and pyrometry. Reliable calibrations of the real sample temperature were important for the semimetals grown in this work due to the limited temperature range of their growth window.

2.1.2 Strain in epitaxial films

MBE offers the ability to create pristine interfaces and surfaces, which are crucial for epitaxial strained/relaxed heterostructures. Thin films can develop built-in strain through heteroepitaxial (dissimilar material) growth of lattice-mismatched materials or in lattice-matched systems due to thermal expansion mismatch. Strain and relaxation in epitaxial films are generally grouped into three categories: (i) homomorphic, the film and substrate are the same material; (ii) pseudomorphic, the film layer is fully strained to the substrate; and (iii) metamorphic, the film and substrate are lattice mismatched and the film is relaxed. The two latter cases present interesting novel functionality in electronic structure engineering and the design of band offsets in heteroepitaxial superlattices [122].

In pseudomorphic growth, the epitaxial film is coherently strained in-plane to the underlying substrate and is thermodynamically stable as long as it remains below the critical relaxation thickness (Figure 2.5A, left). Film relaxation, i.e., plastic deformation of the film relieving the elastic energy, takes place when the elastic strain stored due to lattice mismatch (E_s) surpasses the energy required to form a misfit dislocation [123] or bend an existing threading dislocation [124] ($E_{dislocation}$) or form any other stress-relieving defects such as cracks or hillocks [125,126]. The elastic energy associated with epitaxial films that are coherent with their substrates scales linearly with the film thickness, h [121]:

$$E_s = 2\mu\left(\frac{1+\nu}{1-\nu}\right)h\epsilon_{||}$$

ν is the Poisson's ratio and μ is the shear modulus. The energy required to form a dislocation of a mixed screw and edge character $E_{dislocation}$ equals [9]:

$$E_{disslocation} = \frac{\mu b^2}{4\pi}\left(\frac{1-\nu\cos^2\beta}{1-\nu}\right)\ln(4h/b)$$

b is the burgers vector of the dislocation, and β is the angle between the burgers vector and the dislocation line ($\cos\beta = 1$ for a screw component and 0 for an edge component). Both energies scale with film thickness and the crossing point between the two is defined as the critical thickness (h_c).

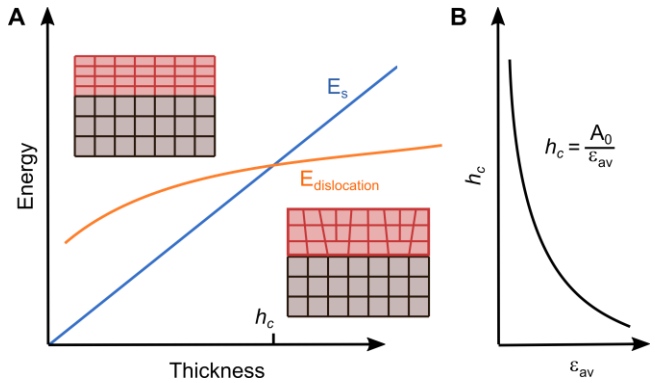

Figure 2.5. (**A**) The elastic strain energy E_S in a lattice mismatched film increases linearly with film thickness, and the misfit dislocation energy $E_{dislocation}$ increases logarithmically with film thickness. A crossover between the two energies takes place at the critical thickness, h_c. Before reaching h_c (left), the epitaxial film is a pseudomorphic layer. After crossing h_c (right), the film is partially relaxed or remains a metastable pseudomorphic layer. (**B**) A plot of the empirical law of h_c vs average film strain ε_{av}, A_0 is a constant accounting for geometric factors, forces on dislocations, and material elastic constants.

Beyond h_c (Figure 2.5A, right) the metamorphic layer has dislocations relieving the strain energy and the film is either partially or fully relaxed. According to Matthews and Blakeslee [124] the onset of relaxation takes place through the penetration of a threading dislocation from the substrate and bending at the epitaxial layer:

$$h_c = \frac{b}{8\pi\epsilon_0\cos\lambda}\left(\frac{1-\nu\cos^2\beta}{1+\nu}\right)\ln(4h_c/b)$$

ϵ_0 being the maximum misfit strain and $\cos\lambda$ is the angle between the glide plane of the dislocation and the interface. Empirically, h_c is found to scale inversely with the average strain (Figure 2.5B) [126], though most of the empirical studies and analytical models are limited to strain levels below 1-1.5% in Si/Ge and IIII-V compounds [125].

Metamorphic buffer layers are useful as virtual substrates for the subsequent growth of lattice-matched epitaxial thin films. For example, ternary and quaternary III-V compounds are not readily available as substrates but are routinely grown as metamorphic buffer layers. Various schemes have been proposed in order to reduce the threading dislocation density or the roughness of metamorphic buffer layers, such as tuning the growth temperature, deposition rate, and the introduction of abrupt interfaces or patterned substrates [122,126]. For example, the III-V metamorphic buffer layers studied in this dissertation were nucleated at low temperatures and high nucleation rates in order to avoid island growth.

2.2 Angle-resolved photoemission spectroscopy

Angle-resolved photoemission spectroscopy (ARPES) is a powerful technique used to probe the electronic band structure, Fermi surface, and many-body effects in materials. Through ARPES one can gain information on the lifetime of electronic states, from which the strength of interactions between electrons in the material is inferred. Early materials studied with ARPES included simple metals and cooperate superconductors, and more recently due to significant technical developments in photoelectron spectrometers and synchrotron light sources, ARPES measurements have become widespread and are now applied to a wide range of novel materials including low dimensional materials, topological materials, and new superconductors [11,127].

ARPES involves shining light (with a photon energy $h\nu$) onto a sample in UHV and measuring the kinetic energy (E_{kin}) and angle of emitted photoelectrons (θ) with a hemispherical analyzer (see Figure 2.6a and b) [128,129]. Due to energy conservation and in-plane momentum conservation (where translational symmetry is preserved), the measured photoelectron obeys the following relations (assuming the azimuth angle is set to $\varphi = 0$):

$$E_{kin} = h\nu - WF - E_B$$

$$k_{||} = \frac{1}{\hbar}\sqrt{2m_e E_{kin}}\sin\theta$$

WF is the work function of the material; E_B is the binding energy of the electron inside the sample; $k_{||}$ is the parallel component (with respect to the sample surface) of the momenta of the photoelectron both in vacuum and in the sample; $\hbar$ is the reduced Planck's constant; m_e is the electron rest mass; and θ is the emission angle with respect to the plane normal. By rotating the azimuth angle, φ, E-$k_{||}$ cuts along different high-symmetry directions can be plotted, as shown in Figure 2.6c.

In the out-of-plane momentum, there is no momentum conservation for the electron moving from the crystal to vacuum $k_\perp^{solid} \neq k_\perp^{vac}$, due to the abrupt potential change across the interface breaking translational symmetry. Therefore, to determine $k_\perp^{solid}$ the final state of the photoelectron in the solid is assumed to behave as a nearly free electron dispersion with an energy minimum of V_0 (called the inner potential) which accounts for the discontinuity in $k_\perp$ at the surface:

$$k_\perp^{solid} = \frac{1}{\hbar}\sqrt{(\hbar k_\perp^{vac})^2 + 2m_e V_0} = \frac{1}{\hbar}\sqrt{2m_e(E_{kin}\cos^2\theta + V_0)}$$

One approach to finding the inner potential is through $h\nu$-dependent measurements, where the periodicity of the out-of-plane band dispersion $E(k_\perp^{solid}) = E(k_\perp^{solid} + nG_\perp)$ is mapped

(for 3D-like bands) when crossing between Brillouin zones *n* integer times by a reciprocal lattice vector $G_{\perp}$. This approach also allows distinguishing 2D surface states from 3D bulk bands as surface states are not expected to disperse in $k_{\perp}$.

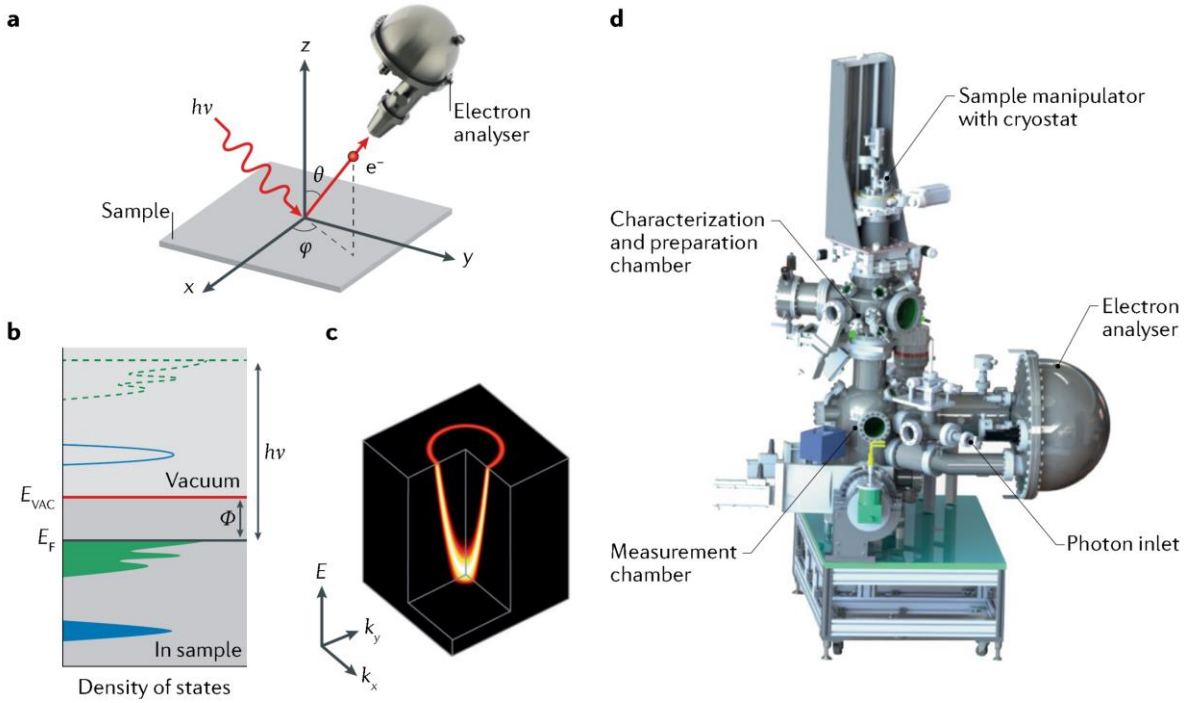

Figure 2.6. (**a**) The basic principle of ARPES measurements. Electrons in the solid absorb photons and escape into the vacuum as photoelectrons, which are collected by an electron analyzer. The emission angles θ and φ of the photoelectron are indicated; *hν* is the photon energy. (**b**) Energetics of the photoemission process (Φ is the material's work function, E_F is the Fermi level, and E_{VAC} is the vacuum level). (**c**) Simulated ARPES data showing the band structure of a 2D free-electron system, where k_x and k_y are the momenta in the *x* and *y* directions. (**d**) An illustration of an ARPES spectrometer and UHV chambers. Figure reprinted with permission from [11].

Photoemission measurements can be performed with light source energies ranging from a few eV to 1000 eV, where the photon energies determine the electron inelastic mean free path (IMFP, λ_{IMFP}) [130] and the range and resolution of both $k_{\perp}$ and $k_{||}$. The key advantage of operating at low photon energies in the vacuum ultraviolet (VUV) range is the higher $k_{||}$ resolution for a given detector angular resolution. On the other hand, both λ_{IMFP} and $k_{\perp}$ are both worse for VUV light. The electron IMFP follows a universal curve that has a minimum near 20–100 eV, where the electron escape depth is only of the order of a few monolayers.

This high surface sensitivity imposes stringent requirements for clean and flat surfaces. Moreover, due to the position-momentum uncertainty principle, if the electron origin in the film plane-normal direction is known with high confidence then by definition $k_\perp$ should experience high broadening: $\Delta k_\perp \approx \hbar/\lambda_{IMFP}$.

2.2.1 Photoemission studies of quantum wells

Quantum well photoemission studies have mostly been conducted on metallic thin films grown via MBE [131,132] and bulk crystals with extensive surface band-bending, resulting in quantum confinement of the bulk wave function [133]. ARPES can be used to determine quasiparticle lifetimes, band structures, substrate-film interactions, and phase shifts in quantum wells. However, atomically uniform films are necessary in order to avoid broad quantum-well state peaks caused by high film roughness [131].

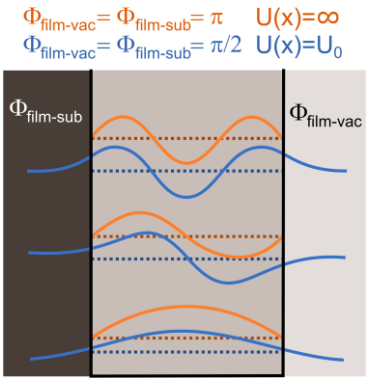

Figure 2.7. Schematic representation of wavefunctions for the first three states in a 1D quantum well box with a potential U(x) outside the well. Two cases are shown: an infinite potential barrier (orange), and a finite barrier, U_0 (blue), and examples of the corresponding phase shifts at the film-vacuum ($\Phi_{film-vac}$) and film substrate ($\Phi_{film-sub}$) boundaries are provided.

One spectroscopic approach to studying the degree of confinement of quantum well states at a given $k_{||}$ in a thin film is the phase accumulation model [131,132,134]. The model is derived directly from the Bohr-Sommerfeld quantization condition for the existence of a quantum well state of a quantum number *n*:

$$2k_z d + \Phi_{tot} = 2\pi(n-1)$$

where k_z is the wavevector perpendicular to the film plane, d is the film thickness, and the total phase shift, Φ_{tot}, is the sum of the phase shifts at each interface: $\Phi_{tot} = \Phi_{film-vac} + \Phi_{film-sub}$. In the ideal case of a quantum well with infinite potential boundaries (see Figure 2.7), we arrive at a standing wave solution: $\Phi_{tot} = 2\pi n$, where each interface has a reflection of π. If the phase shift of a given interface is small and approaches 0, there is significant spilling of the electron density into the underlying substrate.

The film-vacuum phase shift can be calculated using the Wentzel, Kramers, and Brillouin (WKB) approximation for a pure image potential [132]:

$$\Phi_{film-vac} = \pi\left(\sqrt{\frac{3.4}{WF - E}} - 1\right)$$

where WF is the work function of the film surface. The quantum well states are assumed to follow a certain $E(k_z)$ dispersion that can be extracted either computationally or empirically. Assuming Φ_{tot} is only a function of the binding energy for the quantum numbers *n*, and n', and by solving equation the Bohr-Sommerfeld quantization condition for two different quantum well states (n', n) with the same binding energy (E) but different film thicknesses (d', d) [131]:

$$k_z(d', \mathrm{n}') = k_z(d, \mathrm{n}) \rightarrow k_z = \frac{\pi}{2}\frac{n - n'}{d' - d}$$

the out-of-plane dispersion $E(k_z)$ is mapped, and from that relation the total phase shift can be found. For example, if there is a linear dispersion $E = \alpha k_z + \beta$ the total phase shift, Φ_{tot}, for a given quantum state n can be extracted from the slope in the binding energy vs. inverse thickness [72]:

$$E = \alpha \left[\frac{2\pi(n-1) - \Phi_{tot}}{2d}\right] + \beta = \frac{\alpha}{2d}\left[2\pi(n-1) - \Phi_{tot}\right] + \beta$$

Once Φ_{tot} and $\Phi_{film-vac}$ are found, $\Phi_{film-sub}$ can be calculated and the degree of confinement potential in the quantum well can be assessed.

2.3 Magnetotransport

Electrical and magnetotransport characterization of thin films can provide a plethora of information on basic material properties and serve as the most direct method to explore potential applications in electronic devices. Experiments can range from the diffusive classical transport to the ballistic or diffusive quantum transport regime, depending on the material properties and device geometry [135]. In this section, we will focus on electrical measurements for extracting fundamental information such as charge carrier concentrations, mobilities, and carrier scattering times.

2.3.1 Hall effect and length scales

The Hall measurement technique is based on the Lorentz force law: when a magnetic field is applied perpendicular to a current path flowing in a material, a voltage difference is generated across the material in a direction perpendicular to both the current and the magnetic field. This voltage difference, known as the Hall voltage, V_H is given as:

$$V_H = \frac{R_H B I}{d}$$

where R_H is the Hall coefficient, B is the magnetic field, I is the current, and d is the thickness of the conducting sample/film. In a simple model of a three-dimensional (3D) sample with a single type of charge carrier, the Hall coefficient provides information on the carrier density:

$$R_H d = \rho_{xy} = \frac{1}{n^{3D} q}$$

ρ_{xy} being the Hall resistivity, q contains information on the sign and charge of the carrier (-1.602×10^{-19} C for electrons), and n^{3D} is the 3D carrier density. For a two-dimensional (2D) system, the equation is updated to find the 2D carrier density, n^{2D}: $n^{2D} = n^{3D} d$. In addition to the density and type of charge carriers participating in transport, one can also extract their mobility μ by combining Hall measurements with longitudinal resistance measurements which provide information on the sheet resistance R_s:

$$R_s d = \rho_{xx} = \frac{1}{n^{3D} q \mu}$$

Both measurements require a 4-point-probe setup [136] that includes the van der Pauw geometry [137] shown in Figure 2.8A or the Hall bar presented in Figure 2.8B [138]. In section 2.3.3, we will discuss various scaling effects of Hall and longitudinal resistance with a magnetic field. The charge carrier mobility relates to the relaxation time (τ) and effective mass (m*):

$$\mu = \frac{q\tau}{m^*}$$

High carrier mobilities are typically obtained in high-quality epitaxial systems with low defect densities (leading to fewer scattering events) and relatively small effective mass (determined by the electronic band structure). In the diffusive transport regime where the Drude model applies (that is, scattering takes place on length scales that are small compared to the size of the sample) one can find the mean free path, l, from the measured scattering time extracted from the sample mobility. The mean free path is defined as the average distance that charge carriers travel before backscattering:

$$l = v_F \tau$$

Where the Fermi velocity, v_F relates to the carrier density via: $v_F = \frac{\hbar k_F}{m^*}$ and the Fermi wavevector, k_F in a 2D/3D system equals:

$$k_F = \sqrt{\frac{4\pi n^{2D}}{g_s g_v}} = \sqrt[3]{\frac{6\pi^2 n^{3D}}{g_s g_v}}$$

g_v being the valley degeneracy, and g_s is the spin degeneracy.

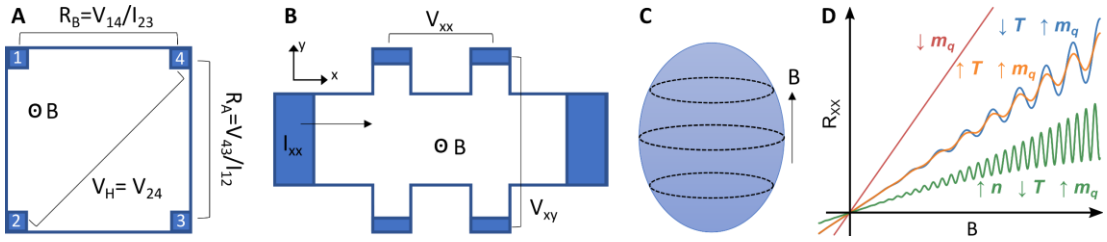

Figure 2.8. (**A**) Schematic of a van der Pauw sample in square geometry (**B**) Schematic of a standard 6-contact Hall bar showing the longitudinal (V_{xx}) and transverse (V_{xy}) voltage (**C**) Sketch of Landau tubes for an ellipsoidal Fermi surface. As the magnetic field increases, the Landau level separation increases as they move through the Fermi surface, leading to quantum oscillations. (**D**) Schematic showing the variation in the amplitudes and frequency of sdH oscillations for materials with high, ↑, and low, ↓, quantum mobility, m_q, as a function of temperature, *T*, and carrier density, *n*. The slopes are changed for clarity.

Scattering lengths depend on the scattering mechanism and the physical quantity that is preserved, such as elastic (l_e) / inelastic(l_i) lengths for energy conservation, or phase-breaking lengths (l_φ) for coherent interference. The current path in the sample (L) and the ratio of different mean free paths are important as they define different transport regimes. For example, the elastic scattering length, l_e (energy being conserved when scattering from impurities, boundaries, etc.) defines the ballistic ($L \leq l_e$) vs. diffusive ($L \gg l_e$) transport regimes. Quantum diffusive ($L > l_\varphi > l_e$) vs. classical diffusive ($L > l_e > l_\varphi$) transport typically depends on the sample temperature and the type of scattering sites.

2.3.2 Shubnikov-de Haas oscillations

In high magnetic fields, the quantization of charge carrier states also needs to be considered and depends on the ratio of the cyclotron radius, l_c, vs. the mean free path. The cyclotron orbit ω_c and cyclotron radius l_c are defined as:

$$\omega_c = \frac{qB}{m^*} \quad , \quad l_c = \frac{\hbar k_F}{eB}$$

When $\omega_c \tau_q = \mu_q B \gg 1$ (τ_q and μ_q being the quantum scattering time and mobility) carriers move in small cyclotron orbits prior to being scattered by other means, leading to oscillatory magnetoresistance as the magnetic field strength is changed. The cyclotron orbits in k-space are confined in their area to the Fermi surface in tubes called Landau levels (see Figure 2.8C) with an energy spacing of $\hbar\omega_c$, and the area is quantized in units proportional to *B.* As the magnetic field increases the number of Landau levels crossing the Fermi contour area changes, leading to variations in carrier densities. In a 3D Fermi surface, the highest sensitivity to area variations is obtained for the extremal cyclotron orbits. These periodic quantum oscillations in resistance ΔR vs. 1/B are known as the Shubnikov–de Haas (SdH) effect, see Figure 2.8D.

The SdH effect is observed in high-mobility materials at high magnetic fields and low temperatures. Information on the Fermi surface geometry, scattering times, density, and effective mass of charge carriers is typically obtained and it serves as a powerful approach for characterizing high-quality crystals. High quantum mobilities are necessary for SdH oscillations in order to avoid scattering prior to the completion of a cyclotron orbit. Moreover, the intensity of the oscillations depends on the sample temperature due to the thermal broadening of the quantum states, therefore –

$$k_B T < \hbar\omega_c = \frac{\hbar q B}{m_q^*}$$

Quantum oscillation carrier densities are calculated from the fast Fourier transform frequency of the SdH oscillations f_{FFT}, using the Onsager relation: $f_{FFT} = \frac{\Phi_0 A_{ext}}{2\pi^2}$. Φ_0 is the magnetic flux quantum, and A_{ext} is the extremal orbit area for the band. For an ellipse cross-section: $A_{ext} = \pi k_F^a k_F^b$ (a and b being the minor and major axes). The Fermi surface volumes are then calculated from the SdH Fermi wave vectors, assuming the Fermi surface shape is known either from magnetic field angle-dependent measurements (i.e. the magnetic field is rotated from the sample normal towards the current path) or other techniques such as DFT/ARPES and more.

2.3.3 Magnetoresistance and multicarrier analysis

In contrast to the stringent requirements necessary to observe the SdH effect, Hall and longitudinal magnetoresistance measurements can be performed in low-mobility/disordered systems and at relatively high temperatures. However, the interpretation of the results is typically challenging in multicarrier/valley systems where the number of parameters might be relatively large. Moreover, the analysis does not account for changes in scattering times/mechanisms as the magnetic field is varied, such as metamagnetic transitions, defect scattering, or quantum diffusive localization effects.

In typical single-carrier systems, longitudinal magnetoresistance increases quadratically with the magnetic field and saturates at high fields (for a closed cyclotron orbit) [139]. The Hall resistance also increases linearly with the magnetic field. However, a non-saturating linear magnetoresistance is possible also in a single-carrier system for two cases: (a) A highly-

ordered high-mobility crystal at the extreme quantum limit, where only a single quantum state is populated; and (b) an inhomogeneous conductor with a high-mobility matrix containing low-mobility islands leading to multiple- electron scattering [140]. Finally, magnetoresistance is also sensitive to geometric effects in metal-semiconductor hybrid structures, which were shown to have extraordinary magnetoresistance [53].

In materials containing more than one type of charge carrier (for example, either due to multiple valleys/bands, or parallel conduction from several layers) the total conductivity of all *N* carriers is assumed to be additive for each carrier type *i*, and one needs to simultaneously fit σ_{xx}^{tot} and σ_{xy}^{tot} in order to obtain a reliable result:

$$\sigma_{xx}^{tot} = \sum_i^N \sigma_{xx}^{i} = \sum_i^N \frac{q_i n_i \mu_i}{1+(\mu_i B)^2} \qquad \sigma_{xy}^{tot} = \sum_i^N \sigma_{xy}^{i} = \sum_i^N \frac{q_i n_i \mu_i^2 B}{1+(\mu_i B)^2}$$

and the longitudinal and Hall resistivity are then found:

$$\rho_{xx} = \frac{\sigma_{xx}^{tot}}{(\sigma_{xx}^{tot})^2+(\sigma_{xy}^{tot})^2} \qquad \rho_{xy} = \frac{\sigma_{xy}^{tot}}{(\sigma_{xx}^{tot})^2+(\sigma_{xy}^{tot})^2}$$

The result of these added terms is that in multicarrier systems a non-linear Hall resistance can emerge, and the longitudinal resistivity can continuously rise even at high fields. Under a specific condition of high charge carrier mobilities, and nearly equal hole and electron charge densities (i.e. charge compensation) and mobilities, the longitudinal resistance is expected to rise quadratically with magnetic field without saturating [139]. This extreme magnetoresistance (XMR) condition is fulfilled by several trivial and topological semimetals [55,61] exhibiting high carrier mobilities and charge compensation.

3 Epitaxial growth, magnetoresistance, & electronic band structure of GdSb films

3.1 Introduction

Motivated by observations of extreme magnetoresistance (XMR) in bulk crystals of rare-earth monopnictide (RE-V) compounds and emerging applications in novel spintronic and plasmonic devices based on thin-film semimetals, we have investigated the electronic band structure and transport behavior of epitaxial GdSb thin films grown on III-V semiconductor surfaces. The Gd^{3+} ion in GdSb has a high spin S=7/2 and no orbital angular momentum, serving as a model system for studying the effects of antiferromagnetic order and strong exchange coupling on the resulting Fermi surface and magnetotransport properties of RE-Vs. To explore the potential for novel magnetoresistive RE-V semimetal devices, it is necessary to map the electronic structure of RE-V thin films and study the degrees of freedom that could help tune magnetoresistance, such as magnetic order transitions, quantum confinement effects, and defect scattering.

Here, we report the growth, ARPES, and magnetotransport of epitaxial lattice-matched GdSb films grown on III-V buffer layers via MBE. To our knowledge, this is the first report on the synthesis conditions and electronic properties of epitaxial GdSb thin films. As a member of the RE-V family, GdSb shares the common features of antiferromagnetic ordering [141] and an unusually high magnetoresistance [142], with previous magnetotransport reports of GdSb bulk crystals presenting magnetoresistance values up to 12500% [142]. From a thin-film synthesis perspective, GdSb is a relatively straightforward RE-V to grow epitaxially on III-V semiconductors. Lighter rare-earth elements tend to be more reactive [143] and form more

stable competing RE-Sb_2 phases [144]. Gd-V compounds serve as favorable model systems for studying magnetoresistive and magnetic scattering behavior in RE-V semimetals due to a relatively simple magnetic phase diagram, lack of orbital angular momentum, and deep-lying occupied 4f bands leading to a smaller *p-f* mixing than observed in Ce-Vs [52].

GdSb is a classical Heisenberg antiferromagnet (AFM), where Gd^{3+} ions with S=7/2, L=0 order as a type-II AFM at 24 K [141,145], such that the Gd magnetic moments are ordered ferromagnetically along the $\langle 11\bar{2} \rangle$ directions, and adjacent {111} planes are coupled antiferromagnetically. The magnetic phase diagram of GdSb has an AFM phase that transitions to a spin-flop phase at very low fields (0.2 T at 4 K, B||$\langle 001 \rangle$). As the magnetic field increases, the spin-flop phase remains stable and linearly increases in magnetization until a critical field of 34.5 T is reached [141]. Due to the large distance of the *4f* electrons from the Fermi level, the occupied *4f* levels have weak coupling to the valence band *p*-orbitals, whereas significant *d-f* Coulomb exchange interaction results in exchange splitting of the electron conduction band when magnetic fields are applied. In the spin-flop phase, the exchange splitting of the electron pocket band should increase linearly with magnetic field due to spin reorientation. The magnetization in GdSb was shown to increase linearly up to the critical field of 34.5 T, after which GdSb enters a forced ferromagnetic phase [141].

Apart from magnetoresistive devices, synthesizing RE-Vs as thin films subject to biaxial strain and confinement effects also presents an opportunity to tune their band-structure topology. While only RE-V bulk crystals with high spin-orbit coupling and large lattice parameters (XBi, X=La-Gd) were found to host topological semimetal states [146–148], recent studies suggest that Sb- and As-based RE-Vs subject to high pressure could also transition into a nontrivial topological phase [149,150]. Having a lattice parameter *a*=6.219 Å [142], GdSb is

uniquely positioned between InSb (6.4794 Å) and GaSb (6.0959 Å)/AlSb (6.1355 Å), allowing tensile and compressive biaxial strain to be tuned by the underlying semiconducting III-V buffer layer structure. Further, epitaxial films of GdSb can serve as high-quality buffer layers that also aid as diffusion barriers for integrating reactive layers on III-V semiconductors [151]. The synthesis of thin films of GdSb also opens up more opportunities to study quantum size effects in RE-Vs, where quantum confinement was shown to alter carrier compensation and differentially affect the mobility of electron- and hole-like carriers [57,58,152]. In addition to improving the fundamental understanding of magnetotransport properties in GdSb, our electronic structure study can be used to engineer plasma resonance frequencies in RE-Vs and semimetal films for plasmonic mid-infrared optoelectronic applications [153].

3.2 MBE growth of GdSb

The GdSb films were grown in a modified VG V80H III-V MBE growth chamber with a base pressure $<5x10^{-11}$ Torr. High purity Gd (4N, Materials Preparation Center, Ames Laboratory), Ga (7N, United Mineral and Chemical Corporation, UMC), Al (6N5, UMC) In (7N, UMC), and Be were evaporated from effusion cells, and Sb (7N, UMC) was supplied from a valved cracker cell as Sb_2. GaSb wafers (Wafer Technology Ltd.) were mounted on tungsten or tantalum substrate holders by Gallium bonding, and the temperature of the substrate was measured using a thermocouple and infrared pyrometer set to an emissivity of 0.62-0.67 (calibrated at 540°C, the thermal desorption temperature of the GaSb surface oxide under Sb_2 overpressure). Epi-ready semi-insulating GaSb (001) wafers were used for magnetotransport measurements, with significant charge carrier freeze-out expected below 80

K. For photoemission and scanning tunneling microscopy (STM) studies, conductive *p*-type Zn:GaSb (001) wafers were used, followed by *p*-type Be-doped III-V buffer layers.

Atomic fluxes for Al, Ga, In, and Sb_2 were measured with an ion gauge (excluding Gd to avoid cathode poisoning due to the high reactivity and oxidation tendency of Gd [120]) and calibrated against RHEED intensity oscillations for Sb-rich surface reconstructions (In, Ga, Al flux) and Ga-rich surfaces (Sb flux) on GaSb (001). The GdSb RHEED intensity oscillations during growth were taken after several monolayers of GdSb film growth so as not to be affected by an embedded growth mode [46].

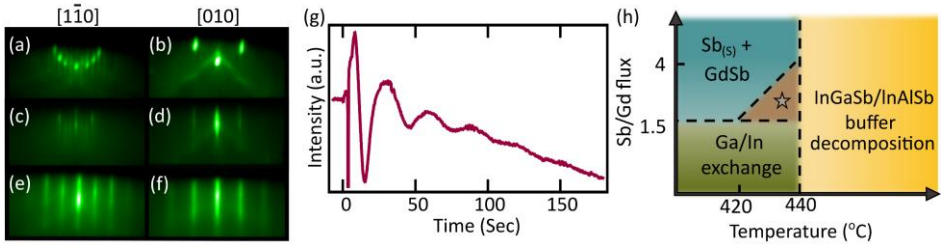

Figure 3.1. RHEED patterns measured along the [1$\bar{1}$0] and [010] azimuths for the (**a-b**) GaSb substrate, (**c-d**) InAlSb metamorphic buffer layer, and (**e-f**) GdSb film. (**g**) GdSb RHEED intensity oscillations, and (**h**) a schematic of the experimental MBE growth window diagram, showing ideal GdSb growth conditions marked by a star. Figure reprinted with permission from [154].

After GaSb (001) native oxide desorption, a ~100 nm thick GaSb buffer layer was grown, followed by a ~1μm metamorphic buffer layer grown to match the GdSb bulk lattice constant of 6.219Å [142]: $In_{0.25}Al_{0.75}Sb$ for transport measurements (referred to as InAlSb), and Be-doped $In_{0.32}Ga_{0.68}Sb$ (referred to as InGaSb) for photoemission studies. The buffer layer was nucleated at 340-350°C and grown <370°C at a rate of ~2.2 Å /sec. The coherent growth of lattice-matched films was studied *in situ* with RHEED (see Figure 3.1) and confirmed *ex situ* with X-ray diffraction (XRD) measurements (see Figure 3.2). Streaky RHEED patterns were seen in all layers, suggesting smooth and epitaxial films. Figure 3.1(a-f) shows the evolution of the RHEED pattern during GdSb (001) epitaxial growth. An Sb-rich C(2×6)/(1×3) surface reconstruction is present for all III-V layers, which evolves into a (1×1) un-reconstructed

surface diffraction pattern upon GdSb growth. The GdSb growth rate was 0.03 unit cells/sec (0.187Å/sec), yielding weak RHEED intensity oscillations (Figure 3.1(g)). The elemental Gd flux was also determined *ex situ* from the finite film thickness fringes measured by XRD. Nearly stoichiometric growth conditions resulted in the highest quality GdSb, especially when grown directly (strained) on GaSb.

Maintaining the narrow growth window of GdSb (see Figure 3.1(h)) becomes challenging for thick film growth (>30 nm) due to unintentional radiative heating from the Gd effusion cell changing the substrate temperature. Growths with high Sb_2 fluxes or too low temperatures (<420°C) led to a significant amount of solid Sb adsorbed on the surface resulting in a hazy polycrystalline ring observed in RHEED, whereas too low of an Sb_2 flux or high-temperature growths led to Ga and In adatoms to accumulate on the surface and react with excess Gd, determined from 3D diffraction patterns seen in RHEED. A thin interlayer (~4 monolayers) of AlSb was added in an effort to expand the GdSb growth window to higher temperatures and lower Sb flux (Figure 3.1(h)) while mitigating any potential Gd-In interfacial exchange reactions [143] or displacement of In atoms to the surface [46]. Following GdSb growth and before removal from vacuum, the GdSb films were protected from degradation in the air by capping in another interconnected vacuum system with an amorphous AlO_x layer deposited by e-beam evaporation of Al_2O_3 at room temperature.

Structural quality, crystal order, and film thickness were monitored *ex situ* with triple-axis XRD and X-ray reflectivity (XRR) oscillations. Figure 3.2(a) shows a wide-range θ-2θ XRD scan of the GdSb film grown on a GaSb (001) substrate and InAlSb buffer layer, revealing no additional peaks from impurity phases. A high-resolution triple-axis XRD scan near the (002) peak in Figure 3.2(b) shows exact out-of-plane lattice matching between the GdSb film and

the InAlSb metamorphic buffer layer. The Pendellösung fringes indicate abrupt interfaces, and the extracted GdSb thickness values agree with *in situ* flux calibrations using RHEED oscillation. A schematic of a typical heterostructure grown for magnetotransport measurements is shown in an inset in Figure 3.2(b).

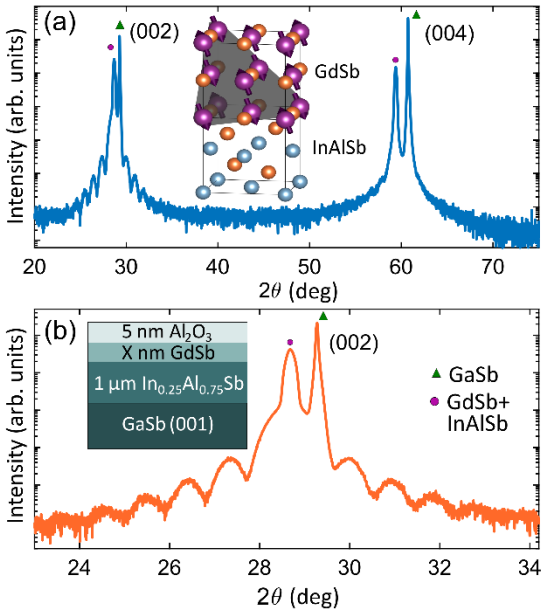

Figure 3.2. (**a**) Out-of-plane θ-2θ XRD scan for a 10-nm-thick lattice-matched GdSb film grown on InAlSb/GaSb (001). The InAlSb and GdSb layers are indexed with a circle, and the GaSb substrate with a triangle. (Inset) Crystal structure and epitaxial relationship of the GdSb/III-V structure, with the magnetic structures for the type-II AFM ground state of GdSb shown. (**b**) Zoom-in on the (002) reflection; the inset shows the sample heterostructure. Figure reprinted with permission from [154].

Surface cleanliness, stoichiometry, and Gd speciation were monitored with *in situ* X-ray photoelectron spectroscopy (XPS). The XPS measurements of a 30 nm thick GdSb film in Figure 3.3(a-c) were performed at UC, Santa Barbara, using monochromic Al kα_1 as the X-ray source (1486.6 eV) at an emission angle of 55° in a Surface Science Laboratories SSX-100 ESCA system. XPS analysis of the Gd 4*d*, 3*d*, and Sb 3*d* core levels in Figure 3.3(a-c) confirms stoichiometry is achieved (Sb:Gd=1.04:1, within the uncertainty of XPS without a reference standard sample and accounting for the photoemission cross sections). The Gd 3*d* and 4*d* spectra and loss features are consistent with previous XPS studies of bulk GdSb [155].

The GdSb films showed no signs of contamination *in vacuo*, i.e., the oxygen and carbon levels at the surface were below the XPS detection limit.

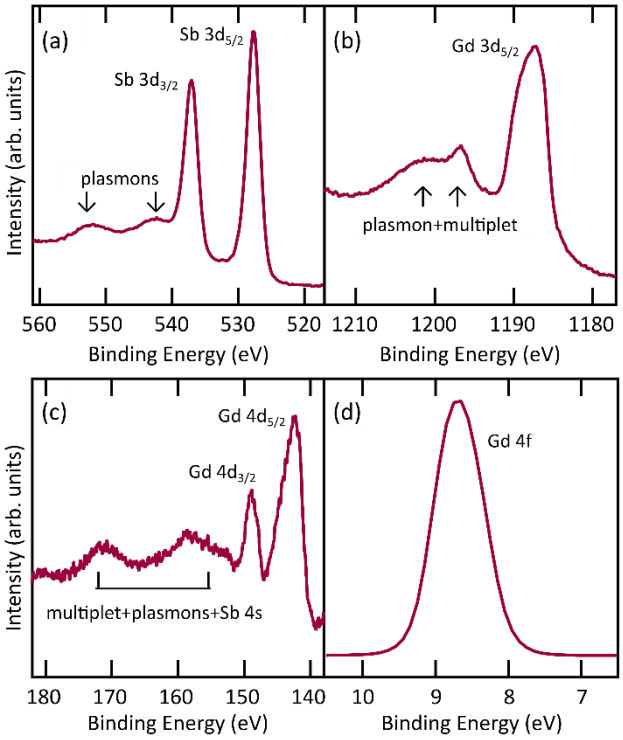

Figure 3.3. *In situ* XPS of the (**a**) Sb 3d, (**b**) Gd $3d_{5/2}$, (**c**) and Gd 4d core levels. (**d**) UPS scan of the Gd 4f core level collected for *in vacuo* transferred GdSb films. Figure reprinted with permission from [154].

Vacuum ultraviolet (VUV)-light ARPES measurements in the 20-100 eV range were performed on 4- and 20-nm-thick (i) *in vacuo* transferred GdSb films, and (ii) Sb-capped, air-exposed, and Sb-decapped GdSb films. A custom-built vacuum suitcase with a base pressure $<1\times10^{-10}$ Torr was used for transferring films from the growth chamber at the University of California, Santa Barbara, to beamline 10.0.1.2 at the Advanced Light Source (ALS) in Berkeley. At the SLAC National Accelerator Laboratory, Sb-capped films were studied at beamline 5-2 at the Stanford Synchrotron Radiation Lightsource. Ultraviolet photoemission spectroscopy (UPS) of the Gd 4*f* and Sb 4*d* core levels was collected for the *in vacuo* ALS transferred GdSb films and the SLAC Sb-capped films (after Sb desorption). We confirmed

the chemical stability of the GdSb films in both cases by the absence of any oxidized components or oxygen 2*s* peak. In Figure 3.3(d), a single Gd 4*f* peak is observed at 8.68 eV, indicating no oxidation. Our UPS scan agrees with the predicted deep-lying energy position of the occupied 4f levels in our DFT calculations, ~8.2 eV below the Fermi level.

The film surface morphology was investigated with Nomarski optical microscopy and scanning probe microscopy. The final surface morphology and nucleation of the GdSb films were studied at room temperature with *in situ* scanning tunneling microscopy (STM) and *ex situ* atomic force microscopy (Figure 3.4)**.** In Figure 3.4, the cross-hatched pattern originates from misfit dislocations in the underlying relaxed InAlSb buffer layer.

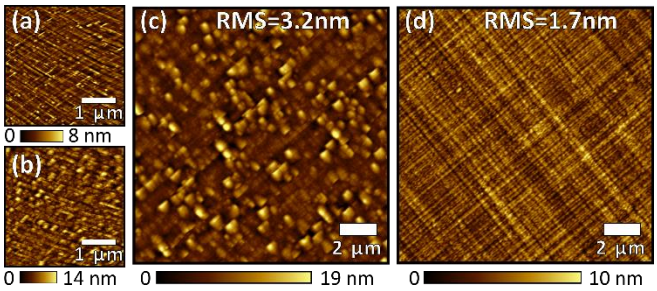

Figure 3.4. *In situ* STM images of (**a**) III-V lattice-matched buffer layer: 2-nm AlSb/200-nm $In_{0.25}Al_{0.75}Sb$/GaSb (001), and (**b**) 30-nm-thick GdSb grown on the lattice-matched buffer-layer structure. *Ex situ* atomic force microscope image of Al_2O_3 capped 30-nm GdSb films grown on the $In_{0.25}Al_{0.75}Sb$ layer (**c**) without and (**d**) with an AlSb interlayer. Figure reprinted with permission from [154].

Figure 3.4(c-d) shows a decrease in the surface roughness of 30-nm GdSb films grown with an AlSb interlayer, suggesting the higher stability of the AlSb surface at low Sb_2 overpressure could play a role in high-quality GdSb growth. A relatively flat surface is achieved for the metamorphic buffer layer grown at low temperatures, as measured with *in situ* STM in Figure 3.4(a). From the similar topography range in Figure 3.4(b-d), a thickness of 5 nm of the amorphous Al_2O_3 capping layer appears to passivate the GdSb surface without continuing reactions after removing the sample from a vacuum environment.

3.3 Electronic band structure of unstrained GdSb studied via ARPES & DFT

ARPES measurements performed on a 20-nm-thick GdSb film are presented in Figure 3.5 and Figure 3.6. In Figure 3.5(b), we observe an ellipsoidal electron pocket (α) at the bulk X point, two nearly spherical light-hole (β) and spin-orbit split-off bands (γ) at the bulk Γ point, and a warped heavy-hole band (δ) resembling a square Fermi surface. The Fermi surface of the GdSb film is consistent with previous reports for other RE-Vs [55,147,148,156–158] and our DFT calculations in Figure 3.5(g). Fits to all bulk bands near the Fermi level are presented in Figure 3.6, and the resulting Fermi wave vector values, band extrema, and calculated carrier densities (Table 3.1) are compared against DFT-extracted values (Table 3.2). The ARPES Fermi wave vectors are closer to the AFM phase DFT predictions than the nonmagnetic phase. Based on the estimated Fermi volumes from the ARPES data, the 20-nm-thick GdSb film shows similar hole and electron carrier densities, with an electron/hole ratio of n_e/n_h=0.84. The 4-nm-thick GdSb films studied with ARPES also showed a semimetallic band structure.

The 20-nm-thick GdSb film displays multiple quantum-well states confirming smooth conformal growth. The hole band quantum-well states are seen in Figure 3.5(c-d) and are particularly visible near $\bar{\Gamma}$ for the γ pocket and $\bar{M}$ for the δ pocket in Figure 3.6(a-d). The electron pocket quantum well states are presented in Figure 3.5(e) and Figure 3.6(e-h). At 20 nm, the GdSb film is still not at the bulk limit for all charge carriers, evidenced by the high number (>10) of finely-spaced quantum-well subbands in the δ hole pocket. The electron pocket shows fewer subbands crossing the Fermi level with a larger energy separation (Figure 3.5(e)) due to the smaller effective mass along the minor axis of the ellipsoidal electron pocket, suggesting that the electron band is strongly affected by quantum confinement.

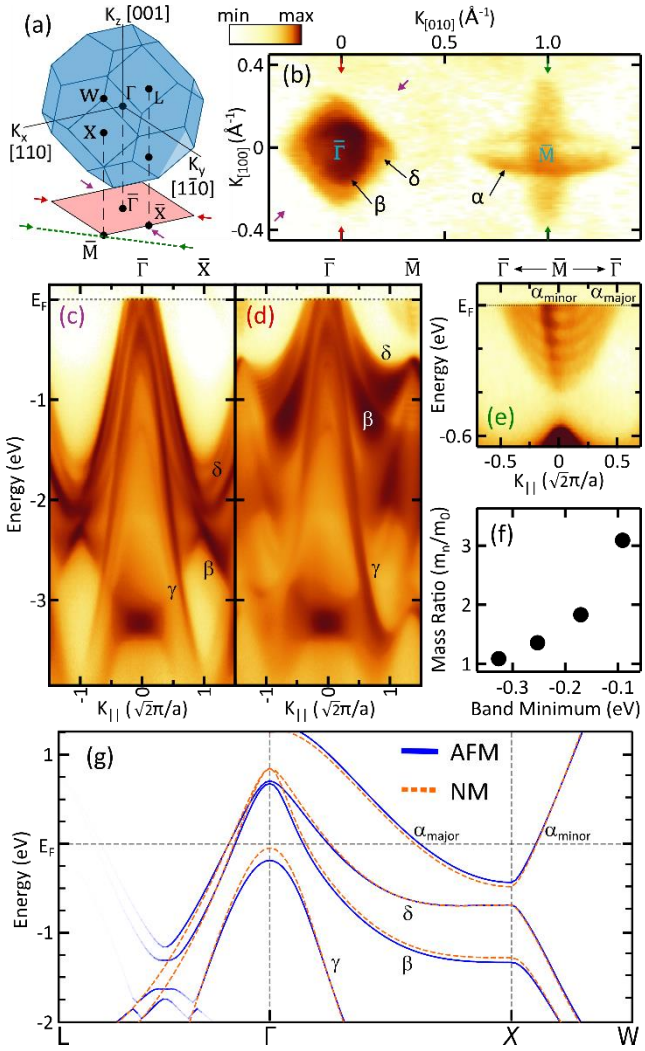

Figure 3.5. (**a**) Rocksalt bulk three-dimensional Brillouin zone and (001) surface projection, with E-k scan directions in panels (**c-e**) highlighted with arrows along $\bar{X}-\bar{\Gamma}-\bar{X}$ (purple, **c**), $\bar{M}-\bar{\Gamma}-\bar{M}$ (red, d), and $\bar{\Gamma}-\bar{M}-\bar{\Gamma}$ (green, e). (**b**) $h\nu$=60 eV (k_z=Γ) Fermi surface map at E_F showing the hole-like bands (β, δ) and electron-like (α) bands. (**c-d**) Band dispersion of the hole pockets and (**e**) the electron pockets, presenting quantum-well states in all three bands. (**f**) Relative mass enhancement of electrons in the quantum-well subbands (m_n) with respect to the lowest level mass (m_0) as a function of the minimum band energy. (**g**) DFT-calculated band structure of GdSb in the antiferromagnetic (AFM) and nonmagnetic (NM) states. The AFM gap is predicted to form along the ⟨111⟩ direction, and the spectral weight of the AFM folded band along $\Gamma-L$ is reflected in the line transparency. Figure reprinted with permission from [154].

Measurements of the electron pocket (Figure 3.5(e)) along $\bar{\Gamma}-\bar{M}-\bar{\Gamma}$ show both the expected $W-X_1-W$ band dispersion from the k_z = Γ zone center along the minor axis, as well as the neighboring Brillouin-zone electron-pocket band dispersions at k_z = X_3 along the electron pocket major axis $\Gamma-X_2-\Gamma$. The nearly identical dispersions along the major axis

of the electron pocket at different photon energies in Figure 3.6(e-h) result from the high k_z broadening expected for the VUV light used in the ARPES measurements [148].

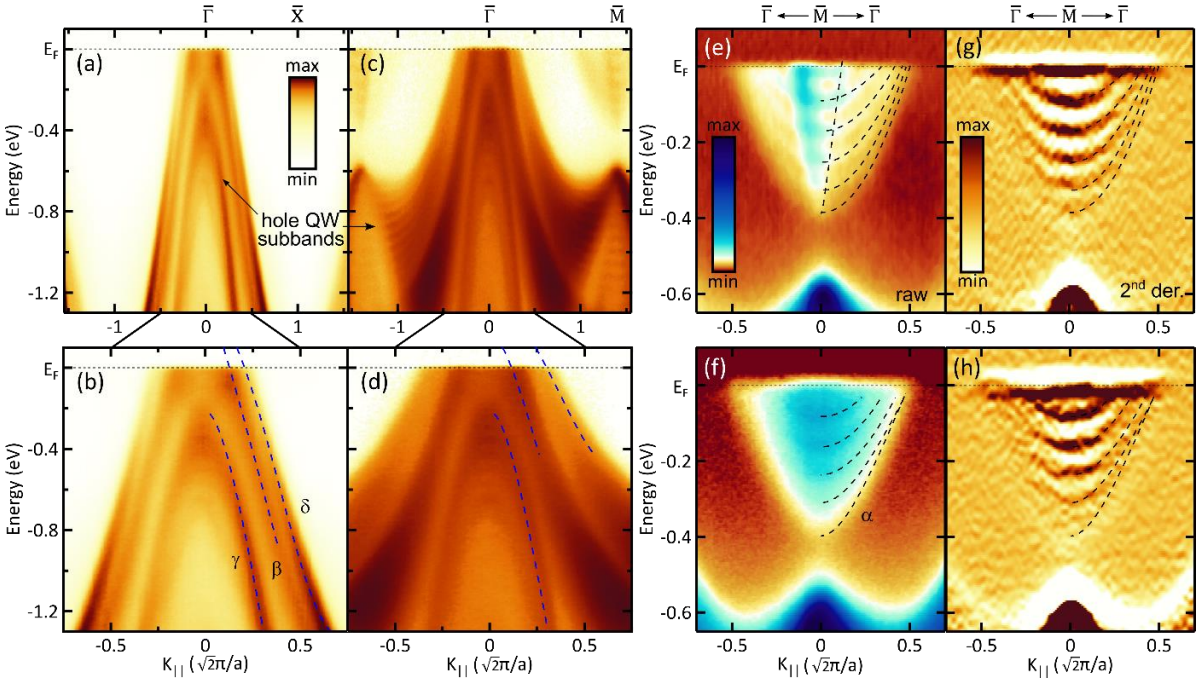

Figure 3.6. ARPES data and overlaid fit to the bands for positive wave vectors. The β, γ, and δ hole pockets along (**a,b**) $\bar{X}-\bar{\Gamma}-\bar{X}$, and (**c,d**) $\bar{M}-\bar{\Gamma}-\bar{M}$. The α electron-pocket minor axis and major axis quantum well subbands along $\bar{\Gamma}-\bar{M}-\bar{\Gamma}$ at the (**e**) Γ plane ($h\nu$=60 eV) and (**f**) X plane ($h\nu$=94 eV). (**g-h**) Second-derivative plots $\frac{\partial^2 I}{\partial E^2}$ of (**e-f**), respectively, enhancing the dispersive features of the raw data. Figure reprinted with permission from [154].

In Figure 3.5(f), the electron pocket effective mass enhancement along the major elliptical axis is calculated for the first four subbands near the Fermi level. Since thick GdSb films are expected to have weak electron correlation effects, the enhanced mass in the subbands with minima closer to the Fermi level is explained by the highly linear and nonparabolic dispersion of the electron pocket. A similar trend was recently observed for IrO_2 [159]. The ability to alter the total carrier density and average effective carrier mass in GdSb quantum-wells through thickness tuning suggests another route to controlling magnetoresistance in RE-V films [160].

The DFT HSE06 band structure calculations for the AFM and nonmagnetic phases are presented in Figure 3.5(g) and appear to overlap at the Fermi level. The HSE06 AFM calculations matched our ARPES measurements and were shown to accurately describe the

carrier concentrations and electronic bandgap at the bulk *X* [60,158]. See Table 3.1 and Table 3.2 for a comparison of ARPES and DFT Fermi wave vectors and band extrema at the *X* and Γ high-symmetry points.

Table 3.1. Fermi surface of a 20-nm-thick GdSb film. Band extrema energy positions, Fermi wave vectors, k_f, effective masses (m^*), and charge-carrier densities (n) obtained from the ARPES measurements. Further details on calculations and data analysis are provided in section 3.5.

Fermi surface	**Band extrema (eV)**		$\mathbf{k_F}$ ($\mathbf{Å^{-1}}$)		$\mathbf{m^*}$ ($\mathbf{m_0}$)		**n** ($\mathbf{10^{20}cm^{-3}}$)
	Γ	**X**					
α	NA	-0.39 (±0.01)	Minor Major	0.084 (±0.014) 0.36 (±0.03)	Minor Major	0.13 (±0.03) 1.73 (±0.29)	$3*n_\alpha$ 2.56 (±0.6)
γ	-0.21 (±0.01)	-3.12 (±0.01)	Does not cross the Fermi level				
β	NA	-1.37 (±0.01)	$\bar{\Gamma}-\bar{M}$ $\bar{\Gamma}-\bar{X}$	0.10 (±0.01) 0.100(±0.003)	$\bar{\Gamma}-\bar{M}$ $\bar{\Gamma}-\bar{X}$	0.19 (±0.02) 0.17 (±0.01)	0.34 (±0.04)
δ	0.31 (±0.06)	-0.60 (±0.01)	$\bar{\Gamma}-\bar{M}$ $\bar{\Gamma}-\bar{X}$	0.23 (±0.03) 0.170 (±0.002)	$\bar{\Gamma}-\bar{M}$ $\bar{\Gamma}-\bar{X}$	0.40 (±0.08) 0.28 (±0.01)	2.72 (±0.8)

Table 3.2. Band energies and Fermi wave vectors obtained from DFT HSE06 calculations for (**a**) the nonmagnetic phase, (**b**) the AFM phase, and (**c**) the FM phase (spin up/down bands, accordingly). Carrier densities extracted from the DFT density of states of the nonmagnetic phase are compared against the analytical calculation of carrier density using the ellipsoid model for the electron pocket and the sphere model for the hole bands (marked with *). Further details on calculations and data analysis are provided in section 3.5.

Fermi surface	**Band extrema (eV)**		$\mathbf{k_F}$ ($\mathbf{Å^{-1}}$)		**n** ($\mathbf{10^{20}cm^{-3}}$)
	Γ	***X***			
α	NA	(a) -0.48 (b) -0.43 (c) -0.13/ -0.61	Minor, Major	(a) 0.103, 0.402 (b) 0.101, 0.383 (c) 0.054/0.111, 0.205/0.461	(a) 4.20 (4.32*), (c) 3.61
γ	(a) -0.05 (b) -0.19 (c) -0.13/-0.26	(a) -3.31 (b) -3.30 (c) -3.15/-3.33	Does not cross the Fermi level		
β	(a) 0.85 (b) 0.67 (c) 0.74/0.44	(a) -1.28 (b) -1.33 (c) -1.29	$\bar{\Gamma}-\bar{M}$ $\bar{\Gamma}-\bar{X}$	(a) 0.151, (b) 0.139, (c) 0.140, 0.133 (a) 0.144, (b) 0.139, (c) 0.148/0.125	(a) 1.18 (1.08*), (c) 0.92
δ	(a) 0.85 (b) 0.67 (c) 1.04/0.91	(a) -0.68 (b) -0.68 (c) -0.63	$\bar{\Gamma}-\bar{M}$ $\bar{\Gamma}-\bar{X}$	(a) 0.254, (b) 0.244, (c) 0.255/0.255 (a) 0.187, (b) 0.183, (c) 0.193/0.178	(a) 3.01 (3.62*), (c) 2.68

The electron-hole bandgap at the bulk *X* point (Figure 3.6(e,f)) is found to be $E_\alpha(X)$-$E_\delta(X)$=0.21 eV and is in close agreement with the AFM phase HSE06 calculations predicting a gap of 0.25 eV in Figure 3.5(g). Near Γ we see the most significant deviation between the AFM and nonmagnetic band structure calculations. In the nonmagnetic phase calculations, the spin-orbit coupled split-off $p_{1/2}$ (γ) pocket nearly crosses the Fermi level. However, as

experimentally observed in Figure 3.6(a-d), the γ pocket-band maxima at the Γ point lies 0.19 eV below the Fermi level, showing that the predictions of the AFM phase (treating the *p-f* interactions explicitly) are in better agreement with experiments. As a type-II AFM, the electron pockets in GdSb are not expected to show any exchange splitting because of the {111} orientation of the ferromagnetic planes. From the spectral weight for the AFM unfolded bands in Figure 3.5(g), we can see that the shadow-band intensity along the $\Gamma - L$ high-symmetry axis is faint near the Fermi level. This can be explained by the relatively weak potential induced by the localized Gd *4f* spin structure and the itinerant Sb *5p* electrons forming the valence band [133]. In our ARPES data, we see no sign of band folding across the AFM Brillouin-zone magnetic boundary (the $\Gamma - L$ axis projected onto $\bar{\Gamma} - \bar{\mathrm{X}}$) in Figure 3.5(c) despite conducting the measurement below the Néel temperature (20 K), possibly due to either short-range AFM ordering or a low photoionization cross-section for the Gd 4*f* level at 60 eV. Nevertheless, evidence of the strong *p-f* mixing predicted to take place in GdSb near the Fermi level [161] is found by comparing the position of the valence bands in DFT calculations for the nonmagnetic phase versus the AFM phase. In the AFM phase, *p-f* mixing shifts the valence band downward and results in hole Fermi wave vectors that agree better with the experimental values.

Finally, DFT calculations of a forced ferromagnetic phase in GdSb (Figure 3.7) were performed assuming all magnetic moments are aligned by a high magnetic field. In such a state significant exchange splitting in the electron *d* band takes place, almost leading to a *p-d* band crossing which would result in a nontrivial band topology and the emergence of Weyl points. Due to the low position of the potential band crossing with respect to the Fermi level (~0.5eV), any Weyl physics contribution to transport is expected to be negligible.

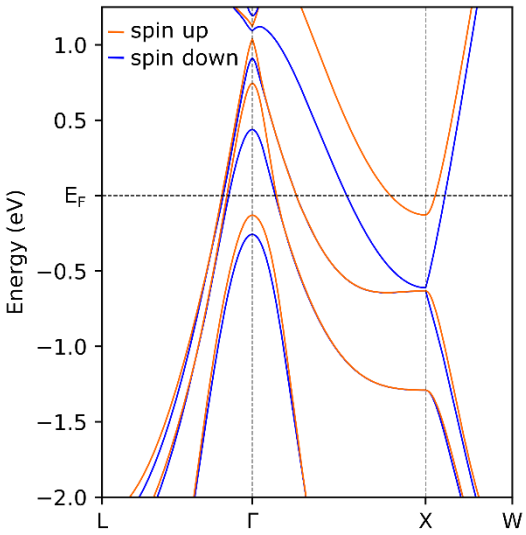

Figure 3.7. HSE06 calculated band structure of GdSb in the forced ferromagnetic state with *f* electrons treated as valence electrons. Ferromagnetic spin-exchange splitting energies for the hole and electron pockets are shown in the spin majority and minority bands. Further details on calculations and data analysis are provided in section 3.5. Figure reprinted with permission from [154].

3.4 Magnetotransport behavior of GdSb films

The temperature dependence of the electrical resistivity for a 10-nm-thick GdSb (001) film is shown in Figure 3.8(a). The total resistivity of the heterostructure (substrate, III-V buffer layer and GdSb film) peaks at 135 K as the InAlSb buffer-layer charge carriers freeze out, indicating the GdSb film has become the lowest resistive path for transport. Upon further cooling, the resistivity adheres to the same trends observed for bulk RE-V crystals [162]: a linear decrease with temperature is observed down to the Néel temperature, where a kink in resistivity at T=25 K (T_N=25.02 and 24.55 K for 10- and 4-nm-thick films, respectively) is followed by a sharp decrease in resistivity. The kink and the sharp drop in resistivity below the Néel temperature indicate that spin-disorder scattering significantly contributes to the total resistivity close to the Néel temperature [163]. Applying higher magnetic fields perpendicular to the film plane increases the resistivity, mainly at lower temperatures.

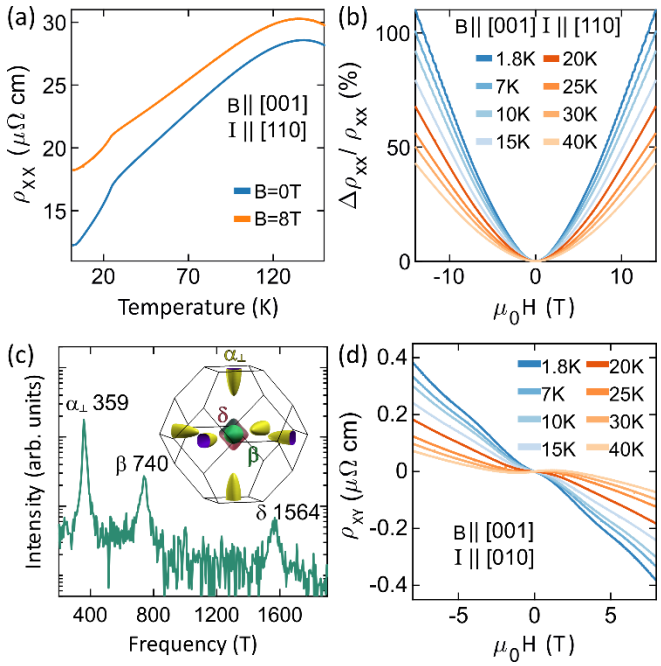

Figure 3.8. Magnetotransport behavior of a 10-nm-thick GdSb film. (**a**) Temperature dependence of the longitudinal resistivity in the epitaxial stack. (**b**) Magnetoresistance vs magnetic field at temperatures below (blue) and near/above (orange) the Néel temperature. (**c**) Log plot of the FFT spectrum of SdH oscillations measured at 1.8 K. (Inset) GdSb Fermi surface. (**d**) Temperature dependence of the Hall resistivity. Figure reprinted with permission from [154].

The small Hall resistivity in Figure 3.8(d) and high longitudinal resistivity upon applied magnetic field (Figure 3.8(b)) both suggest that the films are stoichiometric and have a low defect concentration [142]. Macroscopic scattering sites in LuSb thin films have been shown to promote *p*-type Hall behavior [164], and nonstoichiometric Gd-Vs produce strong negative magnetoresistance behavior at low fields ($\mu_0 H<1$ T) as well as a smaller magnetoresistance [142].

The magnetoresistance at 14 T reaches a maximum value of 110% for a 10-nm-thick film at 1.8 K (Figure 3.8(b)) and 10% for a 4-nm-thick film, the latter being a high value for RE-Vs with a thickness <5 nm [57,58]. SdH oscillations were observed on top of the magnetoresistance background at high magnetic fields (Figure 3.8(b) and Figure 3.9) and were obtained by removing the background using a 5th-order polynomial fit (Figure 3.9(a)). The fast Fourier transform (FFT) of the quantum oscillations reveals three frequencies in Figure 3.8(c),

corresponding to the circular cross-section of the ellipsoid electron pocket at the bulk *X* point along the film plane normal $\alpha_{\perp}$ (359 T) and the two hole pockets, namely, β (740 T) and δ (1564 T) at the Γ point. The Fermi surface of the electron pockets lying at the film (001) plane is not resolved in the FFT spectrum due to the high effective mass of the major-axis band (see Table 3.1). Therefore, we have used the DFT-calculated aspect ratio of the elliptical electron pocket to estimate its Fermi volume. Additional frequencies corresponding to the quantum well subband levels seen in the ARPES measurements were not observed in the quantum oscillations. Subband levels above the ground level (n=0) have a higher probability of lying near the edge of the well and therefore are more affected by interface scattering and would have lower quantum mobilities.

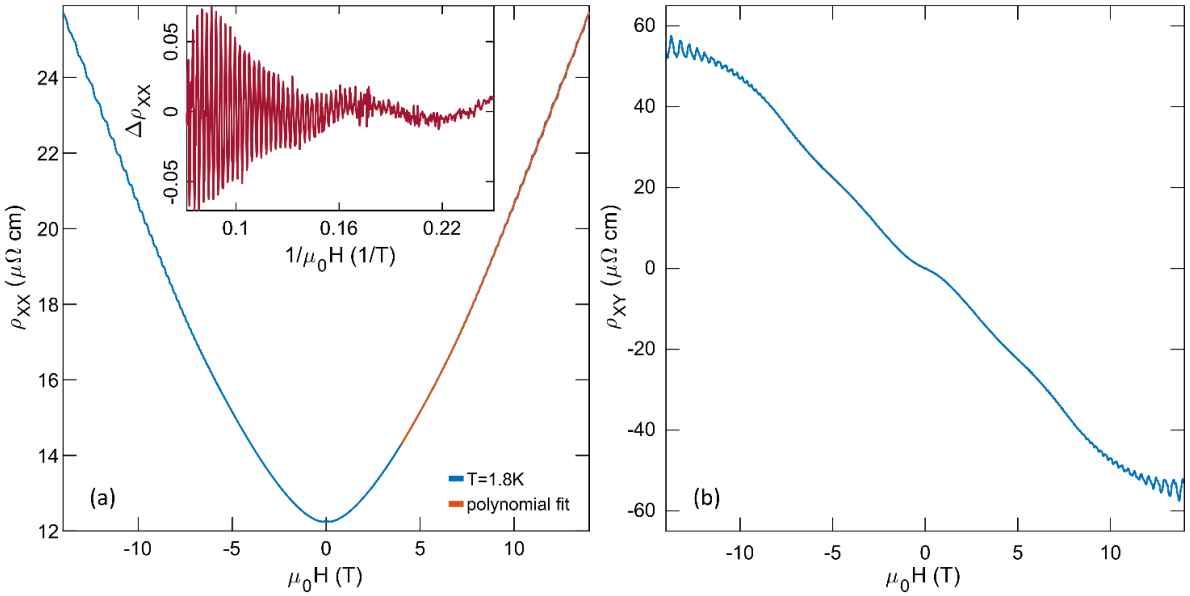

Figure 3.9. (**a**) Longitudinal resistivity and (**b**) Hall resistivity at 1.8 K. (**a**) 5th order polynomial fit used for subtracting the resistivity background. Quantum oscillations vs inverse applied magnetic field are shown in the inset. Figure reprinted with permission from [154].

The FFT amplitude corresponding to the electron pocket $\alpha_{\perp}$ shows a single peak, despite significant exchange splitting. Further information on the SdH oscillations, magnetotransport

models, as well as details on the absence of exchange spin splitting signatures in the electron pocket FFT frequencies are provided in section 3.5.2

Carrier concentrations derived from SdH oscillations are provided in Table 3.3. A similar disparity between ARPES and magnetotransport calculations was seen in earlier RE-V studies [56,156,157]. The lower Fermi wave vectors extracted from ARPES fits are explained by significant k_z broadening at the VUV wavelengths, leading to an underestimated Fermi surface area [148]. The carrier concentrations calculated from both SdH oscillations and the magnetotransport multicarrier fit are in good agreement with previous values of $\sim 4.2\ 10^{20} \mathrm{cm}^{-3}$ found for GdSb bulk crystals [142]. A carrier compensation of n_e/n_h=0.67 is calculated from the SdH oscillations, similar to the ARPES-extracted ratios, yet still far from the nearly exact charge compensation typically assumed for bulk RE-V crystals.

Table 3.3. Fermi surface parameters extracted from SdH oscillations for a 10-nm-thick GdSb film; calculations of the values are described in section 3.5.

Fermi surface	**Frequency (Tesla)**	$\boldsymbol{k_F}$ (Å^{-1})	$\mathbf{n}(\mathbf{10^{20}cm^{-3}})$
$\alpha_{\perp \text{ minor axis}}$	359	0.104	4.32
β	740	0.150	1.14
δ	1564	0.251	5.34

Deviations from an exact carrier ratio n_e/n_h=1 were measured in other bulk RE-V compounds such as DySb [165], LaBi [166], YSb [157], and NdSb [167]. Only a moderate level of compensation may be needed for RE-V compounds to exhibit XMR as long as the carrier mobilities are high. Additional causes for uncompensated carrier concentrations could be more systematic, as the calculations of carrier ratios from Fermi surfaces could depend on the Fermi volume estimation [55]. Lastly, the density of states values from the DFT calculation in Table 3.4 reveals nearly exact carrier compensation. Yet, the computed carrier densities in GdSb also depend significantly on the Fermi level position. A 50 meV shift would cause a relatively steep change in n_e/n_h from 0.7 to 1.5. RE-V thin films are more susceptible to

quantum confinement effects and Fermi level shifts than bulk crystals due to potential charge transfer at the surface/interface.

Table 3.4. Effect of Fermi level position on electron-hole compensation, obtained from DFT calculations for the non-magnetic phase and assuming a rigid band structure.

E_F (eV)	-50 meV	0	+50 meV
n_e ($10^{20} cm^{-3}$)	3.289	4.198	5.234
n_h ($10^{20} cm^{-3}$)	4.863	4.192	3.596
n_e/n_h	0.676	1.001	1.456

Hall coefficients measured for bulk GdSb crystals have shown a transition from *p*- to *n*-type behavior near 5 K [142]. In contrast, in the 10- and 4-nm-thick films a consistent *n*-type behavior is measured in Figure 3.8(d) and Figure 3.10(c), indicating that either a carrier density mismatch or reduced hole mobility leads to a net negative Hall coefficient. Given the temperature dependence of the Hall coefficient at low temperatures <10 K, the higher electron mobility likely leads to *n*-type behavior.

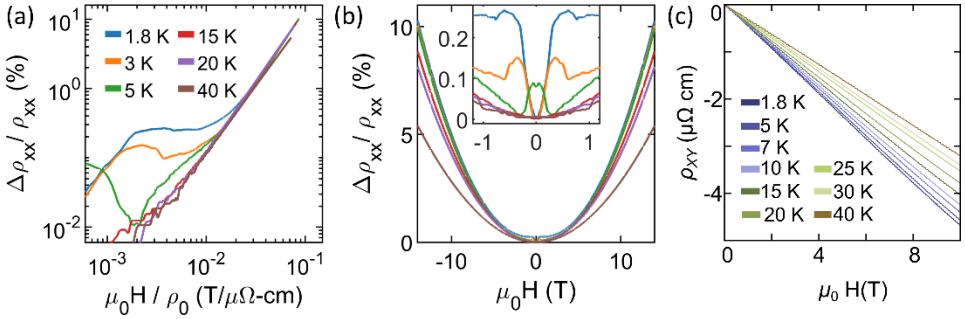

Figure 3.10. 4-nm-thick GdSb film magnetoresistance (MR) at temperatures below, near, and above the Néel temperature. (**a**) Kohler scaling and (**b**) MR vs. magnetic field scaling, (inset) low field MR. Weak antilocalization and metamagnetic transitions are observed at low temperatures for B < 1T. At higher temperatures and higher magnetic fields, the MR scales classically as $MR \propto (\mu_0 H/\rho_0)^{1.58}$. (**c**) Hall resistivity presents a more electron-dominated charge carrier behavior as temperature decreases. Figure reprinted with permission from [154].

In Figure 3.11(a)**,** the Kohler plot [168] shows the effect of magnetic scattering, mobility fluctuations, and electron-electron interactions on varying relaxation times. At low fields, magnetoresistance behavior can be separated into two temperature regimes: low temperatures ($T<<T_N$) and high temperatures ($T\sim T_N$, $T>T_N$). At low temperatures, spin-scattering due to the

spin-flop transition and quantum interference effects leads to a slower, nonparabolic rise in magnetoresistance observed up to ~2 T (~0.15 T/μΩ cm). At high temperatures, quantum interference is suppressed, and spin scattering persists for all fields in the paramagnetic phase and results in a magnetoresistance scaling of $MR \propto (\mu_0 H/\rho_0)^{1.58}$, deviating from the ideal value of 2 due to potential carrier concentration and mobility imbalance.

High magnetic fields are expected to lead to strong exchange splitting at the electron pocket below T_N (see Figure 3.11(b)), potentially leading to a change in carrier compensation. However, based on DFT calculations the ferromagnetic phase of GdSb remains charge compensated (Table 3.2), indicating that no significant carrier concentration change is expected at $T < T_N$ at high magnetic fields. Figure 3.11(c-d) shows the temperature dependence of the charge carrier mobilities obtained from simultaneously fitting the Hall and longitudinal magnetoresistance with a two-band model. The hole and electron carrier density extracted from multiband fits to the magnetotransport data lies between the concentrations extracted from ARPES fits and SdH oscillations, showing an electron-rich carrier density at high temperatures and a nearly compensated carrier concentration below 10 K. This spread in the calculated carrier ratios compared to the other approaches reflects the limited accuracy a simple multicarrier model has in estimating carrier concentrations compared to the more direct methods employed earlier for studying the thin-film Fermi surface. More details on the magnetotransport multiband fit are provided in section 3.5.2.

In Figure 3.11(c), the hole bands show a smaller Hall mobility than the electron pocket at low temperatures. The opposite occurs above the magnetic transition temperature, a trend also observed for bulk single crystals [142]. The higher electron mobility at low temperatures where scattering is reduced is consistent with observations of a smaller effective mass for the

minor axis of the electron pocket vs. the hole bands as measured by ARPES (Table 3.1). After crossing T_N at 25 K to lower temperatures, an accelerated increase in carrier mobilities is seen in Figure 3.11(c), in agreement with the expected suppressed magnetic scattering at low temperatures (mainly affecting electrons due to strong *d-f* scattering). The mobility of electrons and holes shows only a gradual linear-like increase as the temperature drops below 7 K, unlike the nearly exponential rise in mobility observed for bulk Gd-V single crystals [142,169]. The saturation of carrier mobilities at low temperatures suggests that interfacial roughness and surface scattering limit carrier mobilities.

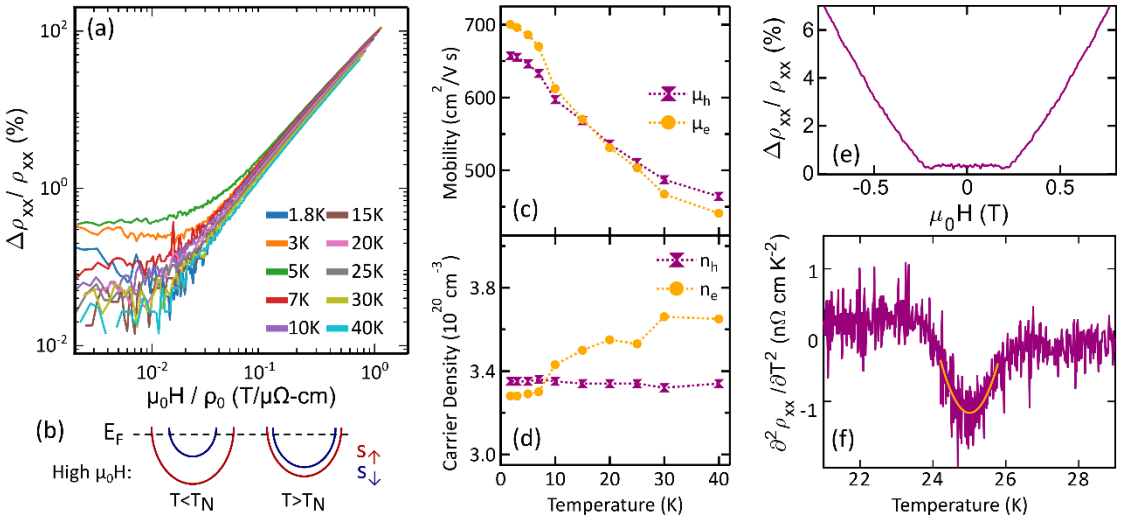

Figure 3.11. (**a**) Kohler scaling of magnetoresistance. (**b**) Schematic of magnetic field-induced exchange interactions in the electron pocket. Temperature dependencies of the mobilities (**c**) of charge carriers and their concentration (**d**) extracted from a two-band fit as described in the main text. (**e**) Low magnetic field magnetoresistance at 1.8 K shows the spin-flop transition. (**f**) Néel temperature extracted from a parabolic fit to the second derivative of the resistivity at B=0 T. Figure reprinted with permission from [154].

From the temperature-dependent resistivity measurements plotted in Figure 3.8(a)**,** the kink and sharp drop in resistivity below the Néel temperature indicate that spin-disorder scattering significantly contributes to the total resistivity close to the Néel temperature. Evidence of the onset of exchange splitting in the spin-flop phase is provided in Figure 3.11(e) by the plateaued magnetoresistance at low magnetic fields, which decreases around 0.2 T and begins to follow

the expected linear/quadratic-like scaling ($MR \propto (\mu_0 H)^n \; n = 1 - 2$) after crossing the spin-flop field [163]. T_N is extracted from the minima in the second-derivative resistivity plots, which are expected to diverge at the Néel temperature (see example fit in Figure 3.11(f)) [145].

3.5 Calculations of Fermi wavevectors, carrier densities, and band positions

3.5.1 ARPES data collection and analysis

ARPES measurements at ALS were conducted at 11K and were acquired with a Scienta R4000 hemispherical analyzer with linear polarized horizontal light. ARPES measurements at SLAC were done for Sb-capped films prepared by thermally desorbing ~1μm of the Sb cap layer at 430°C for at least 1 hour. The SLAC measurements were conducted at a temperature of 20K, obtained using circularly polarized light, and acquired by a Scienta Omicron DA30L hemispherical analyzer. An inner potential of 12eV is determined, similar to previous ARPES studies of RE-Vs [146,148,158]. 20 nm and 4 nm thick films were studied via ARPES.

The experimental Fermi surface volumes in Table 3.1 and Table 3.3 are calculated assuming an elliptical surface for the α bands and spherical surfaces for the hole pockets. The total carrier density is calculated as discussed in [164,170]: $n_e = 3n_\alpha$, $n_h = n_\beta + n_\delta$, $n_{\alpha/\beta/\delta} = \frac{V_F}{4\pi^3}$ and $V_F^{\beta/\delta} = \frac{4\pi}{3} r^3 \; V_F^{\alpha} = \frac{4\pi}{3}\left(k_F^{minor}\right)^2 k_F^{major}$, with the radius r for the hole pockets described below. The Fermi volume model accuracy was confirmed by calculating the carrier density from the DFT Fermi wave vectors in Table 3.2 (marked with *). The degree of compensation between the hole and electron carriers was found to depend mainly on the approximate shape of the δ pocket Fermi volume, similar to earlier observations made for YSb [157] and other La-V compounds [55]. The nonspherical band-warping in the heavy-hole

δ band (and smaller distortion in the light-hole β band) is accounted for by investigating three possible Fermi surface shapes and selecting the model that best describes the DFT carrier density using the DFT Fermi wave vectors for the analytical calculation. The sphere model (b) below best matches the extracted density of states in Table 3.2, and the two other models serve as lower and upper bounds for the carrier density:

a. A Fermi surface composed of two opposite pyramids sharing a base. The square pyramid base area is $A^{\delta} = \left(2k_F(\delta_{\bar{X}\,-\bar{\Gamma}\,-\bar{X}})\right)^2$, the height is $h^{\delta} = k_F(\delta_{\bar{M}\,-\bar{\Gamma}\,-\bar{M}})$, and the total carrier density id $n_{\delta\,(DFT)} = 1.91\times10^{20}$ cm^{-3}.

b. Sphere: The radius being $r = \frac{k_F(\delta_{\bar{X}\,-\bar{\Gamma}\,-\bar{X}})+k_F(\delta_{\bar{M}\,-\bar{\Gamma}\,-\bar{M}})}{2}$ and a total volume $V_F = \frac{4\pi}{3}r^3$, $n_{\delta\,(DFT)}$=3.62 10^{20} cm^{-3}.

c. Average volume of two spheres. $V_F = \frac{\frac{4\pi}{3}(r_1^3+r_2^3)}{2}$ where $r_1 = k_F(\delta_{\bar{X}\,-\bar{\Gamma}\,-\bar{X}})$, $r_2 = k_F(\delta_{\bar{M}\,-\bar{\Gamma}\,-\bar{M}})$, and $n_{\delta\,(DFT)}$=3.80 10^{20} × cm^{-3}.

The magnetotransport quantum oscillation carrier densities in Table 3.3 were calculated from the FFT frequency of the SdH oscillations f_{FFT}, using the Onsager relation: $f_{FFT} = \frac{\Phi_0 A_{ext}}{2\pi^2}$. Φ_0 is the magnetic flux quantum, and A_{ext} is the extremal orbit area for $\alpha_{\perp}, \beta, \delta$, assumed to be circular: $A_{ext} = \pi k_F^2$. We extract the electron pocket semiminor Fermi wave vector, $k_F(\alpha_{minor})$, and the hole pockets $k_F(\beta)$ and $k_F(\delta)$. The electron pocket $k_F(\alpha_{major})$ is calculated assuming an ellipsoidal band with a wave vector ratio of $\frac{k_F(\alpha_{major})}{k_F(\alpha_{minor})} = \frac{3.79}{1}$ (derived from the DFT k_F ratio in the AFM phase; see Table 3.2). The Fermi surface volumes are then calculated from the SdH Fermi wave vectors as described earlier.

To account for the non-parabolic dispersion of the electron pocket, the conduction band is fitted to a hyperbolic function along the semimajor and semiminor (α_{minor}, α_{major}) axes [171]. A quartic polynomial fit to the hole δ pocket was used to assess the valence band maximum binding energy above the Fermi level, and linear fits near the Fermi level were used for extracting the Fermi wavevectors and effective masses of the hole δ and β pockets. Effective masses for all carriers are determined from the first derivative near E_F: $m^* = \hbar^2 k_F \left(\frac{dE(k)}{dk}\right)^{-1}$. Two hole bands (β, δ) cross the Fermi level with an extrapolated peak at 0.31eV and the spin-orbit coupled splitting at the Γ point calculated from ARPES experiments: $E_{\delta/\beta}(\Gamma)$-$E_{\gamma}(\Gamma)$=0.52 eV is consistent with other experimental values extracted for CeSb [148] yet smaller than DFT predictions in Table 3.2 of 0.86 eV.

3.5.2 Magnetotransport models and SdH oscillations

Low-temperature magnetotransport measurements were carried out for 10 nm and 4 nm thick films in a physical property measurement system (PPMS-14T; Quantum Design) using a Van der Pauw geometry with annealed Indium electrical contacts, with R_{xx} measured along [110]. Magnetotransport curves are symmetrized for R_{xx} magnetoresistance measurements and antisymmetrized for the Hall effect (R_{xy}).

In Figure 3.7 we treat the *4f* electrons as valence electrons in a forced ferromagnetic state and calculate E_{ex}=483 meV as the maximum energy separation in the electron pocket expected due to exchange splitting. To evaluate the electron carrier concentration trend predicted from the 2-band fits, the SdH frequency of the electron pocket was studied as a function of temperature from 1.8 K to 15 K and the field range selected for FFT. However, the electron pocket FFT frequency did not shift throughout the field and temperature ranges selected. The

absence of spin-splitting is surprising, yet can be explained by the cancellation of the SdH frequency shifts due to the nearly exact linear magnetic field dependence of the magnetization in the spin-flop phase where the expected frequency shift scales as: $\Delta F = F_{minority} - F_{majority} \propto \left(M - \frac{\partial M}{\partial B} B\right)$ [172,173]. Studies of GdBi bulk single crystals (that present a similar magnetic phase diagram and Fermi surface) also do not have any spin splitting in the SdH FFT spectrum [174]. Based on the critical field of 34.5T for GdSb [141] and the DFT calculated 483 meV exchange energy, at 14T the expected offset between minority and majority spin bands is at least 200 meV (that is before including any Zeeman splitting which should add another contribution to the gap of the spin-split states, albeit a smaller one assuming a g-factor of ~10 [163]).

In Figure 3.12, simultaneous fits to the longitudinal resistivity: $\rho_{xx} = \frac{\sigma_{xx}^{tot}}{(\sigma_{xx}^{tot})^2 + (\sigma_{xy}^{tot})^2}$, and the Hall resistivity: $\rho_{xy} = \frac{\sigma_{xy}^{tot}}{(\sigma_{xx}^{tot})^2 + (\sigma_{xy}^{tot})^2}$, (with $\sigma_{xx}^{tot} = \sigma_{xx}^{h} + \sigma_{xx}^{e}$; $\sigma_{xy}^{tot} = \sigma_{xy}^{h} + \sigma_{xy}^{e}$ and $\sigma_{xx}^{i} = \frac{q n_i \mu_i}{1 + (\mu_i B)^2}$; $\sigma_{xy}^{i} = \frac{q n_i \mu_i^2 B}{1 + (\mu_i B)^2}$) are performed to find the carrier density n_i and mobility μ_i of a given carrier with an elementary charge q. While accounting for more hole bands and adding a mass anisotropy term in the electron pocket mobility values theoretically describes the Fermi surface better, adding these terms did not significantly improve our fits. Therefore, we have kept the number of fitting parameters to a minimum of 4 to avoid overfitting. The longitudinal magnetoresistance fit range was selected at relatively high fields where all magnetoresistance plots have the same scattering mechanism (see Kohler plot in Figure 3.11(a)) to avoid any contributions from spin-scattering at low fields [163] as well as any other potential change in scattering mechanism at low fields which is not accounted for in the two-band model [175].

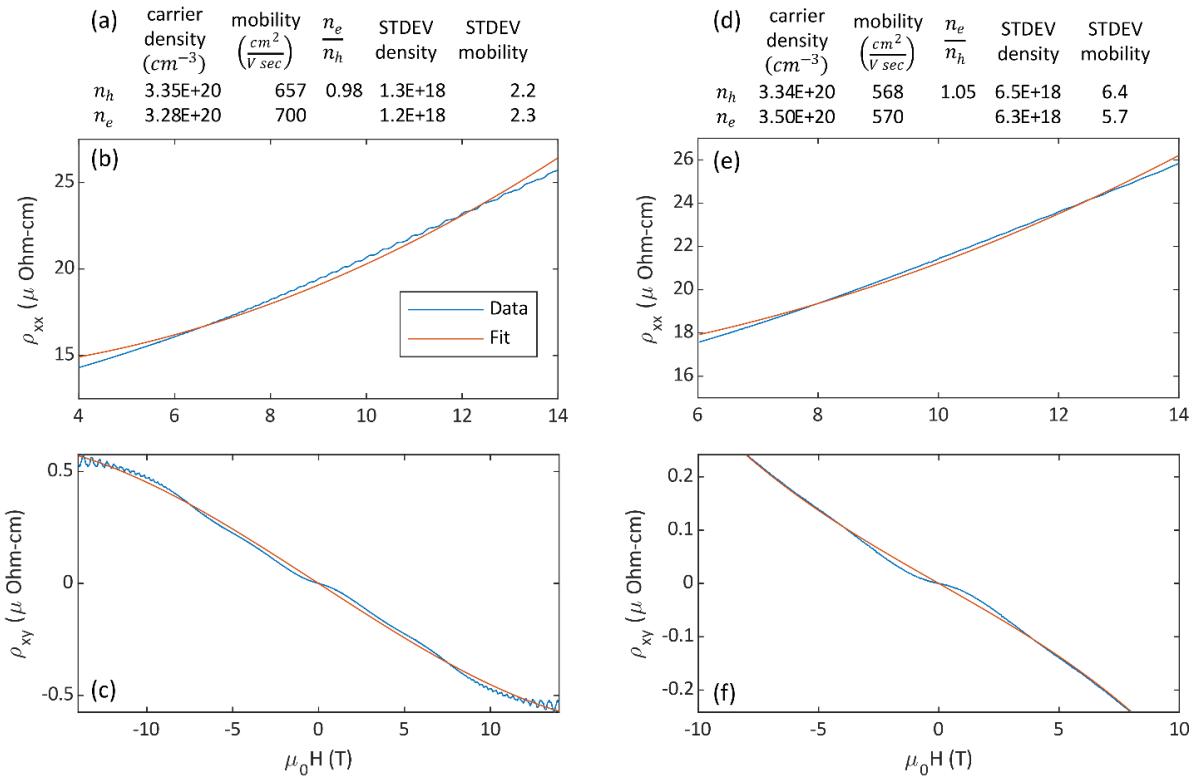

Figure 3.12. Examples of the multicarrier fit results and plots of the longitudinal resistivity (ρ_{xx}) and the Hall resistivity (ρ_{xy}) measured at 2 K (**a-c**) and 15 K (**d-f**) for a 10-nm-thick GdSb film. Figure reprinted with permission from [154].

SdH oscillations in the 4 nm thick GdSb film are only resolved for the electron pocket, with a similar frequency (386 T) as the 10 nm film, in contrast to predictions of the electron pocket being lifted for thinner Gd-V films [58]. Additional frequencies corresponding to the hole pockets (β, δ) and the elliptical cross-section of the electron pocket are not observed in the FFT spectrum of the 4 nm film due to the expected lower quantum mobility for these bands and higher sensitivity of quantum mobilities to small-angle scattering primarily from misfit dislocations in the underlying InAlSb buffer layer. Figure 3.10(a) shows the Kohler plot for the 4 nm thick GdSb film. A system displaying a single scattering mechanism should have all plots with a single slope. Yet in the GdSb films, we see that at high fields $MR \propto (\mu_0 H/\rho_0)^{1.58}$ for the 10 nm thick film and $MR \propto (\mu_0 H/\rho_0)^{1.96}$ for the 4 nm thick film. Given the same electron carrier density, the main difference in the exponent likely stems from a combination

of (i) a closer to exact carrier compensation at thicker films and (ii) interface scattering mechanisms in the 4 nm thick film, which end up reducing the mobilities and altering the carrier mobility ratios. Both effects lead to a larger negative Hall coefficient observed for thinner films (Figure 3.10(c)). In LuSb films, it was shown that the hole pocket size shrinks as the film thickness decreases [57], thus, a change in carrier ratios is possible upon confinement.

From the minimal mobilities and carrier densities of both charge carriers, we calculate a minimum elastic scattering length of l_e~270 nm. Thus for all film thicknesses studied in this paper, we are in the quantum regime where the electron wave function is coherent on length scales of the thickness of the film (i.e., d <l_e) [28]. The thinner 4 nm films also show at low temperatures a resistivity cusp at low fields (Figure 3.10(b), inset), a signature of the weak antilocalization effect reflecting the strong spin-orbit coupling in GdSb. These magnetotransport signatures for thin films were present in other epitaxial RE-V and high spin-orbit coupled semimetal films of similar thickness [10,27]. In addition to weak antilocalization and potential electron-electron interactions in thin films, magnetic field-induced transitions at low temperatures are also present: a spin-flop transition is seen at 0.2T in Figure 3.10(b), inset as well as an intermediate metamagnetic phase that is stable between 0.2T and 0.5T. Changes in resistance due to weak magnetic impurity states [142] are ruled out based on the temperature dependence of the spin-flop field. Weak localization and electron-electron interaction effects are also excluded by observing similar behavior in 20 nm thick films. Jumps and kinks seen in the magnetoresistance curve at low fields near the spin-flop transition are similar to earlier observations of metamagnetic transitions in other RE-Vs, such as HoBi [29] and ErAs [163].

3.5.3 DFT calculations

The calculated band structure of unstrained GdSb, courtesy of Dai Q. Ho and Anderson Janotti at the University of Delaware, is presented in Figure 3.5, Figure 3.7 and Table 3.2 andTable 3.4. Kohn-Sham orbitals in DFT [177,178] were expanded using a plane-wave basis set with a 400 eV energy cutoff. Interactions between ion cores and valence electrons were described by the projector augmented wave (PAW) method [179]. For the magnetic phase calculations, we used a rhombohedral unit cell consisting of 4 atoms and the primitive cell of an FCC crystal structure with 2 atoms to simulate the AFM and FM states, respectively. An $8 \times 8 \times 8$ Γ-centered k-point mesh was used for integration over the first Brillouin zone. The band structure was unfolded for the AFM calculation to directly compare with ARPES data [180,181]. The configurations of the valence shells of Gd and Sb are $4f^7 5s^2 5p^6 5d^2 6s^1$ and $5s^2 5p^3$, respectively. Spin-orbit coupling was included self-consistently in all calculations. The calculated Fermi wavevectors, band extrema, and carrier densities for the AFM, FM, and non-magnetic phases are reported in Table 3.2. In Table 3.4, we present the calculated carrier ratio and its dependence on the relative position of the Fermi level. The charge carrier concentrations were determined using the SKEAF code [182], which uses the Fermi volume obtained from the Wannier90 program with the Brillouin zone sampling consisting of 1,000,000 k-points [183]. The carrier densities from the non-magnetic phase were used to estimate the carrier concentrations and degree of compensation in the AFM phase due to the similar Fermi wavevectors obtained (Table 3.2) and the difficulty in calculating the AFM carrier density directly from the DFT density of states.

3.6 Conclusions

In summary, we have grown epitaxial GdSb films by MBE and studied their band structure and magnetic properties with ARPES, DFT, and magnetotransport. The growth window of high-quality single-crystal GdSb films on a lattice-matched III-V structure has been established, resulting in high magnetoresistance values for the given film thicknesses among RE-V. Our comprehensive study of GdSb films paves the way to understand the relationship between the electronic and transport properties of RE-V films vs. their bulk crystals and other films in semimetallic systems with similar chemistry, such as the Heusler compounds: GdXV (X=Pt, Pd; V=Sb, Bi).

We have identified magnetic and interface scattering mechanisms in GdSb, limiting the mobilities of thin RE-V films and ultimately resulting in lower magnetoresistance values than bulk single crystals and reduced magnetoresistance in thinner films. ARPES experiments of the GdSb layer showed quantization effects of energy levels in the electron- and hole pockets. We did not detect these features in magnetotransport quantum oscillations due to the higher surface scattering and larger effective mass of the higher-energy quantum-well subband levels. Tuning the quantum-well level subband energy position by varying the film thickness could serve as a potential route for engineering carrier compensation and mobilities for improved magnetoresistive behavior.

While we do not see evidence of a *p-d* band inversion in ARPES measurements performed for the antiferromagnetic state, our DFT calculations show the near onset of band overlap for strong exchange splitting at low temperatures and high magnetic fields in the forced ferromagnetic phase. DFT calculations treating the *4f* electrons as core levels in a nonmagnetic phase describe well the band structure of GdSb below the Néel temperature. By introducing *4f*

electron AFM ordering into the valence band structure in our DFT calculations, we have obtained a more accurate description of the split-off band position and total carrier density of the electron and hole bands.

4 Tuning the band topology of GdSb by epitaxial strain

4.1 Introduction

Strain engineering of low-dimensional topological quantum materials serves as a powerful approach to manipulating electronic band structures, thereby controlling topological phase transitions and transport behavior [29]. For example, strained HgTe quantum wells grown in the tensile and compressive regimes were shown to transition from a semimetallic to a two-dimensional topological insulator (TI) system, respectively [30]. Despite the promise of topological state tuning, strain studies of quantum materials thin films are typically restricted either to local, defect-induced strain gradients [31–33] or to strain levels below 1% strain [34,35] in the case of uniform strain in lattice-mismatched growths. In TIs such as the group V-chalcogenides (X_2Z_3, X=Bi, Sb; Z=Te, Se), unstrained growths occur even on substrates with high lattice mismatch due to the low bonding energies between van der Waals layers [28,36]. In addition to the challenge of stabilizing highly strained pseudomorphic topological materials, visualizing the band structure modifications as a function of strain/pressure has been difficult in both bulk single crystals and thin films. In single crystals, large pressure cells are difficult to implement, and when using mechanical strain tuning apparatus, special care is needed to ensure the application of uniform strain [37–40]. For thin films, there are limited reports combining strained film growth with direct spectroscopic tools, such as angle-resolved photoemission spectroscopy (ARPES), with a few exceptions in oxide films [41,42].

Recent reports of bulk rare-earth monopnictide (RE-V) crystals under hydrostatic pressure reveal the emergence of a superconducting phase transition in nonmagnetic RE-Vs [184–186],

and theoretical predictions suggest potential strain and pressure-induced transitions in band topology [60,146,149,187,188]. In addition to observing a strain-driven topological phase transition in the RE-V system, strain studies of RE-Vs are highly relevant for spintronic-based applications as another control knob that can be used to tune magnetoresistance and magnetic properties in RE-V thin films. Finally, coupled with III-V compounds, RE-V thin films and particles have shown many potential device applications [45], including buried metallic contacts [43], THz emitters and detectors [189,190], thermoelectrics [191,192], plasmonic heterostructures [153], and diffusion barriers [151]. Therefore, straining RE-V thin films presents another avenue to tune the functional properties of these semimetals, specifically by modifying magnetic exchange interactions and the charge carrier ratio in these otherwise electron-hole-compensated semimetal systems.

Here, we use ARPES to study the evolution of the electronic structure of GdSb thin films grown by molecular beam epitaxy (MBE) subjected to 2% tensile (+2%) and 2% compressive (-2%) biaxial strain. GdSb belongs to the RE-V family of compounds and is particularly interesting due to the relatively small electron-hole band energy gap that can be inverted via attainable strain/hydrostatic pressure, resulting in a nontrivial $\mathbb{Z}_2$ topological invariant classification [60]. We demonstrate the ability to tune the bandgap and Néel temperature (T_N) in strained GdSb thin films and thereby control the topological phase transition from a trivial to a nontrivial state. GdSb thin films also present high magnetoresistance [154], have a type-II antiferromagnetic ordering at nearly the highest temperature of all RE-V (T_N = 24 K) [141], and can be epitaxially integrated with III-V compounds [44], see Figure 4.1(a-c). This approach to band engineering via epitaxial strain can broadly be applied to a wide range of RE-V antiferromagnet semimetals.

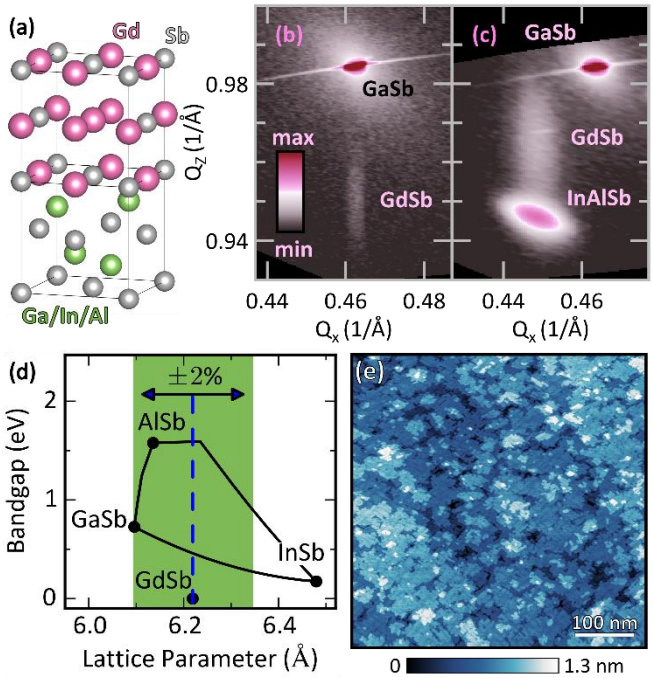

Figure 4.1. (**a**) Crystal structure and epitaxial relationship of the rocksalt GdSb / zincblende III-V (001) orientation. RSM of the (226) reflection in (**b**) −2% and (**c**) +2% strained GdSb films, demonstrating coherent growth to the underlying III-V layer. (**d**) Biaxial strain window of GdSb and range of III-V bandgaps and lattice parameters used for buffer layer growth. (**e**) STM image of the −2% strained film: 4 nm GdSb / GaSb (001) (V = −0.5 V, I=1 nA). Figure reprinted with permission from [193].

4.2 MBE growth, ARPES measurements, and DFT calculations

GdSb has a lattice parameter of a = 6.219 Å between InSb (6.479 Å) and GaSb (6.096 Å)/AlSb (6.136 Å), allowing high tensile and compressive biaxial strain by varying the underlying semiconducting III-V buffer layer structure as shown in Figure 4.1(d). MBE was used to grow epitaxial GdSb (001) thin films on $In_xGa_{1-x}Sb/In_xAl_{1-x}Sb$ buffer layers nucleated on a GaSb (001) substrate. For photoemission and scanning tunneling microscopy (STM) studies, p-type doped substrates and p-type $In_xGa_{1-x}Sb$ buffer layers were used. By changing the Al/In concentration in the buffer layer, the in-plane lattice parameter was adjusted before GdSb growth, as shown in Figure 4.1(d). For magnetotransport measurements, undoped $In_xAl_{1-x}Sb$ buffer layers and epi-ready semi-insulating GaSb (001) wafers were used. Further details on the GdSb growth window, ARPES measurement conditions, and electronic

characterization of lattice-matched unstrained films are detailed in our previous report [154]. The growth of strained films was studied *in situ* with reflection high-energy electron diffraction, STM, and confirmed *ex situ* with x-ray diffraction reciprocal space map (RSM) measurements. Grazing incidence RSM of the (226) reflections for 4-nm-thick GdSb films is shown in Figure 4.1(b-c), confirming that the layers remain pseudomorphically strained. *In situ* STM scans of the 2% compressive strained GdSb film grown directly on GaSb in Figure 4.1(e) and other GdSb films on ternary III-V buffers [154] confirm the growth of a smooth and continuous GdSb film with terrace step heights consistent with half of a unit cell (one atomic monolayer).

To reduce thin-film contributions to the electronic band structure, such as substrate charge transfer and quantum confinement [57], highly strained films as thick as possible (i.e., near the critical relaxation thickness) are studied. In GdSb, strong film-substrate interactions and interlayer bonding allow pseudomorphic growth at high strain levels. The critical thickness (h_c) is determined empirically as the onset of partial relaxation observed with reciprocal space mapping, with $h_c = 5.5\,nm$ in 2% compressively strained films. Consequently, all strained growths are limited to a thickness of 4 nm. From the RSM-extracted in-plane and out-of-plane GdSb lattice parameters, we calculated the planar ($\varepsilon_{\parallel}$) and vertical ($\varepsilon_{\perp}$) strains and Poisson's ratio: $\frac{\varepsilon_{\perp}}{\varepsilon_{\parallel}} = \frac{-2\nu}{1-\nu}$ [194] such that $\nu_{exp} = 0.12 \pm 0.03$. The experimental Poisson's ratio agrees with our DFT-calculated value $\nu_{DFT} = 0.10$ and is comparable to earlier predictions made for other RE-V compounds [195,196].

ARPES measurements at the Advanced Light Source (ALS) at beamline 10.0.1.2 were conducted at 11 K and at the Stanford Synchrotron Radiation Lightsource (SSRL) at beamline 5-2 at 20 K. Both were acquired with a Scienta DA30L hemispherical analyzer. ALS

measurements were conducted for *in vacuo* transferred samples, where a custom-built vacuum suitcase with a base pressure $<10^{-10}$ Torr was used to transfer films from the growth chamber at UC, Santa Barbara, to beamline 10.0.1.2 at the ALS in Berkeley. The SSRL measurements at beamline 5−2 were performed for *ex situ* transferred films. To prevent oxidation of the GdSb films during the *ex situ* transfer to SSRL, a thick ~800 nm antimony capping layer was deposited with Sb_2 flux after GdSb growth during sample cool down beginning at a temperature of 230-130 ^{o}C. Before measurement, samples were heated to 420 ± 20 ^{o}C (calibrated by pyrometry) in an ultra-high vacuum chamber and held at that temperature for ~30 min to fully desorb the Sb cap. The potential thermal decomposition of the $In_xGa_{1-x}Sb$ buffer film limits the maximum annealing temperature. During the final stage of Sb desorption, a spike in pressure to 1×10^{-8} Torr was observed, and the film surface visually transitioned from a shiny to a hazy-matt finish and back to a polished appearance. The thermal desorption window of the Sb cap was confirmed by scanning tunneling microscopy at UCSB and at the SSRL beamline by examination of the Sb 4*d* and Gd *f* core levels. All films showed no evidence of oxidation in XPS scans: a single binding energy component in the Gd 4*f* level was seen, and no oxygen 2s core levels were present. An Sb-related surface state was observed for all films and was remarkably stable for the compressive film, see sharp linear dispersions crossing the Fermi level at $k_F \sim 0.9$ Å^{-1} in Figure 4.2(b,d,f). The Fermi surface of the surface state differs from the expected electronic band structure of elemental Sb and might have originated from a stabilized square-net Sb-rich surface reconstruction [197].

Dai Q. Ho and Anderson Janotti at the University of Delaware investigated the electronic structure of GdSb theoretically using density functional theory (DFT) and the screened hybrid functional of Heyd, Scuseria, and Ernzerhof (HSE06) [198,199] with 25% of exact exchange

and accounting for spin-orbit coupling, as implemented in the Vienna *ab initio* simulation package (VASP) code [200,201]. The Gd *4f* electrons were treated as valence electrons for antiferromagnet (AFM) calculations in Figure 4.2(g-h), whereas for the nonmagnetic phase calculation in the slab calculations the *4f* electrons were treated as core electrons. The configurations of the valence shells of Gd and Sb are $4f^7 5s^2 5p^6 5d^2 6s^1$ and $5s^2 5p^3$, respectively. The calculated equilibrium lattice parameter of 6.197 Å for GdSb was used to consistently determine the Poisson ratio. The experimental lattice parameter of GdSb at room-temperature is reported to be between 6.210 Å [202] and 6.219 Å [142]. For the 2% compressive (tensile) GdSb calculations we used an in-plane lattice parameter of 6.073 Å (6.321 Å), obtaining an out-of-plane lattice parameter of 6.222 Å (6.171 Å).

Kohn-Sham orbitals in DFT [177,178] were expanded using a plane-wave basis set with the value of energy cutoff of 400 eV. Interactions between ion cores and valence electrons were described by the projector augmented wave (PAW) method [179]. We used a rhombohedral unit cell consisting of 4 atoms for magnetic phase calculations to simulate the AFM state in GdSb. The local magnetic moment on each Gd site was constrained to point along $[11\bar{2}]$ direction. An $8 \times 8 \times 8$ Γ-centered k-point mesh was used for integration over the first Brillouin zone. The folded band structure of the AFM unit cell was then unfolded back to the FCC primitive unit cell to facilitate a direct comparison with ARPES data [180,181].

The Fermi surface and Fermi volume were obtained by Wannier interpolation from first principles using the nonmagnetic phase. Since the Gd *d* and Sb *p* are relevant orbitals around the Fermi level, they were used as the starting projectors for the Wannier orbitals construction. The charge carrier concentrations were then estimated from the obtained Fermi volumes by using the SKEAF code [182]. Hopping term values used in constructing the TB model were

extracted from the Wannier orbitals-based Hamiltonian, which is directly achieved from the wannierization process.

We have further investigated the consequence of the size quantization effect on the 4 nm thin films by performing calculations for 4-nm-thick freestanding slabs. Unstrained and in-plane strained cases were simulated using a supercell consisting of 13 monolayers (ML, 2 ML in one unit cell) thick slabs along the [001] direction, assuming a nonmagnetic phase. A vacuum space of at least 20 Å was included in the [001] direction of the supercell to remove artificial interaction between images of the slabs.

4.3 Band topology evolution of strained GdSb

The Fermi surface of GdSb is composed of two hole pockets (β,δ) at the Brillouin zone center (Γ), a third spin-orbit split-off band (γ) positioned below the Fermi level, and three ellipsoidal electron pockets (α) at the Brillouin zone edge (X_1, X_2, X_3, the X_3 high-symmetry point transforming to the Z point in the tetragonal *I4/mmm* space group under biaxial strain). Figure 4.2(a-d) highlights the ARPES high-symmetry cuts studied for the electron pockets located at $X_{1,2}$ points in the film plane. Due to the high k_z broadening expected for the vacuum ultraviolet light used in the ARPES measurements [148], the scans of the electron pocket in Figure 4.2(d) present both the minor axis cut of the ellipsoidal electron pocket and project the electron pocket from the neighboring Brillouin zone in Figure 4.2(b). Figure 4.2(e-f) shows the electron pocket at the Z high-symmetry point, positioned along the film plane normal. Figure 4.3 depicts the expanded momentum range of the *E-k* cuts in Figure 4.2(e-f), capturing electron and hole pockets lying perpendicular to the film plane (Z high-symmetry point for $k_{||} = 0$) and in the film plane ($X_{1,2}$ high-symmetry points in the neighboring Brillouin zones

projecting to $\bar{M}$ at $k_{||} = \frac{2\pi}{a}$). Figure 4.4 displays the valence band pockets in the k_z= Γ plane dispersing along $\bar{M} - \bar{\Gamma} - \bar{M}$. We first review the band topology evolution under strain, and at a later stage address the effect of finite thickness quantization on the additional subbands observed in ARPES and modeled with DFT.

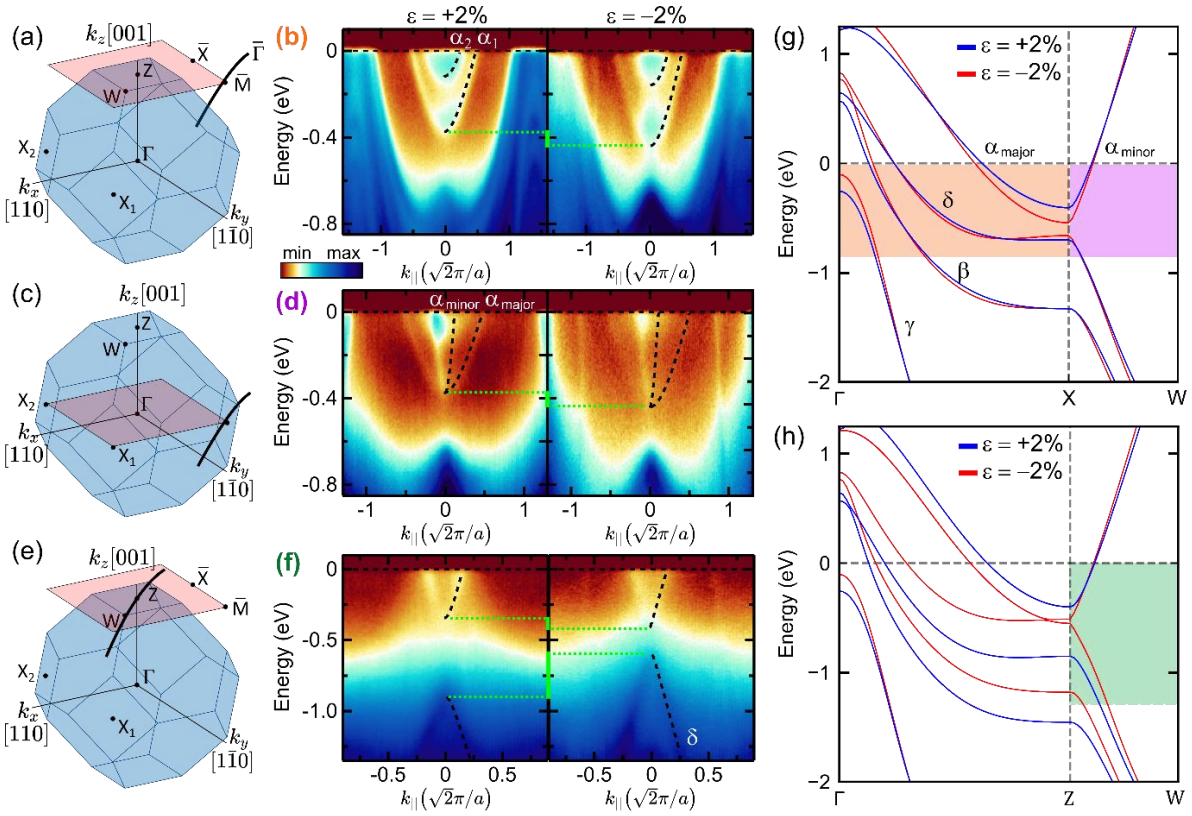

Figure 4.2. Band dispersion of electron pockets and hole bands in GdSb films studied with ARPES and strain-induced modifications for +2% tensile (left) and −2% compressive (right) biaxial strain. (**a**), (**c**), and (**e**) Schematics of the bulk Brillouin zone projected to the (001) surface Brillouin zone, showing the measured k_z plane (pink square) and *E-k* spectra directions (black line). $\bar{\Gamma} - \bar{M} - \bar{\Gamma}$ cut along the in-plane electron pockets $X_{1,2}$ for the (**a,b**) semimajor axis ($\Gamma - X_1 - \Gamma$) measured at k_z=Z with a photon energy of 94 eV, and (**c,d**) semiminor axis ($W - X_2 - W$) measured at k_z= Γ with a photon energy of 60 eV. (**e,f**) $\bar{M} - \bar{\Gamma} - \bar{M}$ cuts of the out-of-plane electron pocket semiminor axis ($W - Z - W$) measured at k_z=Z with a photon energy of 88 eV. Black dotted lines are hyperbolic fits to the band dispersions, and the green dotted lines highlight the band shifts. See Table 4.1 for the Fermi wave vectors and band extrema extracted from the fits. (**g-h**) DFT-calculated band structures for ε = +2, −2% along (**g**) the in-plane high-symmetry points and (**h**) film plane normal direction. Fermi levels were set at 0. Shaded regions in (**g-h**) highlight the *E-k* cuts in panels (**b,d,f**).Figure reprinted with permission from [193].

ARPES of the electron pockets at $X_{1,2}$ (Figure 4.2(a-d)) shows an increased bandwidth and major axis Fermi wave vector upon compressive strain, with the band minima shifting from

$\alpha_{X_{1,2}}^{+2\%} = -0.375$ eV to $\alpha_{X_{1,2}}^{-2\%} = -0.440$ eV. The hole band extrema in the film plane remain largely unchanged: $\delta_{X_{1,2}}^{+2\%} = -0.66$ eV, $\beta_{X_{1,2}}^{+2\%} = -1.41$ eV, and $\delta_{X_{1,2}}^{-2\%} = -0.68$ eV, $\beta_{X_{1,2}}^{-2\%} = -1.45$ eV (see Figure 4.4 and Table 4.1). Fitting the electron and hole bands maximum at Z along $W - Z - W$ in (Figure 4.2(f) and Figure 4.3), we see a downward shift in the electron pocket from $\alpha_Z^{+2\%} = -0.34$ eV to $\alpha_Z^{-2\%} = -0.41$ eV , and for the valence band pockets we notice an upward shift: $\delta_Z^{+2\%} = -0.9$ eV to $\delta_Z^{-2\%} = -0.59$ eV for the heavy-hole band, and $\beta_Z^{+2\%} = -1.45$ eV to $\beta_Z^{-2\%} = -1.31$ eV for the light-hole band. The influence of epitaxial strain on the hole bands, primarily lying along $\Gamma - Z$ (and only small shifts for the bands dispersing in-plane), agrees with our calculations in Figure 4.2(g-h) and earlier DFT calculations performed for LaSb [150]. Due to high k_z broadening, in Figure 4.2(e-f) and Figure 4.3, the valence band pockets at $k_z=\Gamma$ also project to the $k_z=Z$ plane, leading to a blurred background intensity preventing the observation of the expected topological surface states (TSS) for the compressively strained film (TSS in RE-Vs typically have a weaker spectral intensity compared to the bulk bands [147,166], and leading to a larger error bar in our estimation of electron band minima at Z. Further work using bulk-sensitive soft x-ray ARPES would enable better ability to resolve the bulk band dispersion along $\Gamma - Z$. Nevertheless, the ARPES dispersions for the hole bands at X and Z and the electron bands lying in the film plane are consistent with our DFT calculations and support the predicted bandgap reduction scenario at Z moving from tensile to compressive strain.

Our DFT calculations in Figure 4.2(g-h) show that at $\varepsilon = -2\%$ GdSb transitions into a topological semimetal state as the hole and electron bands anti-cross along $\Gamma - Z$ and are inverted at Z. In contrast, the in-plane electron and hole bands at $X_{1,2}$ remain gapped. The ARPES dispersions for bands lying in the film plane are consistent with our DFT calculations

and support the predicted bandgap reduction scenario. The DFT-calculated and ARPES-extracted Fermi wave vectors and band extrema positions for both strain values are summarized in Table 4.1, and the calculated gap at *Z*, $E_g(Z)$, between the conduction and valence bands as a function of strain level is shown in Figure 4.5(c). Compressive strain widens the bandwidth along $X/Z - W$ for the hole and electron pockets (see Table 4.1 and Figure 4.2(g-h)).

Table 4.1. Fermi surface of 4 nm-thick strained GdSb (001) films. Band maximum/minimum energy positions, Fermi wave vectors (k_F) for all bands, and the carrier density ratio, obtained from ARPES measurements and DFT calculations. Band extrema are reported for all quantum-well subbands observed via ARPES.

			+2% (tensile strain)		**−2% (compressive strain)**	
			ARPES	DFT	ARPES	DFT
α k_F (Å^{-1})	Minor $W - X$	$X_{1,2}$	0.085 (±0.02)	0.103	0.084 (±0.02)	0.110
		Z	0.11 (±0.05)	0.108	0.089 (±0.02)	0.103
	Major $\Gamma - X$	$X_{1,2}$	0.356 (±0.02)	0.374	0.371 (±0.03)	0.423
		Z	NA	0.364	NA	0.434
α Band Extrema (eV)		$X_{1,2}$	α_1: −0.375 (±0.004) α_2: −0.118 (±0.006)	−0.405	α_1: −0.440 (±0.004) α_2: −0.157 (±0.004)	−0.540
		Z	-0.34 (±0.02)	−0.398	−0.41 (±0.02)	−0.512
δ k_F (Å^{-1})	$\bar{M} - \bar{\Gamma} - \bar{M}$		0.230 (±0.030)	0.238	0.184 (±0.030)	0.248
	$\bar{X} - \bar{\Gamma} - \bar{X}$		0.123 (±0.01)	0.175	0.124 (±0.018)	0.189
β k_F (Å^{-1})	$\bar{M} - \bar{\Gamma} - \bar{M}$		0.116 (±0.017)	0.127	0.105 (±0.005)	0.151
	$\bar{X} - \bar{\Gamma} - \bar{X}$		0.064 (±0.008)	0.127	0.077 (±0.010)	0.151
γ Band Extrema (eV)		Γ	−0.32 (±0.01)	−0.255	−0.30 (±0.01)	−0.102
		$X_{1,2}$	−3.205 (±0.05)	−3.33	−3.12 (±0.05)	−3.27
δ Band Extrema (eV)		$X_{1,2}$	δ_1: −0.66 (±0.02) δ_2: −0.82 (±0.02) δ_3: −1.09 (±0.02)	-0.70	δ_1: −0.68 (±0.02) δ_2: −0.88 (±0.05) δ_3: −1.21 (±0.02)	−0.66
		Z	δ_1: −0.90 (±0.02)	−0.855	δ_1: −0.59 (±0.08)	−0.55
β Band Extrema (eV)		$X_{1,2}$	β_1: −1.41 (±0.01) β_2: −1.62 (±0.03)	−1.33	β_1: −1.45 (±0.03) β_2: −1.70 (±0.05)	−1.33
		Z	β_1: −1.45 (±0.02)	−1.45	β_1: −1.28 (±0.02)	−1.18
Eg		$X_{1,2}$	0.285 (±0.02)	0.295	0.24 (±0.02)	0.12
		Z	0.56 (±0.03)	0.457	0.18 (±0.08)	-0.04
n_e/n_h			1.52	1.09	1.85	1.11

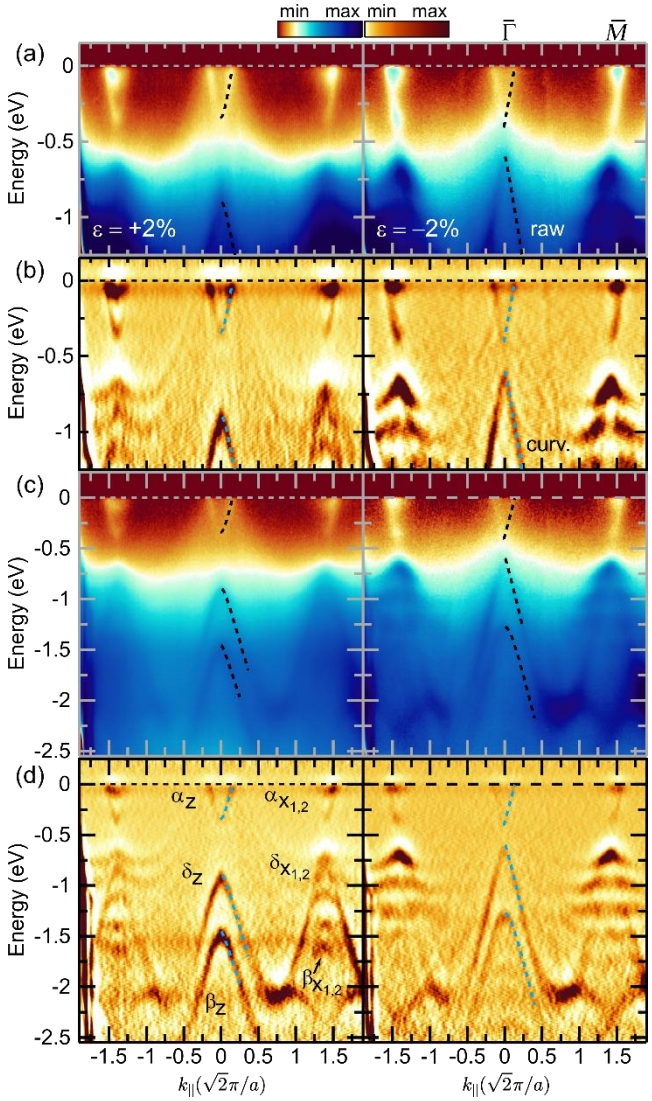

Figure 4.3. *E-k* dispersion along $\bar{M} - \bar{\Gamma} - \bar{M}$ in the biaxial strained GdSb films measured a photon energy of 88 eV, capturing a wider energy and momentum range of the cuts shown in Figure 4.2(e-f). (**a,c**) Raw data, (**b,d**) curvature plots of the raw data. (**a,b**) Narrow energy range near the Fermi level (**c,d**) wider energy range showing the *β* hole pocket maximum. Fermi wave vectors and band extrema extracted from the fits are detailed in Table 4.1. Figure reprinted with permission from [193].

Table 4.1 summarizes the experimental and calculated bandgaps at *X* and *Z* for each strain level, $Eg_{X/Z} = \alpha_{X/Z} - \delta_{X/Z}$ and shows qualitative agreement. The reduced bandgap when transitioning from tensile to compressive strain suggests two possible scenarios for $\varepsilon = -2\%$: inverted bands with a nontrivial topology or uninverted bands with a smaller trivial gap. The gap measured for the compressive strained film is closer to that of unstrained GdSb films [154] (with a 20 nm thickness) $Eg_X^{0\%} = Eg_Z^{0\%} = \alpha_X^{0\%} - \delta_X^{0\%} = 0.21$ eV. Compared to the thicker

unstrained film, quantum confinement effects in the thinner 4 nm thick strained films are expected to be stronger in the in-plane electron pockets (*X*) and negligible in the out-of-plane pocket (*Z*) [203] as demonstrated in our DFT calculation in Figure 4.7. Therefore, the close values of $Eg_Z^{0\%}, Eg_Z^{-2\%}$ suggest that a transition past the critical bandgap closing point is possible under compressive strain. In order to unequivocally determine a nontrivial band topology in compressive strained GdSb, future work should examine additional strain levels between 0 and -2% biaxial strain to track the gap closing, as well as apply strain beyond $\varepsilon = -2\%$ to access a larger inverted gap. We expect that by further optimizing growth conditions higher compressive strain should also be possible, for example by growing directly on InAs, $\varepsilon = -2.5\%$.

We have further checked the predicted topological nature of the strained GdSb by evaluating the $\mathbb{Z}_2$ strong topological index ν_0 according to the band parity product criteria [4] considered at eight time-reversal inversion momenta (TRIM) points: *Γ*, 4 *L*, 2 *X*, and *Z* where $(-1)^{\nu_0} = \prod_{i=1}^{8} \delta_i$, with δ_i being the parity product at each TRIM point for all occupied bands. Time-reversal symmetry (Θ) and primitive-lattice translation symmetry ($T_{1/2}$) in GdSb are broken; however, their combination is preserved (S=$\Theta T_{1/2}$), enabling the classification of the topological nature using the $\mathbb{Z}_2$ topological invariant [204]. In the unstrained and tensile cases, the $\mathbb{Z}_2$ invariant $\nu_0 = 0$, demonstrating a trivial topological state. In contrast, we observe a change in the parity product at the *Z* point (from $+$ to $-$) in the compressively strained case, resulting in a $\mathbb{Z}_2$ index $\nu_0 = 1$ which indicates a nontrivial topological band structure. We have found that there are only minor changes in our DFT calculation between the room-temperature lattice parameter (6.219 Å) and low-temperature/DFT relaxed GdSb lattice parameter (6.197 Å), with band extrema changes smaller than 50 meV. We used the calculated equilibrium

lattice parameter of 6.197 Å for unstrained GdSb to consistently determine the Poisson ratio. However, since the calculated inverted gap for the 2% compressive layer is 40 meV, it can be sensitive to the starting relaxed lattice parameter used. In our earlier work, we showed that HSE06 AFM calculations for unstrained GdSb accurately describe the electronic bandgap at the bulk *X* point compared to other DFT functionals [154]. Thus, the 2% compressive GdSb appears to lie within the transition region between a strong topological insulator with a nonzero value of the topological invariant and a $\mathbb{Z}_2$ trivial topological state.

Table 4.1 lists also band positions collected via ARPES and results from DFT calculations. The values of hole and electron carrier Fermi wave vectors for both GdSb strain levels are similar to other bulk crystal RE-V compounds studied with ARPES [55,147,148,156–158]. Comparison to other RE-Vs also demonstrates that for the in-plane dispersions, biaxial lattice compression shows a similar trend as chemical pressure induced by lanthanide contraction; a smaller lattice parameter leads to a higher chemical potential [60,158]. The experimental Fermi velocity of both the hole and electron carriers does not show a significant change as a function of strain, which can be explained by the relatively high energy separation of the Fermi level from the band extrema, where most effective mass changes are expected to take place [205].

The hole band Fermi wave vectors and γ band extrema near the valence band in Table 4.1 (extracted from Figure 4.2(f), Figure 4.3, and Figure 4.4) deviate from our DFT calculations, which predicted a displacement of the valence band maximum with strain (Figure 4.2(g-h) and Table 4.1), a trend we do not observe experimentally. In Figure 4.4, the hole split-off γ band maximum at Γ does not shift significantly with strain and remains at the same maximum energy of −0.3 eV. In addition, when transitioning from tensile to compressive strain we observe a

decrease in k_F along $\bar{M} - \bar{\Gamma} - \bar{M}$ in contrast to DFT predictions. These two trends suggest that the observed position of the Fermi level in the compressive film could differ from the initial DFT-calculated position shown in Figure 4.2(g-h). The origin of this variation between ARPES results and DFT calculations could be either due to quantum size effects in the hole band [57], related to the hydrostatic tensor contributions to the DFT-modeled valence band shift [206], or resulting from experimental effects such as defects in the compressively strained film leading to bulk doping or potential Fermi level pinning at the film surface.

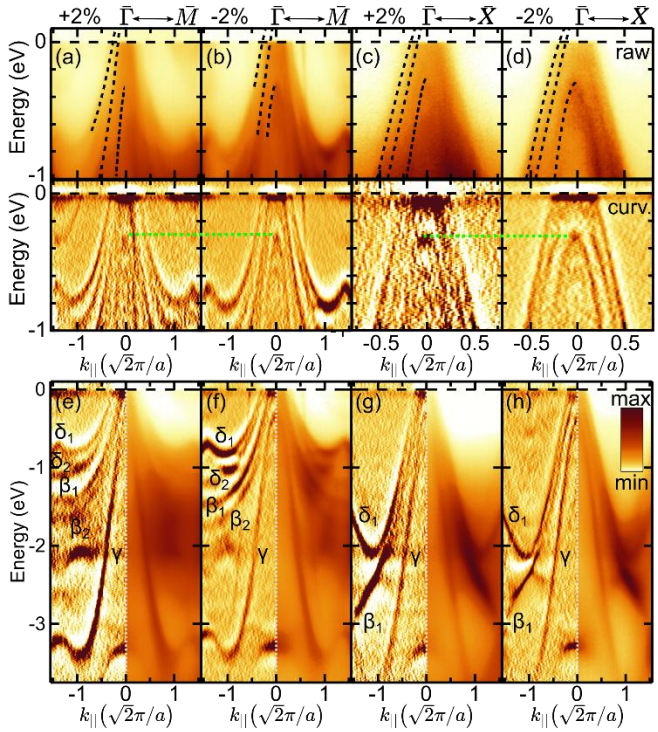

Figure 4.4. *E-k* dispersion of the hole pockets in the biaxial strained GdSb films measured at $k_z = \Gamma$ (photon energy of 60 eV). ARPES spectra near the Fermi level, the green dotted line highlights the same γ valence band maximum position, and black lines show overlaid fits along (**a,b**) $\bar{M} - \bar{\Gamma} - \bar{M}$ and (**c,d**) $\bar{X} - \bar{\Gamma} - \bar{X}$. Top panel: raw data, bottom panel: curvature plot of the raw data. (**e-h**) Wider energy range of the same cuts in (a-d), showing the quantum well states. The plots on the right-hand side present the raw data, and the plots on left-hand side display the curvature plot. Fermi wave vectors extracted from the fits to the valence band and band extrema in panels (**e-h**) are detailed in Table 4.1. Figure reprinted with permission from [193].

4.4 Tight binding model

The bands lying in the normal direction of the film plane, i.e. along [001] ($\Gamma - Z$), are primarily affected by epitaxial strain, whereas in RE-Vs under hydrostatic pressure [60,149] all three $\Gamma - X$ high-symmetry directions are equivalent. The bandgap changes in $\Gamma - Z$ can be explained using a simple tight-binding (TB) model, accounting for the orbital composition of the electron and hole bands near the Fermi level and the scaling of nearest-neighbor and next-nearest neighbor interactions with strain (see Figure 4.5(b-c)). Our orbital composition determination in Figure 4.5(a) shows the *p*- and *d*- orbital composition of the valence and conduction band, respectively, and agrees with ARPES measurements by Nummy et al. [147] assigning the orbital characters in the analogous La-Vs. In addition, we do not observe significant mixing between *s* orbitals and the group of *p* and *d* orbitals near the Fermi level.

Based on the orbital-resolved DFT electronic band structure in Figure 4.5(a), a TB model was constructed that reproduces well the DFT-calculated band structure and the effect of strain on hopping terms (Table 4.2). The TB Hamiltonian is thus constructed by 16x16 matrix elements, consisting of 8 atomic orbitals (Sb: p_x, p_y, p_z; and Gd: d_{yz}, d_{zx}, d_{xy}, d_{x2-y2}, d_{z2}) and accounting for spin-orbit coupling (SOC) which contains the atomic SOC parameter λ_{Gd} and λ_{Sb}. These parameters are matched to the Gd *5d* and Sb *5p* atomic values, which are λ_{Gd} =0.43 eV and λ_{Sb}=0.53 eV [207]. On-site energies are derived from the unstrained GdSb calculation: Sb_p=4.190 eV, $Gd_d(e_g)$=9.283 eV, and $Gd_d(t_{2g})$=7.562 eV. Taking the two-center approximation and considering only the nearest-neighbor Gd-Sb interactions and the next nearest-neighbor Gd-Gd and Sb-Sb interatomic couplings, the hopping terms are expressed by [208]:

$$t(p_x,p_y)_{[110]}=1/2\ (p_{Sb}p_{Sb}\sigma - p_{Sb}p_{Sb}\pi)$$

$$t(p_x,p_x)_{[110]}=1/2\ (p_{Sb}p_{Sb}\sigma + p_{Sb}p_{Sb}\pi)$$
$$t(p_{x/y},d_{xy})_{[100]/[010]} = p_{Sb}d_{Gd}\pi$$
$$t(d_{xy},d_{xy})_{[110]}=1/4(3d_{Gd}d_{Gd}\sigma + d_{Gd}d_{Gd}\delta)$$
$$t(d_{xy},d_{xy})_{[011]}=1/2(d_{Gd}d_{Gd}\pi + d_{Gd}d_{Gd}\delta)$$
$$t(d_{xy},d_{yz})_{[101]}=1/2(d_{Gd}d_{Gd}\pi - d_{Gd}d_{Gd}\delta)$$
$$t(p_{x/y},d_{x\hat{}2-y\hat{}2})_{[100]/[010]} = \frac{\sqrt{3}}{2}p_{Sb}d_{Gd}\sigma$$

The obtained TB parameters in the standard Slater-Koster notation are tabulated in Table 4.2. The Fermi level was set to 5.6 eV so that the DFT and TB dispersions match in position for unstrained GdSb.

Using the parameters listed in Table 4.2, the TB model is constructed using the open-source package chinook [209]. The energy dispersion obtained from the TB model in Figure 4.5(d) and Figure 4.6 reproduces well the ARPES and DFT results. Being isotropic, the TB model accounts for the strain-induced changes in hopping terms by using Slater-Koster parameters derived primarily from hopping terms in the (001) plane (except $t(d_{xy},d_{xy})_{[011]}$ and $t(d_{xy},d_{yz})_{[101]}$ in order to extract $d_{Gd}d_{Gd}\pi$ and $d_{Gd}d_{Gd}\delta$). The hopping term decay rate, $V^* - V_0$, is calculated based on the absolute difference between the strained (V^*) and unstrained (V_0) hopping terms. For example, $V(p_{Sb}p_{Sb}\pi)^{+2\%} - V(p_{Sb}p_{Sb}\pi)^{0\%} = -0.064 - (-0.090) = 0.026$.

Table 4.2. Nearest- and next-nearest neighbors TB parameters for GdSb, extracted from DFT calculations.

Parameters (eV)/Strain	−2%	0%	+2%
$p_{Sb}p_{Sb}\sigma$	0.713	0.661	0.583
$p_{Sb}p_{Sb}\pi$	-0.095	-0.090	-0.064
$d_{Gd}d_{Gd}\sigma$	-0.814	-0.745	-0.695
$d_{Gd}d_{Gd}\pi$	0.233	0.239	0.238
$d_{Gd}d_{Gd}\delta$	0.051	0.046	0.056
$p_{Sb}d_{Gd}\pi$	-0.964	-0.894	-0.845
$p_{Sb}d_{Gd}\sigma$	-1.899	-1.745	-1.665
λ_{Gd}		0.43	
λ_{Sb}		0.53	

The band structure of GdSb resulting from our TB parametrization is presented in Figure 4.5(d) and Figure 4.6 over narrow and wide energy ranges, respectively. From Figure 4.5(a), it is apparent that the out-of-plane electron pocket centered at Z is mainly composed of Gd d_{xy} orbitals, which form $dd\sigma$-like bonds in the <110> direction and $dd\pi$-like bonds along the <101> direction (highlighted in Figure 4.5(b), with $dd\delta$ hopping being negligible, i.e., close to 0). The heavy- (δ) and light- (β) hole bands consist of Sb p_x + p_y orbitals along $\Gamma - Z$, forming three different hopping terms $t_{1,2} = pp\pi \pm pp\sigma$ $t_3 = pp\pi$. The split-off valence band (γ) is made up of p_z orbitals. Moreover, p-d mixing in GdSb through $pd\sigma$ and $pd\pi$ bond formation is necessary to describe the sharp conduction and valence band dispersions along $Z - W$. Similarly, the in-plane electron pockets at X_1/ X_2 and δ hole band dispersing along the $\Gamma - X_{1,2}$ axis are composed of Gd d_{yz} / d_{xz} orbitals and Sb p_y + p_z / p_x + p_z orbitals, respectively.

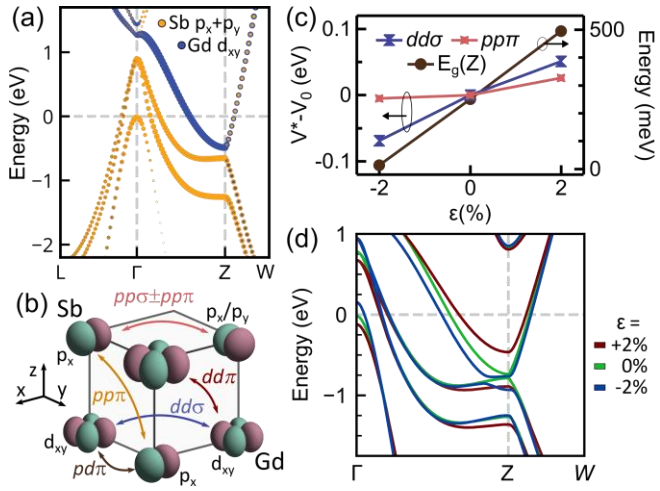

Figure 4.5. Strain effect on orbital overlap in GdSb. (**a**) Nonmagnetic DFT calculations of the electronic band structure in GdSb and the orbital character of the DFT wavefunctions. (**b**) Illustration of relevant atomic orbitals and primary interaction paths at the Z point. (**c**) Tight binding hopping term decay rate with increasing strain and the evolution of the DFT-calculated gap at the TRIM Z point vs strain. (**d**) Tight binding band structure of GdSb and its dependence on the strain level. Figure reprinted with permission from [193].

Upon applying compressive strain, the orbital overlap increases between the in-plane hopping terms of the p_x p_y d_{xy} orbitals, leading to increased dispersion in both the valence and the conduction bands. However, because the d orbital hopping terms have a stronger distance

dependence than the *p* orbitals Figure 4.5(c) [210], the electron pocket has a more significant increase in its bandwidth moving from tensile to compressive strain. This behavior also explains the topological phase transition trend observed for RE-Vs due to lanthanide contraction [60,146]. Lighter lanthanide elements have both larger ionic radius [211] and larger unit cells [202], yet overall the ratio of the lanthanide ionic radius to the RE-V unit cell increases for the lighter lanthanides, leading to higher *d-d* orbital overlap eventually resulting in band inversion, despite the decrease in *p-p* orbital overlap.

Strain-induced band inversion along $\Gamma - Z$ in Figure 4.2(h) and Figure 4.3 is reproduced in the TB model in Figure 4.5(d) and explains the more substantial modifications observed in ARPES and measured in DFT for band dispersions composed of atomic orbitals distributed within the film plane. For the in-plane electron pockets at $X_{1,2}$ under compressive strain, the *d-d* orbital overlap in the (011)/(101) faces is affected by both the reduced distance along <010>/<100> and slightly expanded out-of-plane lattice parameter along <001>. However, due to the small Poisson ratio, the total distance between the d_{xz}/d_{yz} orbitals decreases, leading to a slight reduction of the gap at $X_{1,2}$. In conclusion, the TB model demonstrates the importance of both Gd-Gd *dd*σ and Sb-Sb ppπ bonding in determining the degree of band inversion at the *Z* high-symmetry point.

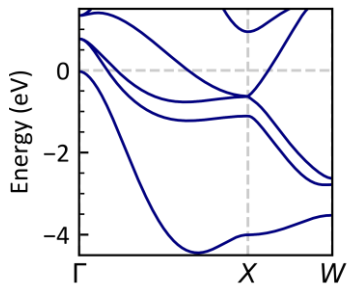

Figure 4.6. Wide energy range *E-k* dispersion based on the constructed TB model for unstrained GdSb. Figure reprinted with permission from [193].

4.5 Confinement effects

Next, we map the quantum well states in the conduction and valence bands. Two electron sub-band pockets are present for both strain levels in Figure 4.2(b). Scans of the hole pockets along $\bar{M} - \bar{\Gamma} - \bar{M}$ ($X_{1,2} - \Gamma - X_{1,2}$ in the bulk Brillouin zone) and $\bar{X} - \bar{\Gamma} - \bar{X}$ ($K - \Gamma - K$ in the bulk Brillouin zone) in Figure 4.4 show multiple quantum well states and agree with the number of subbands seen in our DFT calculations in Figure 4.7 for films of the same thickness. The same number of quantum well sub-bands and similar energy splitting for the biaxially strained films confirm the growth of atomically uniform films of the same thickness and comparable interface potentials when grown on GaSb ($\varepsilon = -2\%$) and $In_{0.65}Ga_{0.35}Sb$ ($\varepsilon = +2\%$) buffer layers.

Due to quantum size effects, the band extrema positions in the 4-nm-thick films (detailed in Table 4.1) are expected to be shifted to higher (lower) binding energies for the in-plane dispersing hole (electron) pockets at $X_{1,2}$ compared to the DFT calculations in Figure 4.2(g) performed for bulk-like GdSb. DFT calculations in Figure 4.7 modeling the effect of quantum confinement in 13 ML of GdSb (001) slabs show that the electron pockets in the film plane are experiencing quantum confinement, in contrast to the electron bands lying in the [001] direction which follow the bulk band-structure calculations. The pockets in the film plane normal direction are less susceptible to quantum confinement in the (001) plane due to their in-plane orbital composition.

In Figure 4.7, the 4 nm strained GdSb films showed an experimental shift in the γ hole band by ~ 0.1 eV away from the Fermi level and reduced Fermi wave vectors in both the light- and heavy-hole bands along $\bar{X} - \bar{\Gamma} - \bar{X}$ compared to the bulk-limit 20-nm-thick unstrained film [154]. The electron pocket second quantum well state at $\bar{M}$ is predicted to nearly graze

the Fermi level in our calculation in Figure 4.7 but experimentally lies well below the Fermi level in Figure 4.2(b). The smaller quantum well state spacing is most likely due to the finite potential barrier at the film-substrate/buffer layer interface, whereas our calculation assumes a freestanding GdSb slab.

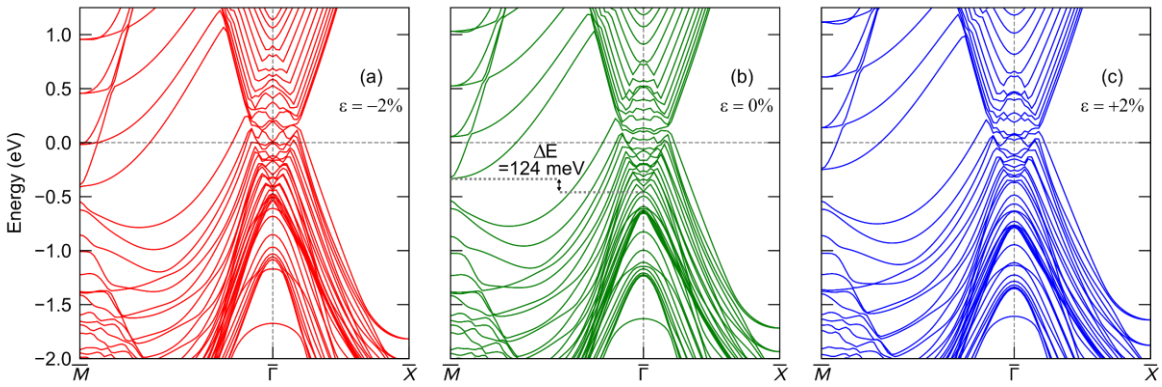

Figure 4.7. DFT-calculated electronic structure of free-standing GdSb (001) films that are 13 ML thick for (**a**) 2% compressively strained, (**b**) unstrained, and (**c**) 2% tensile strained films. The electron pockets lying in the film plane ($X_{1,2}$, projecting to $\bar{M}$) shift to higher energies compared to the electron pockets in the film plane normal direction (Z, projecting to $\bar{\Gamma}$), with an energy difference of 124 meV calculated for the unstrained film. Figure reprinted with permission from [193].

A modest change in the concentration of all charge carriers is seen as a function of strain (see chapter 3.5 for details on the carrier density analysis). Overall, the charge carrier ratio increases with compressive strain from $\left(\frac{n_e}{n_h}\right)_{+2\%} = 1.52$ to $\left(\frac{n_e}{n_h}\right)_{-2\%} = 1.85$, suggesting that biaxial strain could serve as another degree of freedom to tune magnetoresistance in RE-Vs. As in past observations for LuSb [57] (a nonmagnetic RE-V analog), due to quantum confinement effects in the 4-nm-thick films, the Fermi surface area of the hole pockets and the electron pockets in the strained thin films is slightly smaller than the values extracted via ARPES for thicker unstrained GdSb films [154]. The electron-rich carrier ratio measured for both thin films, deviating from exact compensation in unstrained bulk GdSb, agrees with our earlier studies of quantum confinement effects in RE-Vs [57].

4.6 Magnetic properties of strained GdSb films

Finally, we address the effect of strain on the magnetic properties of GdSb. Due to the absence of orbital angular momentum in the $4f^7$ configuration of the Gd^{3+} ion, GdSb represents an ideal isotropic Heisenberg model system for studying magnetic exchange interactions. GdSb can be considered a parent compound of the half-Heusler structure GdPtV (V = Bi, Sb), which shows complex behavior, such as an antiferromagnetic to ferromagnetic transition in GdPtSb due to strain gradients [33] and chiral anomaly and anisotropic magnetotransport in the predicted Weyl semimetal GdPtBi [212].

GdSb can be considered an orbitally quenched system since the $4f^7$ configuration results in zero orbital angular momentum. Therefore, there is a negligible crystalline electric field (CEF) effect. The weak CEF effect in GdSb permits us to overlook the impact of strain on local symmetry breaking and to easily elucidate the role strain-driven band structure modifications and orbital overlap might have on magnetic ordering in GdSb. The 4*f* electrons in GdSb are well localized, with occupied states at 8.7 eV below the Fermi level [155]. Superexchange interactions (via *p-d* hopping in Gd-Sb) and Ruderman-Kittel-Kasuya-Yosida (RKKY) indirect-exchange interactions are expected to coexist in this compound [213], the former leading to antiferromagnetic behavior, and the latter contributing to a competing ferromagnetic order. Assuming a molecular field approximation can describe well the ordering in GdSb [141], the Néel Temperature (T_N) of a type II Heisenberg AFM with S=7/2 is [214]:

$$k_B T_N = \frac{2}{3} S(S+1)\hbar^2(-6J_2) = -63\hbar^2 J_2$$

J_2 being the next nearest neighbor exchange constant. The pnictogen *p*-orbitals mediate the AFM superexchange interactions between the Gd atoms, and J_2 can be expressed by the

empirical relation used for transition-metal compounds: $J_2^{super} = -\frac{n_d t_{pd}^4}{\Delta^2}\left(\frac{1}{U}+\frac{1}{\Delta}\right)$ where n_d is the *d* moment induced by intra-atomic *5f-4d* exchange, t_{pd} is the hopping integral between the Sb-*p* and Gd-*d* orbitals, *U* is the on-site coulomb energy and Δ is the energy difference between the *d* and *p* orbitals [213,215]. From Table 4.2, we can see that both $t_{pd\sigma}$ and $t_{pd\pi}$ hopping terms increase (in absolute value) moving from tensile to compressive strain, in agreement with the stronger superexchange interaction expected with decreasing lattice constant.

The electrical resistivity of the GdSb films, shown in Figure 4.8 is measured between 2 and 70 K (above 70 K the III-V buffer layer and GaSb substrate contribute to transport), in order to estimate T_N for the two GdSb strain levels. The resistivity measured for the 4 nm thick −2% biaxial strained film (without a metamorphic buffer contributing to the film roughness and scattering) is $\rho^{-2\%}(2K, B = 0\,T) = 84\,\mu\Omega - cm$. A resistivity kink near the Néel temperature is typically seen for RE-V bulk crystals in an otherwise linear temperature dependence, in good agreement with specific-heat measurements and magnetic-susceptibility data [142,145,216]. A monotonic increase in T_N (including the lattice-matched film results [154]) is measured as a function of strain. T_N in the thin films is inferred from the kink in the resistivity temperature dependence, similar to features previously reported in GdSb bulk single crystals [142,145,216] and RE-V thin films [163]. A 2.6 °C increase in T_N from +2% tensile (24.3 K) to −2% compressive (26.9 K) strained films is observed in Figure 4.8. Similar strain-dependent changes were measured for EuTe, an S=7/2 rare-earth analogue [217]. However, the superexchange parameter J_2 in GdSb is predicted to be much larger and more sensitive to variations in the lattice constant [141]. Based on our TB model, a reduction in the lattice parameter results in increased *p-d* orbital hopping, which in turn, leads to a higher T_N. To our knowledge, this is the first study showing the direct impact of epitaxial strain on

superexchange *p-d* hopping in a RE-V and could guide future efforts in strain tuning the magnetic ordering temperature of additional materials beyond the RE-V family. Building on these results, the effect of strain/pressure in other RE-Vs with more complex magnetic behavior, such as Ce-V [52] and Eu-VI [217], can be modeled or applied to semiconducting RE-V nitrides, such as ScN [218] and GdN [196].

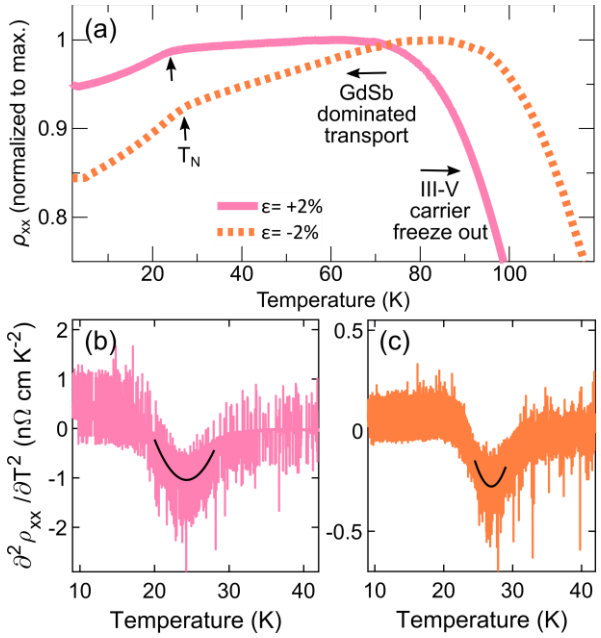

Figure 4.8. Néel temperature in strained 4-nm-thick GdSb films. (**a**) Temperature dependence of the longitudinal resistivity normalized to the maximum resistivity. At high temperatures > 70 K, transport is dominated by the III-V substrate and/or buffer layer. Under 70 K, the charge carriers in the III-V buffer layer and GaSb substrate freeze out, and transport is dominated by the GdSb films. (**b-c**) Néel temperature extracted from a parabolic fit (black line) to the second derivative of the resistivity at B=0 T, for (**b**) +2% strain (T_N=24.3 K) and (**c**) −2% biaxial strain (T_N=26.9 K). Figure reprinted with permission from [193].

4.7 Conclusions

In summary, we have followed with ARPES and DFT the evolution of the bulk band structure in biaxial strained GdSb quantum wells and demonstrated the tuning of bandgaps in RE-Vs through epitaxial strain. We report the successful growth of strained GdSb films integrated with a conventional III-V semiconducting substrate, and the resulting trends in magnetic ordering temperature and charge carrier ratios are discussed. The synthesis of high-

quality epitaxial GdSb is an important step toward practical control of transport characteristics in magnetic Weyl semimetals. Our TB model based on nearest and next-nearest neighbor interactions describes well the electronic structure of GdSb. We have shown that biaxial compressive strain is expected to promote *d-d* hopping in the rare earth t_{2g} conduction bands to a larger extent than the pnictogen *p* band hopping, resulting in band inversion and a higher electron carrier density. This work opens the door to future studies of strain-controlled topological phase transitions and semimetal-semiconductor transitions in RE-Vs and RE-V derived compounds, such as topological half-Heusler alloys (RE Pt/Pd V) [97–99].

5 Inversion symmetry breaking in epitaxial ultrathin Bi (111) films

5.1 Introduction

Scientists have studied strain and quantum size effects in bismuth (Bi) (111) films for decades, which provide a rich platform for tuning topological order [62], semimetal to semiconducting transitions [63], and quantum-well states [64]. The low carrier density, long mean free path, large spin-orbit coupling, and presence of spin-polarized surface states [65] have made Bi films a promising system for future applications in spintronics [66]. Group-V elemental two-dimensional (2D) layers have also attracted interest in classical electronic and optoelectronic device applications due to their high carrier mobility and potential bandgap tunability [67]. The large mass anisotropy in the surface state and the bulk band valleys in the band structure of Bi allow valley degeneracy to be controlled by the orientation of an applied magnetic field, a feature that can be used in valleytronic devices which encode information through valley-polarized currents [68].

In the field of topological materials, there is an ongoing effort to classify the $\mathbb{Z}_2$ invariant of Bi experimentally [32,72], which also proves challenging to calculate computationally [73]. A single Bi (111) bilayer (BL) with a nontrivial $\mathbb{Z}_2$ topological number is predicted to behave as a quantum spin Hall insulator [74]. Along the Bi (111) step edges (running perpendicular to $\langle\bar{1}\ \bar{1}\ 2\rangle$) one-dimensional (1D) helical modes were also observed [71], an ingredient in one proposed platform to construct Majorana zero modes [76]. Yet, the synthesis of the (111) rhombohedral phase on a semiconducting substrate has remained elusive, with only planar bismuthene wetting layers on SiC reported thus far [79]. The synthesis of large-area, single-

domain ultrathin (<6 BL) buckled Bi (111) epitaxial films on semiconducting substrates has remained a materials science challenge for many decades. For Si or Ge (111) substrates, weak film-substrate van der Waals (vdW) interactions [84] have led to the nucleation of a nearly freestanding-like Bi layer. Due to weak epitaxial stabilization, a competing black phosphorus-like pseudocubic {012} allotropic phase is favorable in the few-BL growth regime. The pseudocubic phase transforms to the (111) rhombohedral phase only after the film coalesces beyond a thickness of 6 BL for Si(111) [77]. Ultrathin Bi (111) films were nucleated on metallic substrates such as highly oriented pyrolytic graphite [219] and the topological insulator substrate Bi_2Te_3 [86–89]. However, those films suffer from parallel conduction paths from the underlying metallic bulk or surface states of the substrate with which they hybridize.

Bulk Bi in the rhombohedral A7 structure (space group $R\bar{3}m$,) is a low-carrier semimetal (Figure 5.1, A and B) with a valence-band maximum at the time-reversal invariant momentum (TRIM) T point (projecting to $\bar{\Gamma}$ for the (111) surface) and a conduction-band minimum at the L TRIM point (projecting to $\bar{M}$). The small direct bandgap at the L point is only a few meV and determines whether Bi is a topological insulator (an inverted bandgap at L) or a higher-order topological insulator (no band inversion at L).

Bi is predicted to lie at the border of a topological phase transition between a higher-order topological insulator and a topological insulator phase [32]. Calculations have shown that the indirect T-L gap and the direct inversion bandgap at L depend on electron doping [93], biaxial and shear strain [32,62,87], and bulk alloying in $Bi_{1-x}Sb_x$ [4]. Yet despite the challenge of estimating the gap size at the L point, most DFT calculations [62,73] predict a trivial band order at the L point for unstrained bulk Bi crystals. More accurate quasiparticle self-consistent

GW (*QSGW*) calculations also yield nontrivial behavior, with a gap at L of 13 meV compared to 86 meV in standard DFT [62].

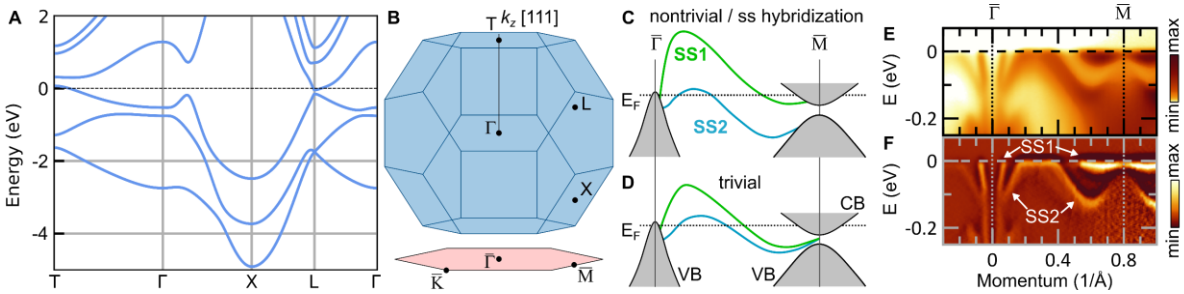

Figure 5.1. Surface state dispersion of Bi (111) (**A**) Calculated bulk band structure of Bi showing the hole and electron pockets at the TRIM points T and L, respectively. (**B**) Schematic of the bulk Brillouin zone and TRIM points projected onto the (111) surface Brillouin zone. (**C** and **D**) Schematic drawings of two possible surface state (SS) dispersions and projected valence and conduction bands (VB, CB) along $\bar{\Gamma} - \bar{M}$ (**C**) Connectivity of SS1 and SS2 with the CB and VB, respectively, at the $\bar{M}$ point. The SS gap could indicate either a topologically nontrivial band structure for a semi-infinite crystal or interactions between surface states at the top and bottom surfaces in a thin film. (**D**) Surface state degeneracy at $\bar{M}$, indicating a $\mathbb{Z}_2$ trivial band structure. (**E** and **F**) ARPES *E*-*k* dispersion of the surface states at $h\nu$ = 37.5 eV for a 200 BL thick film Bi (111) film grown on InSb (111)B presenting a very small/nonexistent gap at the $\bar{M}$ point. (**E**) Raw data and the (**F**) curvature plot [220] of the raw data, enhancing dispersive features. Figure reprinted with permission from [221].

ARPES measurements [69,72,94] of Bi thin films have nonetheless shown surface states gapped at the $\bar{M}$ point, which in the past were attributed to a $\mathbb{Z}_2$ nontrivial band topology (Figure 5.1C). Since the surface states near the Brillouin-zone edge penetrate deep into the film bulk, on the order of 100s of bilayers [73,95,96], crosstalk between surface states on neighboring surfaces could lead to the formation of a hybridization gap and the appearance of a topological-like signature even in the trivial semimetal case (Figure 5.1C). ARPES spectra of films as thick as 200 BL grown on Ge (111) still show gapped surface states lying close to each other [72], obscuring the direct determination of a surface state gap/degeneracy even for relatively thick films.

Recent *ab initio* calculations have predicted that in an inversion a-symmetric film (resulting from surface perturbations/functionalization [222,223] or inter/intra-bilayer expansion [224]), one could more easily distinguish between the topologically trivial and nontrivial phases due to the emergence of degenerate surface states observed only from one

surface, as schematically portrayed in Figure 5.1D. Thus, in order to study the true topological nature of Bi, a substrate/overlayer with strong bonding to Bi films would break inversion symmetry and prevent surface state hybridization, facilitating the topological phase assignment of Bi. In this work, we have identified a semiconducting substrate, InSb (111)B, satisfying this condition and allowing us to break inversion symmetry in epitaxial Bi films through strong film-substrate interactions. Unlike previously explored substrates, these strong interactions allow us to stabilize ultrathin (<6 BL) large-area Bi films in the (111) orientation down to 1 BL thick films and take advantage of the film-substrate interface perturbation to study only the top surface of the Bi film with ARPES and DFT.

5.2 Growth and epitaxy of Bi (111) on InSb (111)B

A well-ordered (3×3) surface of unintentionally doped epi-ready InSb (111)B wafers (Wafer Technology Ltd.) was prepared with atomic hydrogen cleaning for native oxide removal and was studied *in vacuo* with RHEED and STM [225]. To hydrogen clean the samples, the samples were heated to 360 ^{o}C, as measured by a thermocouple near the sample, and exposed for an hour to a chamber pressure of 5×10^{-6} Torr of atomic hydrogen, as measured by an ion gauge in the chamber. The atomic hydrogen was generated by flowing hydrogen gas through a leak valve and into a thermal cracker (Dr. Eberl MBE-Komponenten GmbH) operated at 1700 ^{o}C. Following hydrogen cleaning the substrate was cooled at a slow rate (≤5 ^{o}C/min) to room temperature to obtain a (3×3) surface, otherwise for faster cooling rates a metastable (3×1) surface reconstruction was obtained. The starting (111)B face was selected due to previous reports predicting improved wetting over InSb (111)A [226]. Layer-by-layer growth was observed for Bi nucleated both on the InSb (3×3) In-rich and (2×2) Sb-rich surface

reconstructions, with a (3×3) reconstruction selected in this study to avoid unintentional Sb doping of the Bi film [227].

The thin Bi (111) films were grown by MBE in a MOD Gen II growth chamber with a base pressure <$1x10^{-10}$ Torr. Bi was evaporated from a conventional effusion cell with a pyrolytic boron nitride crucible at a temperature of 482 ^{o}C with a deposition rate of $1.9x10^{14}$ atoms/cm^{2}min, determined by Rutherford backscattering spectrometry measurements of the elemental area atomic density of calibration samples grown on Si. The nominal thickness is represented in units of bilayers (BLs), where 1 BL corresponds to the 2 ML atom density in (111) planes assuming lattice matching to the underlying InSb substrate (a_{Bi}^{InSb}=4.582 Å): $1.10x10^{15}$ atoms/cm^2 (see Figure 5.2(A-C)). The surface crystal quality was monitored *in situ* with RHEED during film growth and post-annealing. Thin films are nucleated at 14 ^{o}C followed by low-temperature annealing at 80-120 ^{o}C for several hours to allow local ordering of the Bi atoms but avoid film dewetting observed at higher temperatures. Hotter annealing temperatures led to three-dimensional islands, confirmed by STM, and showed up in RHEED as a dim (2×1) pattern. The samples were transferred *in vacuo* for ARPES and STM measurements and were eventually capped with a 5-nm-thick AlO_x layer deposited by electron-beam evaporation of Al_2O_3 source material to prevent film oxidation and dewetting when loaded out of ultrahigh-vacuum for *ex situ* characterization.

Figure 5.2(A-C) shows the epitaxial relationship between the InSb (111)B substrate and the $(111)_r/(0001)_{hex}$ Bi film. The (111) rhombohedral orientation of Bi can also be simplified using the (0001) quasi-hexagonal unit cell shown in Figure 5.2A, where 3 BL (BL=3.95 Å) define the out-of-plane lattice constant of c_0=11.862 Å, with the in-plane lattice constant a_0=4.546 Å [228]. Each Bi BL has a buckled structure with a vdW-like gap separating the

bilayers. The lattice mismatch between the bulk Bi lattice constant and InSb <110> atomic spacing is small, with only 0.8% nominal biaxial tensile strain applied to the Bi film. RHEED patterns in Figure 5.2D confirm the nucleation of smooth (1×1) unreconstructed Bi films on a well-ordered (3×3) InSb (111)B surface reconstruction.

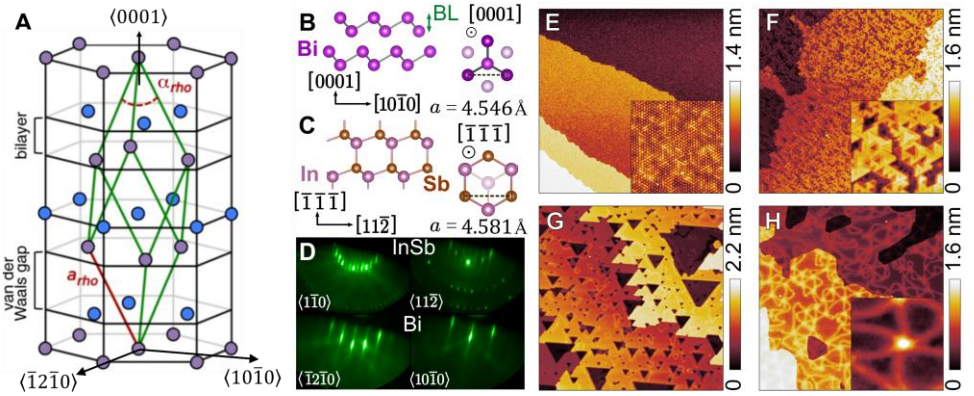

Figure 5.2. (**A**) Rhombohedral (green) unit cell and hexagonal crystal structure of bulk Bi. Purple and blue atoms are at the bottom and top row of each bilayer, respectively. Adapted from [62]. The Side and top-view models of (**B**) the Bi $(0001)_{hex}$ surface ($(111)_r$ in the rhombohedral notation) illustrating intralayer covalent-like bonds and interlayer vdW stacking and (**C**) InSb (111)B unreconstructed surface. (**D**) RHEED patterns and epitaxial alignment of the (3×3) InSb (111)B substrate and (1×1) Bi $(0001)_{hex}$ surface. (**E - H**) STM images of InSb and ultrathin Bi films 400×400 nm^2. (**E**) InSb (111)B substrate (bias voltage, V_b: 1.2 V), 20×20 nm^2 inset exhibits the atomic resolution of the (3×3) surface reconstruction (V_b: 1 V). (**F**) 1 BL Bi film (V_b: 3 V). 50×50 nm^2 inset depicts the fractal pattern (V_b: 3 V). (**G**) 2.6 BL Bi film, featuring continuous coverage above the percolation threshold; exposed patch area and density determined by annealing duration (V_b: 3 V). (**H**) 5.4 BL thick film, showing progressive film relaxation (V_b: 3 V); 50×50 nm^2 inset highlights a soliton node (V_b: 0.25 V). Figure reprinted with permission from [221].

In vacuo STM was performed with an Omicron LT STM at 77 K with a base pressure $< 4 \times 10^{-11}$ Torr. STM images in Figure 5.2(E-H) show the evolution of the ultrathin film morphology with film thickness. In Figure 5.2, an atomically smooth InSb (111)B starting surface is measured, with an atomic (3×3) surface reconstruction (Figure 5.2D, inset) consistent with previous observations [229]. Following the deposition of 1 BL, the Bi film evolves into a fractal Sierpiński triangle-like structure (Figure 5.2F) which was recently reported for the same film-substrate system [229]. Examining line profiles, the step height between the first bilayer and InSb is 358±3 pm, smaller than the spacing expected from the trigonal lattice constant of pseudomorphic bismuth films measured via XRD (at 298K,

$d_{vdW}+d_{BL}$=394±1 pm) or thicker bilayer spacing measured via STM (at 78K: $d_{vdW}+d_{BL}$=391±1 pm). The spacing measured via STM convolutes both structural and electronic effects, however could indicate strong interactions between the Bi film and InSb. For Bi films with a thickness of 2-3 BL, the fractal pattern transforms to a uniform coverage of (111) oriented Bi with 1-2 BL steps and wetting layer patch areas. In Figure 5.2G, we observe only a single domain orientation in our STM images, unlike the common rotational domains seen thus far for thin Bi films [85].

Lattice parameters, film thickness, and crystallinity information were extracted from high-resolution x-ray diffraction in Figure 5.3 and confirmed that the films have high crystalline ordering and sharp interfaces. The azimuthal alignment and in-plane strain are further studied with STM (Figure 5.2) and XRD (Figure 5.3), where the epitaxial film-substrate relationship and film strain relaxation are monitored as a function of film thickness. The large-area single domain orientation observed for Bi (111)/InSb(111)B is in contrast to the two rotational domains typically seen for Bi films nucleated on Si (111) [85]. It was shown via STM that coherent strain is maintained in the film only up to a thickness of 2 BL. Films thicker than 2 BL begin to partially relax and form a soliton network, a unique strain relief mechanism in vdW materials [230], which was observed in Bi films only when grown on InSb [229,231]. The relaxed soliton network is also evident in Figure 5.2H for a 5.4 BL film. Reciprocal space maps (RSMs) of the Bi ($1\ 0\ \bar{1}\ 11$) peak for the 5.4 and 13 BL samples are shown in Figure 5.3(C and D). The RSMs reveal the film has significant biaxial strain at the ultrathin limit, in agreement with the experimental Poisson ratio of 0.28 for basal plane biaxial strain [232]. The thinner sample has the diffracted intensity mostly centered at the InSb in-plane lattice constant (with strained lattice parameters: a_s=4.58 Å, c_s=11.81 Å), whereas the thicker 13 BL film has

the peak weight shifted to a smaller in-plane lattice constant due to more significant relaxation, yet maintains a fraction of a coherently strained film even after strain relaxation occurs (a_s =4.58 Å, c_s =11.86 Å, and for the relaxed peak: a_R =4.524 Å, c_R =11.892 Å).

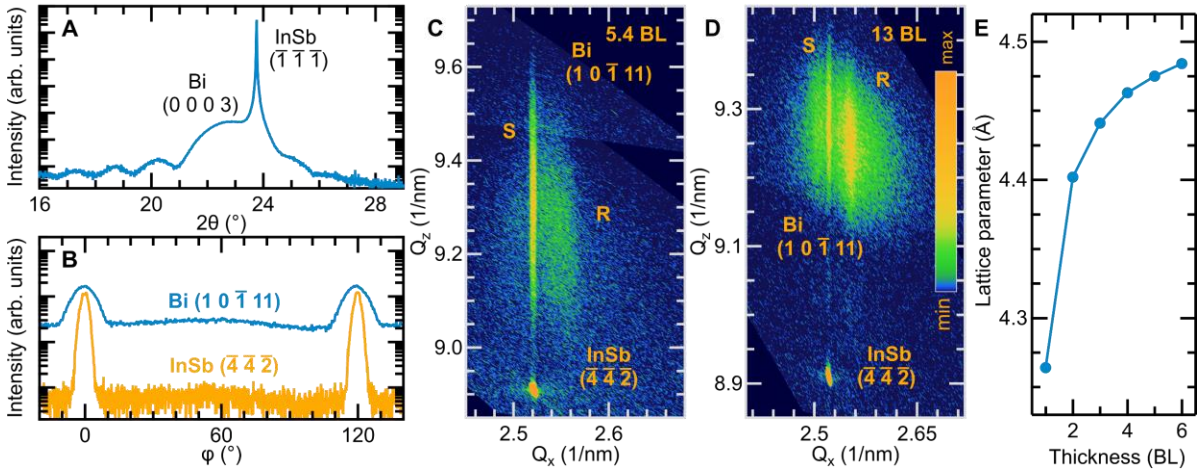

Figure 5.3. Epitaxy of bismuth on InSb (111)B. **(A)** θ-2θ XRD scan exhibiting thickness fringes indicating a sharp interface. (**B**) In-plane φ scan of the Bi (1 0 $\bar{1}$ 11) and InSb ($\bar{4}$ $\bar{4}$ $\bar{2}$) reflections showing the 3-fold symmetry of a single crystal domain orientation. Reciprocal space map of (**C**) 5.4 BL and a (**D**) 13 BL thick film showing partial relaxation, with both coherently strained (S) and relaxed peaks (R) present. (**E**) DFT-calculated lattice parameter of freestanding ultrathin Bi films vs. film thickness, see section 5.3.2 for details.

Interestingly, the relaxed in-plane (a) and trigonal (c) lattice constants shrink/expand (respectively) compared to the literature bulk crystal lattice constants of a=4.546 Å, c =11.862 Å [228]. This contraction in a for thinner films and expansion in c was predicted in computational studies of Bi (111) nanofilms [233] and was also reproduced in our DFT calculations for freestanding films (Figure 5.3E, see section 5.3.2 for details) and would explain the early onset of strain relaxation observed in our STM scans with tensile strain as high as 3% possible at the 2 BL limit. Therefore, a lattice mismatch higher than the nominal 0.8% tensile strain (with respect to the Bi bulk lattice constant) is applied at the ultrathin limit when Bi is nucleated on InSb. Bi films thicker than 30BL are fully relaxed in the topmost bilayer, presenting no biaxial strain [231].

5.3 Electronic structure of ultrathin Bi (111) films

5.3.1 Photoemission spectra

ARPES measurements at the Advanced Light Source (ALS) at Lawrence Berkeley National Laboratory were conducted at 11 K and acquired with a Scienta DA30L hemispherical analyzer. The ALS measurements were performed on *in vacuo* transferred samples, where a custom-built vacuum suitcase with a base pressure $<10^{-10}$ Torr was used to transfer films from the growth chamber at UCSB to beamline 10.0.1.2 at the ALS in Berkeley.

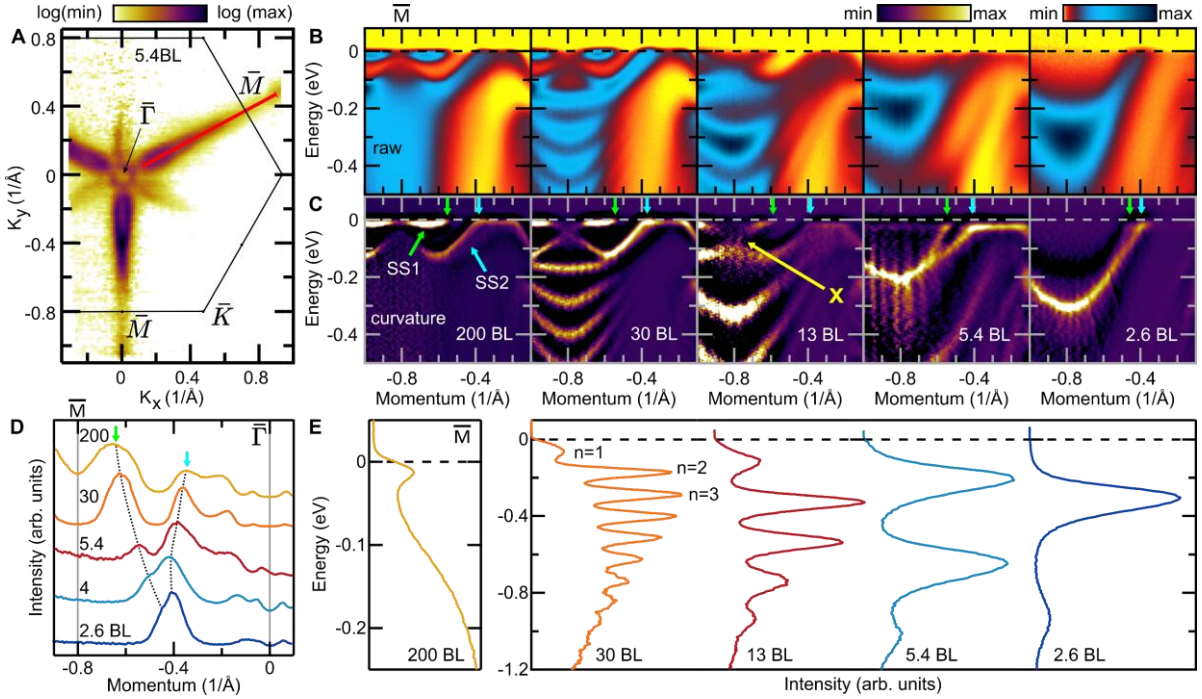

Figure 5.4. Fermi surface and surface states measured with ARPES at an incident photon energy $h\nu$ = 37.5 eV for various film thicknesses. (**A**) Fermi surface of a 5.4 BL thick Bi (111) film at the Fermi energy, E_F. The corresponding E–k cut along the $\bar{\Gamma} - \bar{M}$ path in (**B**) and (**C**) is highlighted. (**B**) ARPES raw images and (**C**) curvature plots, enhancing the dispersive features of the surface states (SS1, SS2) and quantum-well states. The surface state band degeneracy at $\bar{M}$ ($k = 0.8$ Å^{-1}), marked by X, is observed due to inversion symmetry breaking. (**D**) Momentum distribution curves at E_F. The surface state Fermi level crossings near $\bar{M}$, highlighted by arrows in (**C**) and (**D**), decrease in separation as the films become thinner. (**E**) Energy distribution curves at the $\bar{M}$ point showing the evolution in quantum-well state energy spacing as a function of film thickness. Figure reprinted with permission from [221].

Figure 5.4A shows the Fermi surface of a 5.4 BL Bi film measured using ARPES, presenting a dominant three-fold symmetry as the surface states disperse from the valence band

at $\bar{\Gamma}$ towards the valence and electron pocket at $\bar{M}$ (Figure 5.1) indicating a single epitaxial domain orientation and in agreement with the STM measurements. In Figure 5.4(B and C) we present narrow energy-range ARPES measurements along $\bar{\Gamma} - \bar{M}$ for Bi films with varying thicknesses (wide energy range scans provided in Figure 5.5). Due to the small bulk carrier density, quantum confinement effects in Bi films emerge for films 10s of bilayers thick, leading to well-resolved quantum-well states for all films thinner than 200 BL. Despite the ultrathin thickness of the Bi films studied (< 6 BL), we do not observe in ARPES any bands originating from the underlying InSb substrate, as confirmed by examining a reference InSb (3×3) reconstructed surface in Figure 5.6.

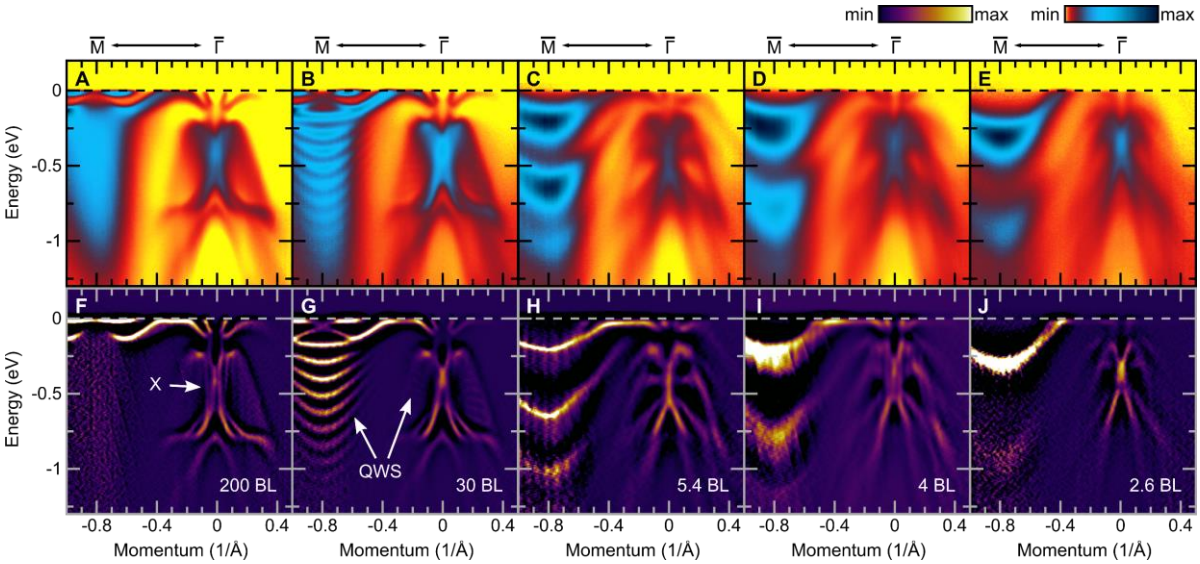

Figure 5.5. ARPES spectra of Bi films along $\bar{M} - \bar{\Gamma}$ over a wide energy range. ARPES images of the raw spectra (**A**-**E**) and two-dimensional curvature plots (**F**-**J**), enhancing the dispersive band features. Quantum-well states (QWS) and the crossing of the second pair of surface states at ~0.5 eV, marked by X, are highlighted. The spectra are measured at an incident photon energy *hv* = 37.5 eV. Figure reprinted with permission from [221].

In Figure 5.5, four Fermi-level band crossings are observed along $\bar{M} - \bar{\Gamma}$, twice for each surface state band highlighted in Figure 5.4. An additional set of surface state bands [234] is centered at the $\bar{\Gamma}$ point near 0.2-0.6 eV with a crossing marked by X in Figure 5.5. The valence bulk bands at the T and L high-symmetry points were not detected for any of the Bi films over

an energy range of 18-60 eV in Figure 5.4, Figure 5.5, Figure 5.8, and Figure 5.9 owing to their low cross-section compared to the surface states. As the surface states (crossing the Fermi level) disperse towards $\bar{M}$, additional quantum-well states are observed due to the hybridization of the surface states with the quantum-well states originating from the bulk band (and additional bulk quantum-well states are also apparent at the $\bar{\Gamma}$ point).

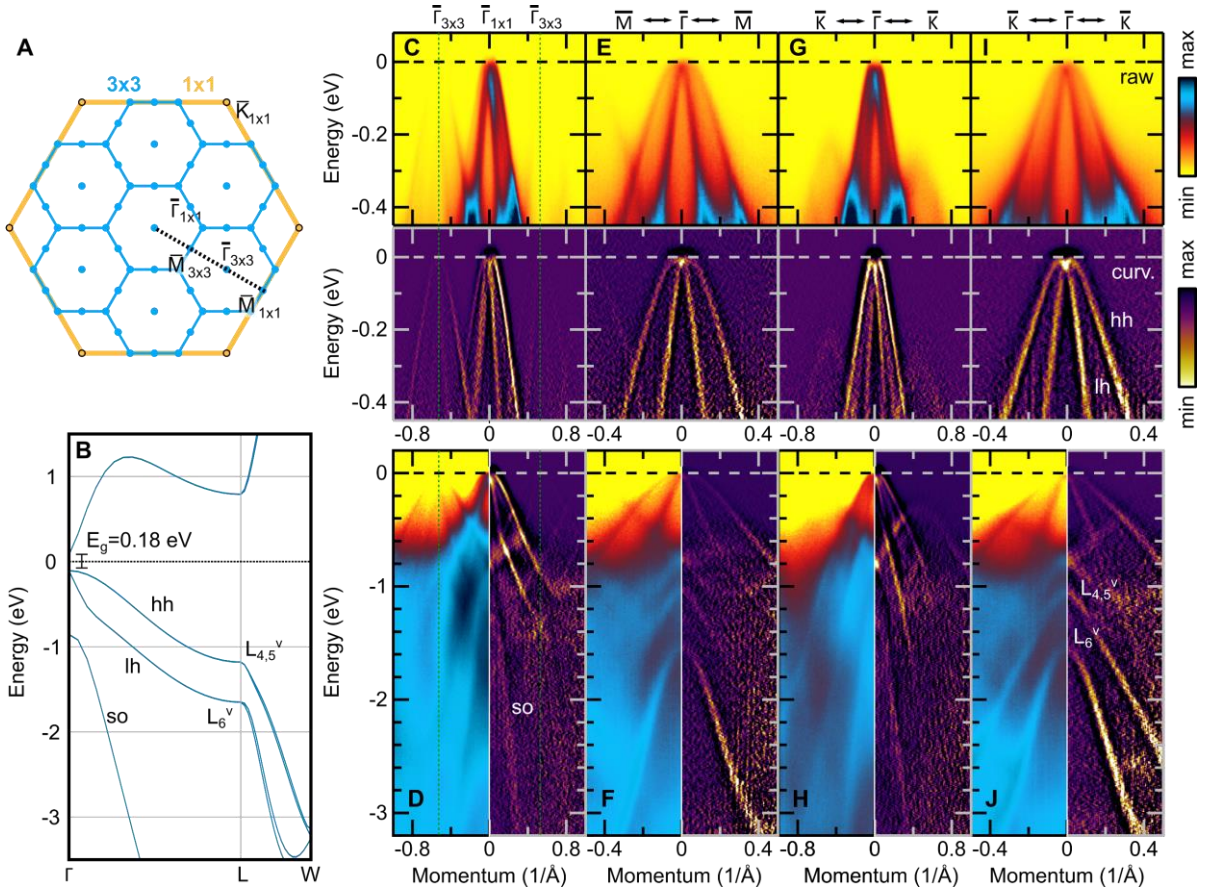

Figure 5.6. InSb surface and bulk band structure and ARPES spectra. (**A**) Surface Brillouin zone and symmetry points of the (1x1) unreconstructed (orange) and (3×3) reconstructed surface (blue) of InSb (111)B. (**B**) HSE06-calculated band structure of InSb showing the heavy-hole (hh), light-hole (lh), and split-off (so) bands. (**C-J**) ARPES images of the raw spectra (top/left panels) and two-dimensional curvature plots, enhancing the dispersive band features (bottom/right panels). (**C-D**) $\bar{M}-\bar{\Gamma}-\bar{M}$ cuts collected at an incident photon energy $h\nu$ = 37.5 eV for (**C**) narrow and (**D**) wide energy ranges. Shadow bands due to the (3×3) surface reconstruction are marked by green lines. (**E-F**) $\bar{M}-\bar{\Gamma}-\bar{M}$ cuts at an incident photon energy $h\nu$ = 20 eV for (**E**) narrow and (**F**) wide energy ranges. (**G-H**) $\bar{K}-\bar{\Gamma}-\bar{K}$ cuts at an incident photon energy $h\nu$ = 37.5 eV for (**G**) narrow and (**H**) wide energy ranges. (**I-J**) $\bar{K}-\bar{\Gamma}-\bar{K}$ cuts at an incident photon energy $h\nu$ = 20 eV for (**I**) narrow and (**J**) wide energy ranges. Figure reprinted with permission from [221].

Figure 5.6 shows reference ARPES images for the atomic hydrogen-cleaned InSb (111)B substrate, collected at the same photon energies and *E-k* cut directions used for studying the Bi films. We observe bulk valence bands and surface shadow bands due to the (3×3) surface reconstruction (resulting in the folding of the surface Brillouin zone, as shown in Figure 5.6A). At $h\nu$ = 37.5 eV (Figure 5.6, C and D), there is a resonant enhancement of the valence band photoemission cross-section due to the proximity in energy to the Sb $4d \rightarrow 5p$ (valence band) transition, also leading to a stronger intensity of the shadow bands. While the photon energies of 37.5 and 20 eV should reflect cuts near the bulk Γ and L points [235] (see Figure 5.6B), respectively, the valence band dispersion remains essentially unchanged, with the addition of bands centered at L for the 20 eV scans, indicating high k_z broadening. The InSb bands in Figure 5.6 are not apparent in any of the Bi film ARPES measurements. Since InSb has a finite bandgap of 0.235 eV [236], the valence band maximum in Figure 5.6 was set to the Fermi level position as it was shown in scanning tunneling spectroscopy measurements that the Fermi level of the (3×3) InSb (111)B surface is pinned near the valence band edge [225]. However, based on Bi/InSb Fermi level calibrations, the Fermi level position is likely 0.17 eV above the valence band maximum, which also yielded better agreement with literature values of InSb photoemission core level binding energies [237].

Figure 5.7 presents the ultraviolet photoemission spectra collected as a function of the Bi film thickness for the Bi $5d_{5/2}$, Sb 4*d*, and In 4*d* core levels. A survey scan of the 1.3 BL film in Figure 5.7A shows Bi 5*d* core levels with an intensity order of magnitude higher than the In and Sb-related peaks. The quenched intensity of the Sb and In peaks following the growth of just a few bilayers highlights the smooth InSb starting surface and the layer-by-layer growth of the Bi film. In Figure 5.7B**,** the 1.3 BL Bi $5d_{5/2}$ peak presents additional components at a

higher binding energy, either due to Bi-Sb bonds forming at the Bi-InSb (111)B interface or due to surface components related to Bi atoms with dangling bonds on the fractal-like surface (see Figure 5.2). Upon increasing Bi film thickness, the Bi lineshape evolves into the bulk-like core level spectra with no pronounced change in the Bi core level binding energy.

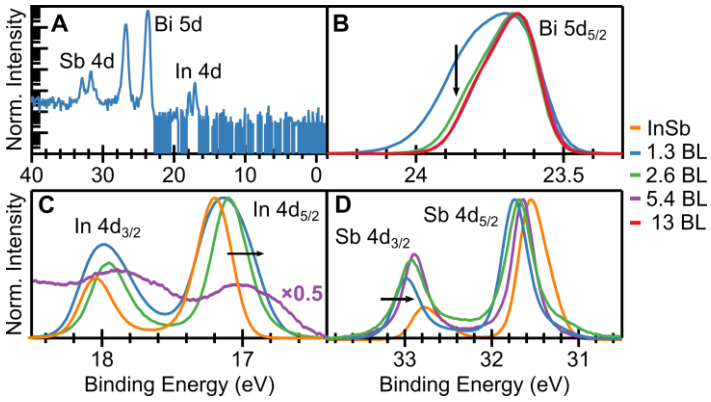

Figure 5.7. Bi-InSb interfacial bonding revealed by ultraviolet photoemission scans collected for the InSb (111)B (3×3) surface and Bi thin films with varying thicknesses. (**A**) Log-scale survey spectrum of the 1.3 BL Bi film collected at 80 eV. Photoemission spectra of (**B**) Bi $5d_{5/2}$ measured at 80 eV, (**C**) In 4d at 50 eV, and (**D**) Sb 4d at 80 eV. In (**B**) the arrow indicates the transition from a single BL to bulk-like Bi lineshape. The higher binding energy component present for 1 BL bismuth could be either due to bonding with InSb or due to another surface core level that is specific to the 1BL fractal pattern. Arrows in (**C**) and (**D**) highlight the decreasing binding energies of both Sb and In peaks with increasing Bi film thickness. Figure reprinted with permission from [221].

In Figure 5.7C, a single In 4*d* core level bulk component is used to fit the InSb substrate spectra (In $4d_{5/2}$ = 17.18 eV , In $4d_{3/2}$ = 18.01 eV), and upon Bi deposition, a gradual decrease in binding energies is observed as the Bi film thickness increases. This shift in the In 4*d* spectra could be related to In-Bi bonds forming and/or band-bending in InSb (Fermi level pinning near the InSb valence band). In Figure 5.7D, two Sb 4*d* core level components are used to fit the InSb spectra: Sb $4d_{5/2}$ = 31.38 eV, 31.58 eV, and Sb $4d_{3/2}$ = 32.82 eV, 32.62 eV in agreement with previous photoemission measurements [237]. A sharp jump in the Sb 4*d* binding energy occurs upon Bi deposition. This shift could result from Sb-Bi bonds forming at the Bi-InSb interface. Similar to In 4*d*, the Sb core level binding energies decrease with increasing Bi film thickness, indicating Fermi level pinning near the InSb valence band.

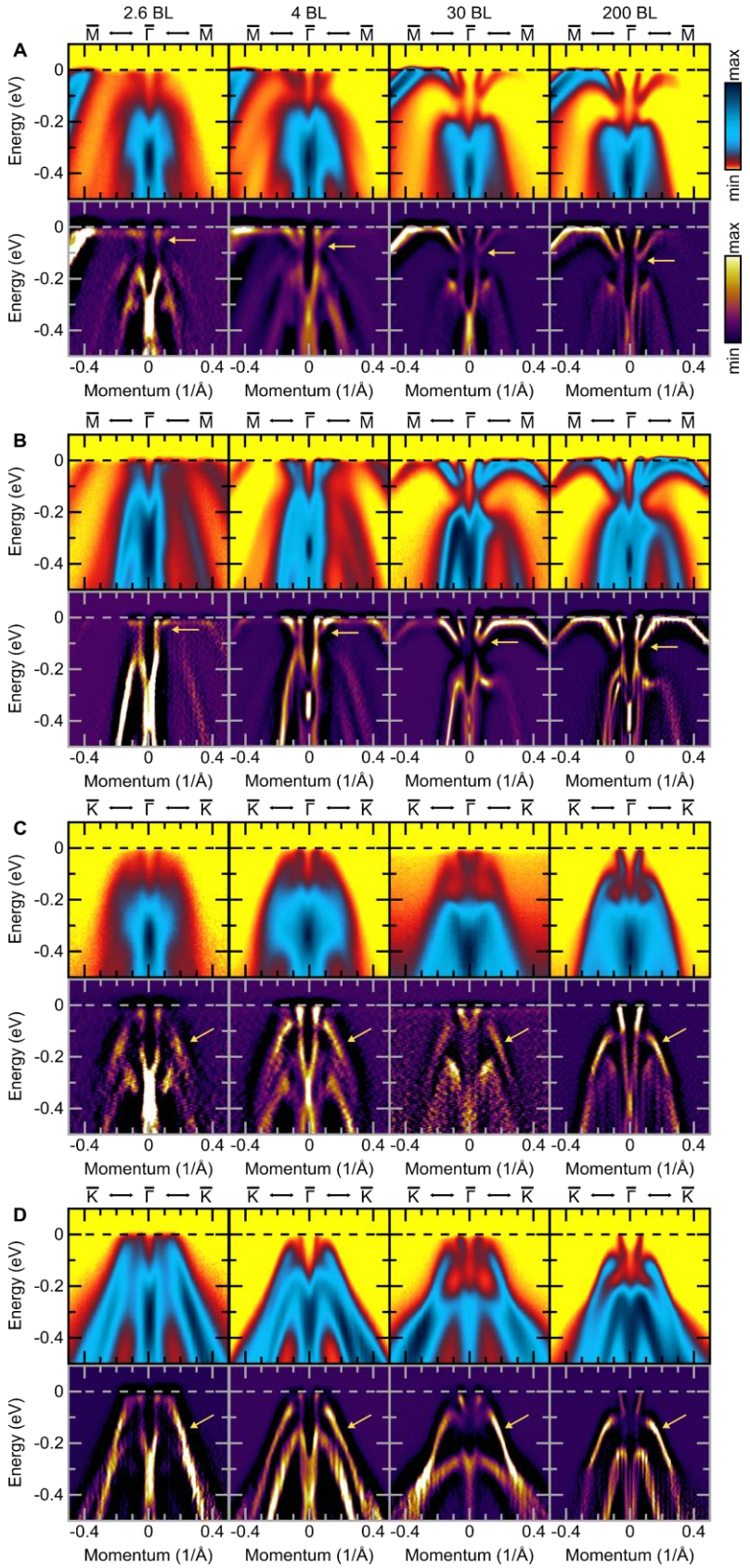

Figure 5.8. ARPES spectra of Bi films near $\bar{\Gamma}$, highlighting the surface state band energy shift. ARPES images of the raw spectra (top panels) and two-dimensional curvature plots (bottom panels), enhancing the dispersive band features. (**A** and **B**) $\bar{M} - \bar{\Gamma} - \bar{M}$ and (**C** and **D**) $\bar{K} - \bar{\Gamma} - \bar{K}$ cuts collected at an incident photon energy (**A** and **C**) $h\nu$ = 37.5 eV and (**B** and **D**) $h\nu$ = 20 eV. In (**A** and **B**) the surface state band minimum energy for each film thickness is highlighted with an arrow. In (**C** and **D**) the change in the surface state band dispersion to a more linear-like E-k dispersion is highlighted with an arrow. Figure reprinted with permission from [221].

In Figure 5.8, high-resolution photoemission scans near $\bar{\Gamma}$ are collected at 20 and 37.5 eV photon energies, which should be close to the bulk Γ and T points, respectively, assuming an inner potential of 6-10 eV. No surface state dispersion is observed as a function of photon energy, yet the scans collected at 30 – 40 eV show a higher surface state cross-section and are more bulk sensitive (i.e., show the 3-fold symmetry near $\bar{M}$) than scans collected at 20 eV. The surface state energy minimum in the $\bar{M} - \bar{\Gamma}$ direction in Figure 5.8A-B is monitored as a function of film thickness, showing a shift towards the Fermi level with decreasing film thickness. Moreover, as the film thickness decreases, the bottom surface state band along $\bar{K} - \bar{\Gamma}$ evolves into a more linear-like dispersion. No additional surface states (from the Bi-InSb interface) are observed in the $\bar{K} - \bar{\Gamma}$ direction for any of the films thicker than 1.3 BL.

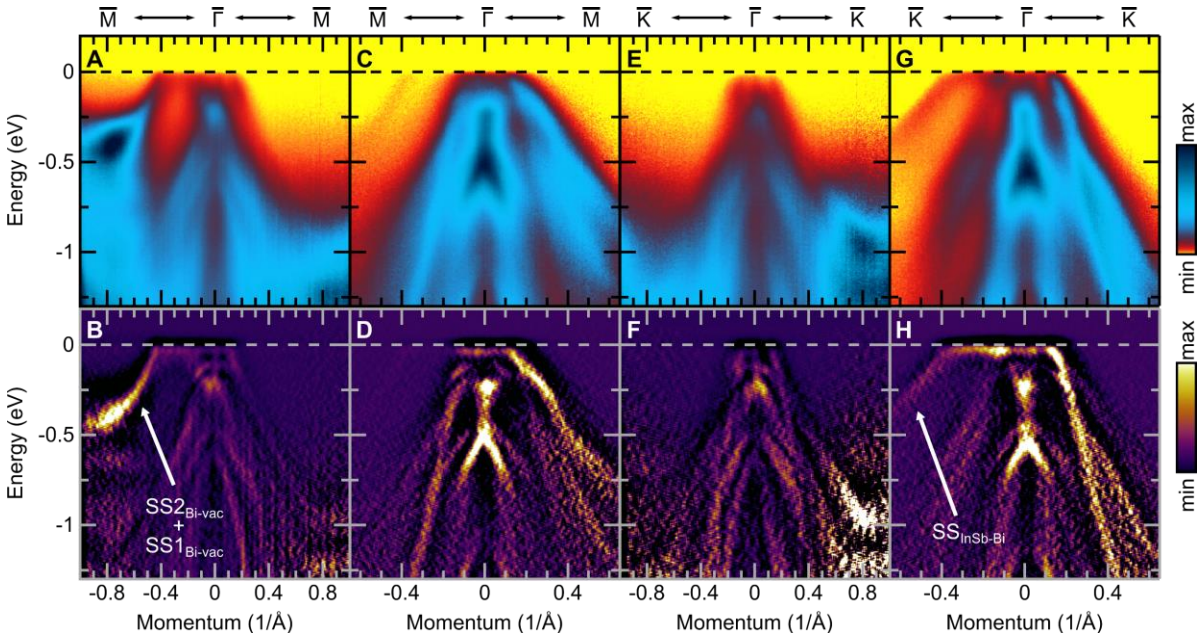

Figure 5.9. ARPES spectra of a 1.3 BL thick Bi film. ARPES images of the raw spectra (top panel) and two-dimensional curvature plots (bottom panel) enhancing the dispersive band features. (**A-D**) $\bar{M} - \bar{\Gamma} - \bar{M}$ cuts collected at a photon energy of (**A-B**) *hv* = 37.5 eV and (**C-D**) *hv* = 20 eV. (**E-H**) $\bar{K} - \bar{\Gamma} - \bar{K}$ cuts collected at photon a energy of **(E-F**) *hv* = 37.5 eV and (**G-H**) *hv* = 20 eV. The two surface states (indistinguishable due to their overlap) at the Bi-vacuum interface are highlighted in (**B**). The surface state originating at the Bi-InSb interface is highlighted in (**H**). Figure reprinted with permission from [221].

ARPES spectra of a 1.3 BL thick Bi film in Figure 5.9 show no evidence of InSb bulk or surface bands (see Figure 5.6) in any of the cuts along the $\bar{M}-\bar{\Gamma}-\bar{M}$ or $\bar{K}-\bar{\Gamma}-\bar{K}$ directions, in contrast to the 1 BL Bi films grown on Bi_2Te_3 showing strong hybridization between the film and the underlying substrate [86,89]. While the bands are slightly more diffuse due to the absence of long-range order in ~ 1 BL films (Figure 5.2F), we observe the Bi-vacuum surface states crossing the Fermi level along $\bar{M}-\bar{\Gamma}-\bar{M}$, similar to thicker films. Along $\bar{K}-\bar{\Gamma}-\bar{K}$ in Figure 5.9(G-H) we see an additional surface state band which we suspect originates at the Bi-InSb interface and was also predicted by our DFT calculations.

5.3.2 First-principles calculations

The DFT calculations in this chapter were conducted by Muhammad Zubair under the supervision of Anderson Janotti at the University of Delaware. We investigated the electronic structure of Bi thin films with DFT-based first-principles calculations with the projector augmented wave (PAW) method as implemented in the VASP code [200,201]. The generalized gradient approximation (GGA) of Perdew-Burke-Ernzerhof (PBE) for the exchange-correlation functional was used [238], including spin-orbit coupling as implemented in the VASP code. We used PAW potentials for Bi with five valence electrons, $6s^2 6p^3$, three valence electrons for In, $5s^2 5p^1$, and five valence electrons for Sb, $5s^2 5p^3$. For convergence of the electronic self-consistent calculations, a total energy difference criterion was defined as 10^{-6} eV. A cutoff energy of 500 eV is used in the plane wave basis set, and a Γ-centered 8×8×1 k-point mesh was employed in the slab calculations. All the band structures were plotted using the PyProcar package [239].

Freestanding Bi layers and Bi/InSb structures were modeled with varying numbers of Bi BLs, from 1 to 6 BL. The lattice parameter of the 1-6 BL freestanding Bi films in Figure 5.10C is fixed to the in-plane relaxed lattice parameter of bulk Bi: $a_{Bi,fixed}^{freestanding} = 4.523$ Å. To study the effect of Bi ultrathin films on an InSb substrate, we modeled the same varying number of Bi BLs on a 2-unit cell thick InSb (111)B slab with a vacuum thickness of 15 Å. The top surface of the InSb (111) slab (B face) was an unreconstructed Sb-polar layer, and the In atoms at the bottom surface (A face) were passivated with hydrogen with a 5/4 fractional charge to fulfill 2 electrons per bond. The structures are relaxed vertically while keeping the in-plane lattice parameter fixed. The Bi/InSb structures with varying Bi layer thicknesses were constrained to the underlying InSb substrate lattice parameter $a_{Bi,fixed}^{Bi/InSb} = a_{[110]}^{InSb} = 4.628$ Å, shown in Figure 5.10D.

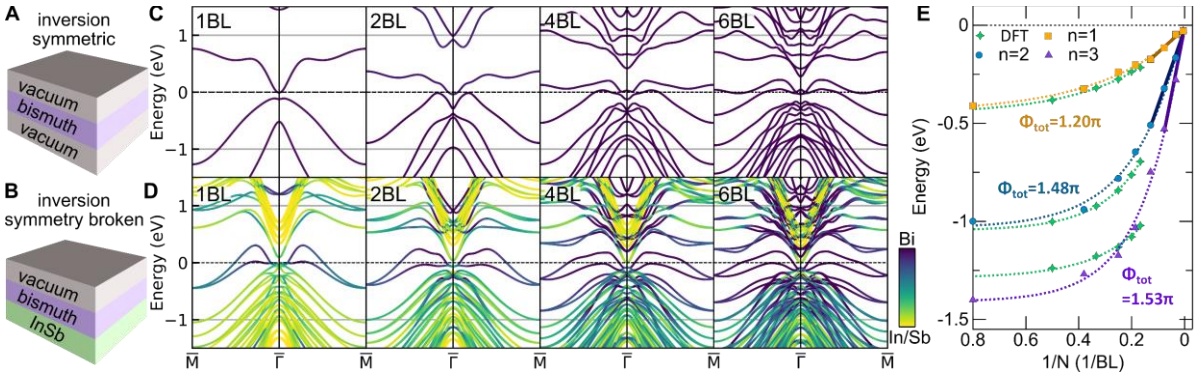

Figure 5.10. Effect of inversion symmetry breaking in ultrathin Bi films. Schematics of representative stacks for (**A**) a freestanding film preserving inversion symmetry and (**B**) a film with broken inversion symmetry. DFT calculations along $\bar{M} - \bar{\Gamma} - \bar{M}$ for varying ultrathin film thicknesses for (**C**) the freestanding Bi slab in (**A**) and (**D**) the film with broken inversion symmetry in (**B**). In (**D**), all states with more than 60% of their spectral weight in the Bi film are marked in purple, and states with 0% of their weight in the Bi film (originating from the InSb layer) are marked in yellow. (**E**) DFT (green) and ARPES (yellow, blue, purple) quantum-well state energy position at $\bar{M}$ vs inverse film thickness, 1/N. The full solid lines are linear fits used for analyzing the total phase shift, and the dotted lines are drawn as guides for the eye. Figure reprinted with permission from [221].

In order to gain more insight into the electronic and structural modifications of the heteroepitaxial structure, we calculate (i) the bulk electronic structure of Bi and InSb, (ii) the band structure calculations for fully relaxed in-plane freestanding Bi and Bi/InSb, (iii) the top

and bottom bilayer-resolved calculations for trivial and nontrivial band structures, and (iv) the stacking arrangement of Bi bilayers with respect to InSb.

We investigated the electronic structure of bulk InSb (see Figure 5.6B) using the screened hybrid functional of Heyd, Scuseria, and Ernzerhof (HSE06) [198,199] with 25% of exact exchange and accounting for spin-orbit coupling. A Γ-centered 6 × 6 × 6 k-point mesh was employed in the InSb bulk band structure calculations to optimize the lattice parameters and the self-energy. The calculations for bulk Bi in Figure 5.1A were performed using a primitive rhombohedral cell with 2 atoms and a Γ-centered 12×12×12 k-point mesh. The optimized lattice parameters of the primitive rhombohedral cell correspond to an in-plane lattice parameter $a_{Bi}^{bulk} = 4.523$ Å and an out-of-plane lattice parameter $c_{Bi}^{bulk} = 3(d_{vdW} + d_{BL}) = 11.75$ Å for the conventional hexagonal cell containing 6 atoms (where the interlayer vdW-like gap is: $d_{vdW} = 2.308$ Å and the intralayer BL height is: $d_{BL} = 1.609$ Å).

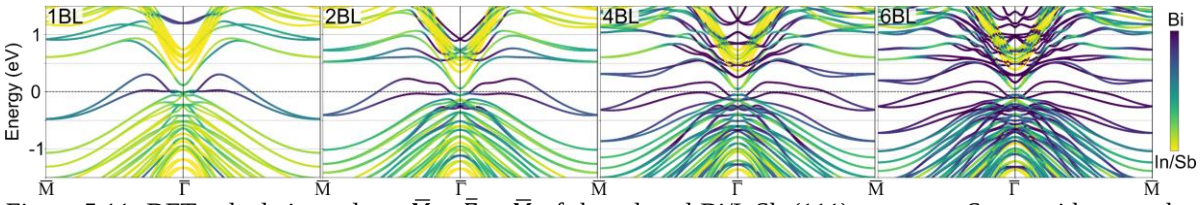

Figure 5.11. DFT calculations along $\bar{M} - \bar{\Gamma} - \bar{M}$ of the relaxed Bi/InSb (111) structure. States with more than 60% of their weight in the Bi film are marked in purple, and states with 0% of their weight in the Bi film (originating from the InSb layer) are marked in yellow. Figure reprinted with permission from [221].

Band structure calculations of freestanding Bi ultrathin films with a relaxed in-plane lattice parameter, present a decrease in the lattice parameter as the film thickness decreases: $a_{Bi,relaxed}^{freestanding} = 4.264, 4.402, 4.441, 4.463, 4.475,$ and 4.484 Å for 1, 2, 3, 4, 5, and 6 BL thick films, respectively. This contraction in the lattice parameter for the freestanding film is consistent with earlier studies of ultrathin Bi films [233]. To confirm strong interfacial bonding, we also let the in-plane lattice parameter of the Bi/InSb films relax (presented in Figure 5.11). The in-plane relaxed lattice parameter of the Bi films on InSb gradually decreases

(elastically, i.e., without introducing dislocations) , approaching the Bi bulk lattice parameter with increasing film thickness: $a_{Bi,relaxed}^{\frac{Bi}{InSb}} = 4.603,\ 4.607, 4.597, 4.592, 4.588, 4.583$ Å for 1-6 BL thick films, respectively. The band structure of the relaxed Bi/InSb films is very similar to the in-plane-constrained structures in Figure 5.10B when comparing band dispersion and quantum-well energies at $\bar{M}$ (within a 20 meV energy difference). Thus, the $\mathbb{Z}_2$ trivial topological band assignment is not heavily dependent on the relaxed/strained ranges for ultrathin films of Bi/InSb.

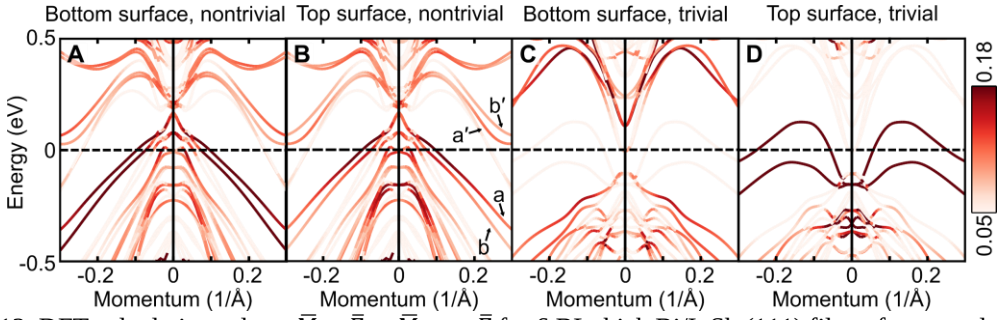

Figure 5.12. DFT calculations along $\bar{M} - \bar{\Gamma} - \bar{M}$ near $\bar{\Gamma}$ for 6 BL thick Bi/InSb (111) films, for states localized at the top and bottom bilayers of trivial and nontrivial band structures. The color scheme depicts the fraction of localization of a state at each surface, where the bottom bilayer in the Bi film is interfaced with InSb, and the top bilayer is at the film-vacuum interface. (**A** and **B**) The Bi/InSb band structure with the c-axis strained by 15% is predicted to have a $\mathbb{Z}_2$ nontrivial band topology. (**C** and **D**) The Bi/InSb band structure without strain in the c-axis, with a trivial $\mathbb{Z}_2$ band topology, the same structure as shown in Figure 5.10D only for a narrower *k* range. (**A** and **C**) Bottom bilayer-resolved bands and (**B** and **D**) top bilayer-resolved bands. The surface state pairs for each interface in the nontrivial band structure are marked with letters (a and a′, b and b′). Figure reprinted with permission from [221].

We have also investigated bilayer-resolved DFT calculations for the topological trivial and nontrivial cases of the Bi/InSb structures in Figure 5.12 to highlight the difference in the intensity of bands originating from the top and bottom layers in inversion asymmetric films based on band topology. This treatment follows earlier detailed studies performed on other inversion asymmetric structures [73,222,240]. To accurately determine the layer-resolved band origin, we have focused on the region near the surface Brillouin zone center due to the higher localization of surface state bands and their reduced penetration into the film bulk [95].

In both cases, the Bi film has the same in-plane lattice constant fixed to the computed InSb lattice parameter of $a_{Bi,fixed}^{Bi/InSb} = a_{[110]}^{InSb} = 4.628$ Å, and the same Bi-InSb interfacial distance. The Bi film with a trivial band structure has an out-of-plane lattice constant of $c_{Bi}^{bulk} = 11.709$ Å and the $\mathbb{Z}_2$ nontrivial band topology was modeled by fixing the out-of-plane lattice parameter to a relatively high value of $c_{Bi}^{nontrivial} = 1.15 \times c_{Bi}^{bulk} = 13.465$ Å to ensure a transition to a $\mathbb{Z}_2$ nontrivial band topology based on earlier reports modeling the inversion gap at L [62,222,241].

Surface states from opposite interfaces will still leak to the adjacent interface at a thickness of 6 BL, however their origin can be distinguished based on the relative changes in band localization. In the $\mathbb{Z}_2$ nontrivial case, Figure 5.12(A and B), we observe a strong intensity of two surface state pairs labeled (i) a and a′ and (ii) b and b′. A third pair of bands with weaker intensities was observed to cross the Fermi level near $k \sim 0.25\ 1/\text{Å}$ and was confirmed to have In/Sb atom contributions and was therefore assumed to be an InSb-related surface state. The pairs a and a′ correspond to states localized at the upper surface, and b and b′ to states localized at the bottom bilayer. Each pair is expected to gap out at $\bar{M}$, though bands a and b, and bands a′ and b′ will each meet at $\bar{M}$ as discussed at length in [222]. In the trivial band structure case in Figure 5.12(C and D), we see only one pair of surface states intersecting the Fermi level in the top bilayer (Figure 5.12D). The bottom bilayer in Figure 5.12C shows no significant contributions from those surface states. The surface states at the top bilayer are confirmed to cross at $\bar{M}$, as shown in Figure 5.10D.

The arrangement of the Bi atom positions on top of the InSb slab was studied via HSE calculations, showing only minor energy differences (ΔE) between three InSb-Bi stackings in Figure 5.13: C-A (ΔE=0 meV), C-B (ΔE=8.62 meV), and C-C (ΔE=5.74 meV), with the InSb

substrate following the conventional face-centered cubic A-B-C-A-B-C stacking. In the C-A stacking, the first Bi monolayer (lower plane of the buckled BL) lies vertically above the last layer of Sb atoms in the InSb slab. In the C-C stacking, that monolayer lies above the last layer of In atoms in the InSb slab. We present the DFT calculations performed for the C-A stackings, which agree better with the ARPES-measured binding energy scaling of quantum-well states with film thickness shown in Figure 5.10E.

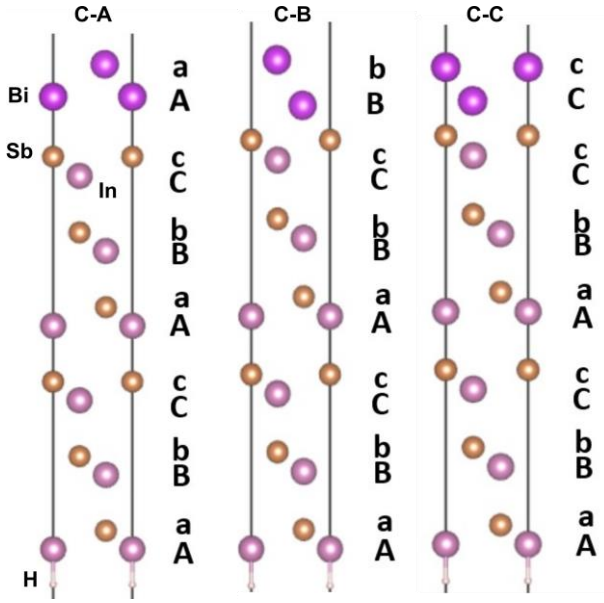

Figure 5.13. Bi-InSb stacking arrangements studied in DFT calculations.

5.3.3 Inversion symmetry breaking

In Figure 5.4(B-E), we follow the evolution of the surface states (SS1 and SS2) and quantum-well states as a function of film thickness. Contrary to earlier ARPES measurement reports for Bi (111) grown on any other substrate, such as Si(111) [64], Ge (111) [72], or Bi_2Te_3 (111) [87,89], we observe a distinct surface state band degeneracy at the $\bar{M}$ point, consistent with the trivial surface state assignment of Bi (Figure 5.1D) and indicative of the surface state bands avoiding crosstalk between the top and bottom surfaces from $\bar{\Gamma}$ to $\bar{M}$. One-

dimensional edge states [242] are ruled out as we do not observe a similar dispersion along $\bar{\Gamma} - \bar{K}$. We further trace the separation between the Fermi wave vectors of the surface states (highlighted in arrows in Figure 5.4(C and D)) and observe a decrease in the surface state separation as the film thickness decreases.

To elucidate the origin of the surface state crossing, we perform DFT calculations for two possible Bi film structures with thicknesses varying from 1 to 6 BLs: (i) an inversion-symmetric freestanding Bi slab (Figure 5.10A) without any surface terminations and (ii) a Bi film on an InSb slab (Figure 5.10B). Our band structure calculations for freestanding Bi layers in Figure 5.10C are consistent with earlier studies [92,233], predicting a semimetal to semiconductor transition for the thinnest 1 BL thick film and two surface states gapped at the $\bar{M}$ point. On the other hand, the Bi/InSb stack in Figure 5.10D shows a surface state degeneracy at the $\bar{M}$ point and an increasing separation in the surface state Fermi wave vectors with film thickness. These results for the Bi/InSb (111)B structure calculations agree with our experimental observations in Figure 5.4(B and C) and Figure 5.5.

The surface state crossing behavior in thin films can be explained by arguing inversion symmetry breaking due to strong Bi-InSb interfacial bonding. Bi films grown on other substrates have not exhibited this band degeneracy due to weak vdW-like interactions at the film-substrate interface [77]. Several observations support the existence of strong Bi-InSb bonding. First, we note the epitaxial stabilization of ultrathin Bi in the (111) orientation on InSb for films as thin as 1 BL in Figure 5.2F, and the formation of a unique fractal structure which requires strong Bi-InSb bonding [229]. Moreover, the nucleation of tensile-strained and azimuthally aligned Bi films [231] to the underlying InSb substrate suggests that the bonding energy initially surpasses the elastic energy later gained when the film relaxes. Finally,

ultraviolet photoemission measurements reveal a shift in both the In 4*d* and Sb 4*d* core levels upon Bi deposition in Figure 5.7, indicating the formation of Bi-Sb bonds and Fermi level pinning near the InSb valence band. No In or Sb core levels were observed for films thicker than 5.4 BL, confirming layer-by-layer deposition and large-area uniform coverage of the ultrathin films.

According to earlier predictions, freestanding Bi films subjected to tensile strain should undergo a semimetal to semiconducting transition resulting in a valence-band edge displaced to higher binding energies and a lowered surface state minima at the $\bar{\Gamma}$ point [62,69,87,89,92,233]. However, our Bi/InSb structure calculations show that the surface state crossing at $\bar{\Gamma}$ (at the binding energy range of 0-0.1 eV) should move closer to the Fermi level as the film thickness decreases, both in Bi films that are tensile strained to the underlying InSb structure (Figure 5.10D) and Bi films that relax above the InSb slab. ARPES data in Figure 5.8 show that the surface state crossing energy approaches the Fermi level as the film thickness decreases. A similar trend was observed for ultrathin films of Sb/InSb(111)A [240]. Thus, film-substrate interactions at the few BL limit could be driving this energy shift.

Another property affected by inversion-symmetry breaking in ultrathin Bi films is the predicted bandgap opening in a 1 BL Bi film [92,243]. In our DFT calculations (Figure 5.10D), the surface states for a 1 BL thick film on InSb are predicted to cross the Fermi level, leading to metallic transport. Therefore, any edge transport channel will coexist with surface state conduction. Our DFT calculation is consistent with ARPES measurements of a 1.3 BL thick film (Figure 5.9), showing the surface states crossing the Fermi level twice along $\bar{\Gamma} - \bar{M}$.

To understand the nature of bonding between Bi and InSb and whether biaxial strain could influence our topological phase assignment, we examined the degree of in-plane relaxation

predicted by DFT calculations (Figure 5.11) and compared the lattice parameters to experimental values [231]. The in-plane relaxed Bi/InSb structure reproduces the experimental trend of early film relaxation starting from 2 BL thick films (Figure 5.2G) [231] and shows no significant change in the surface state dispersion or quantum-well energies, therefore our band assignment applies to Bi films with biaxial strain ranging from 0-0.8% tensile strain. By investigating the bilayer localization of the surface states in DFT calculations along $\bar{\Gamma} - \bar{M}$ (Figure 5.12) we also demonstrate that for a $\mathbb{Z}_2$ trivial Bi film, the surface states are heavily weighted only at the film-vacuum surface and have diminished presence at the InSb interface. Conversely, in a modeled $\mathbb{Z}_2$ nontrivial film we have shown that the surface states at the top and bottom interfaces remain robust against substrate perturbations (Figure 5.12).

5.3.4 Phase accumulation model

Next, we analyzed the extent of film-substrate band hybridization and the degree of quantum confinement in the Bi films. The weighted atom-resolved bands in Figure 5.10D show no significant mixing between the In/Sb- and Bi-derived bands. The quantum-well states in Figure 5.4E and Figure 5.5 observed at $\bar{M}$ originate due to the quantization of the bulk band along the X-L direction, and are analyzed using a phase accumulation model [64,69,72]. For additional information and equations, please see Chapter 2.2.1. At a thickness of 200 BL, quantum-well states are not observed in Figure 5.4E due to the small energy spacing, but thinner films display a larger quantum-well state energy separation with decreasing film thickness. The binding energies at $\bar{M}$ of the top three quantum-well bands (n=1 the surface state crossing point and n=2,3 the following two quantum-well states below) in the DFT

calculations and ARPES measurements for varying Bi film thicknesses (N) are compared in Figure 5.4E, showing excellent agreement.

Along the X-L path, the $E(k_z)$ band disperses nearly linearly up to a 1.5 eV binding energy (see Figure 5.1); therefore, a linear approximation $E = \alpha k_z + \beta$ was suggested [72] to estimate the dispersion relation. To find α, we extract k_z by linearly interpolating multiple binding energies in Table 5.1. $\alpha = 3.85\ eV$Å. We eventually arrive at:

$$E \propto 0.487[2\pi(n-1) - \phi_{tot}]\frac{1}{N}$$

Table 5.1. DFT-calculated and ARPES-extracted binding energies of quantum-well states n=1,2,3 at $\bar{M}$ for the Bi films

# of DFT calculated bilayers	**Binding Energy (eV)**		
	n=1	n=2	n=3
1	-0.442	-1.047	-1.291
2	-0.381	-1.002	-1.239
3	-0.323	-0.923	-1.178
4	-0.277	-0.842	-1.132
5	-0.253	-0.763	-1.080
6	-0.214	-0.696	-1.022
# of ARPES measured bilayers			
1.25	-0.412	-1.00	-1.4
2.63	-0.324	-0.940	-1.27
4	-0.24	-0.782	-1.175
5.38	-0.203	-0.647	-1.034
7.87	-0.175	-0.510	-0.750
13	-0.116	-0.323	-0.529
30	-0.049	-0.166	-0.280
200	-0.03	-0.03	-0.03

For films thicker than 10 BLs, a linear-like region in E for band energy vs. inverse film thickness describes the expected *E*-k_z bulk-like film dispersion [72]. Ultrathin Bi films with less than 10 BL do not obey the linear relationship $E \propto \frac{1}{N}$, thus indicating a deviation from bulk-like dispersion along the X-L, suggesting a transition to 2D-like behavior in ultrathin films. From the linear slopes in Figure 5.10E, we extract the total phase shift, Φ_{tot}, obtained for each quantum number:

$$\phi_{tot}^{n=1} = 1.20\pi, \qquad \phi_{tot}^{n=2} = 1.48\pi\,, \qquad \phi_{tot}^{n=3} = 1.53\pi$$

The vacuum phase $\phi_{Bi-vacuum}$ is calculated using the Wentzel, Kramers, and Brillouin (WKB) approximation for a pure image potential [132] assuming the film's work function is 4.34 eV [244]. Therefore, near the Fermi level at a binding energy E = −0.15 eV: $\phi_{Bi-vacuum} = -0.13\ eV$, and the phase shift at the Bi-InSb interface is:

$$\phi_{Bi-InSb}^{n=1} = 1.33\pi, \qquad \phi_{Bi-InSb}^{n=2} = 1.61\pi\,, \qquad \phi_{Bi-InSb}^{n=3} = 1.66\pi$$

The phase shift calculated for the surface state Bi band *n*=1 is close to the value reported for Bi films grown on Si [64], indicating a similar confining potential for the top surface state. For the *n*=2,3 quantum-well states, a less confining phase shift is measured. This suggests a gradual increase in the degree of spilling of the quantum-well state electron density into the underlying InSb substrate for higher quantum numbers.

5.4 Summary

In conclusion, we report the growth and evolution of surface state dispersion for large-area, single-domain ultrathin films of Bi (111) synthesized on InSb (111)B. We find that strong film-substrate bonds stabilize the ultrathin Bi films in the (111) orientation, offering a new route for the epitaxial growth and integration of other related topological systems, such as compressive strained Bi films and $Bi_{1-x}Sb_x$ 2D layers on insulating III-V substrates. For the first time in Bi films, we observe a surface state crossing at the $\bar{M}$ point, a signature of inversion symmetry-breaking in the $\mathbb{Z}_2$ topological trivial phase. We studied the Bi film quantum-well potential through a phase accumulation model and showed a significant increase in 2D-like behavior for films thinner than 10 BL. Contrary to previous predictions of confinement- [92] or strain-induced [241] semimetal to semiconductor transition in freestanding Bi films, we find

that for inversion-symmetry broken films the metallic surface states cross the Fermi level for all thicknesses down to 1 BL, characterizing a topologically trivial phase.

Our work demonstrates experimentally the possibility of tailoring topological and trivial surface states in group-V ultrathin 2D layers through heteroepitaxial interfaces. Despite numerous theoretical studies on the surface chemistry of buckled Bi films [222,223,245] and other elemental 2D materials [246], there are still few experimental reports on inorganic or molecular functionalization. Future attempts to control surface terminations in 2D materials through overlayer growth could aid in band structure engineering of inversion-symmetric structures and identifying topological phases and their transport signatures in inversion-symmetric / a-symmetric films. A wide range of possibilities is now open for exploring wafer-scale ultrathin $Bi/Bi_{1-x}Sb_x$ films of high crystalline quality for topological edge-transport studies and electronic and optoelectronic device applications.

6 Growth of LuPtBi films

6.1 Introduction

The half-Heusler compound LuPtBi belongs to a unique group of superconductors with a topologically non-trivial band structure and very low carrier densities (<10^{20} cm^{-3}). Given the semimetallic nature of LuPtBi, the phase transition temperature Tc of ≈ 1 K cannot be explained within the Bardeen-Cooper-Schrieffer theory framework [247,248]. Due to strong spin-orbit coupling and broken inversion symmetry in LuPtBi (Figure 6.1A), new mixed pairing states beyond the singlet s wave (J = 0) and triplet p wave (J = 1) are possible [249]. In addition to unconventional pairing states, the strong band inversion found in LuPtBi could suggest three-dimensional (3D) topological superconducting behavior [249]. Topological superconductivity can be thought of as the combination of a topological insulator and a superconductor. Unlike 1D/2D systems, in which proximity-induced topological superconductivity is engineered artificially, 3D topological superconductivity is intrinsic and thus highly desirable.

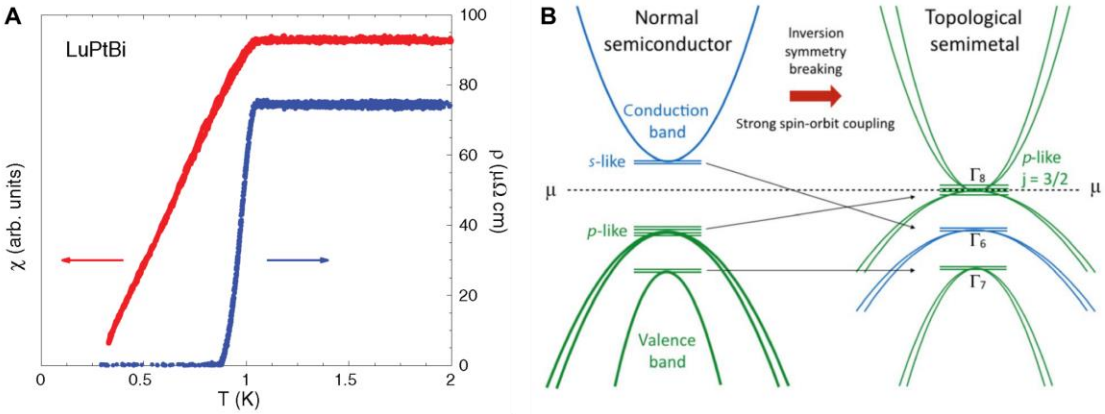

Figure 6.1. (**A**) Superconducting phase transition observed in both resistivity and magnetic susceptibility in bulk LuPtBi crystals, occurring at T_c = 1K. (**B**) Strong spin-orbit coupling in high Z half-Heuslers pushes the s-like band below the chemical potential energy and produces a topological semimetal, which retains the spin $^3/_2$ character of the original p-like band. (**A**) Adapted from [249] and (**B**) adapted from [250].

Experimental evidence of mixed even and odd pairing was shown for REPdBi (RE: rare earth) ([251] LuPtBi [249] and YPtBi [250,252]. Since the chemical potential is situated in the p-like Γ_8 band for many of these Heulslers, the total angular momentum of conduction electrons is j = 3/2, and pairing states with a total angular momentum beyond the singlet s wave (J = 0) and triplet p wave (J = 1) are possible. Finally, the low carrier density in Heusler semimetals also presents these compounds as highly promising tunable superconductors.

Synthesizing LuPtBi in thin film form is challenging. Compared to III-V compounds, epitaxial Heusler films are difficult to synthesize due to narrow adsorption-controlled growth windows and precise flux control required to obtain stoichiometric transition metals [110]. Unlike Sb-based half-Heuslers grown by MBE [104,253], Bismuth-containing half-Heuslers have additional unique growth complications: (i) low Bi atom incorporation [103,254–256], (ii) a lack of lattice-matched substrates, and (iii) narrower chemical potential stability fields (i.e., lower point-defect tolerance) [257].

Achieving high Bi incorporation in thin films is a common issue found in III-V-Bi ternary growth [258] and bismuthide half-Heusler films [103,254–256]. In III-Vs, Bi alloying is limited to only a few percent before phase separation occurs, typically resulting in Bi surface segregation [258]. This behavior is attributed to the weak metal-Bi bonding energy, the large size of the Bi atom, the low melting point (271 ^{o}C), and high vapor pressure of Bi limiting high-temperature growth. Similar evaporation and segregation challenges are also faced in Heusler growth, resulting in reduced carrier mobilities and high carrier concentrations [254].

Compared to conventional semiconducting substrates, bismuthide half-Heuslers have relatively large lattice constants far from group-IV or III-V compounds (Figure 1.7). The substrates closest to Bi-based half Heuslers in lattice matching are InSb (6.479 Å, see Figure

6.2), CdTe (6.481 Å), and sapphire (for *c*-plane Al_2O_3: a=4.765 Å), yet still incur significant lattice mismatch ($|\varepsilon| \geq 1.5\%$). Typical III-V metamorphic buffer layer growth schemes cannot be easily applied to produce lattice-matched buffer layers for a > 6.479 Å, thereby limiting epitaxial strain control.

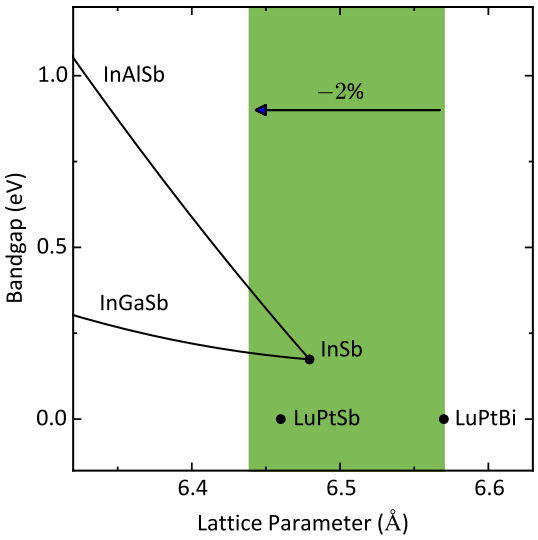

Figure 6.2. Bandgaps and lattice constants of III-V compounds and half-Heusler alloys. The green field shows the composition range of potential buffers falling within a 2% compressive biaxial strain of LuPtBi.

6.2 Growth of LuPtSb and LuPtBi on InSb (111)B

A (3×1) surface of unintentionally doped epi-ready InSb (111)B wafers (Wafer Technology Ltd.) was prepared with atomic hydrogen cleaning for native oxide removal and studied *in vacuo* with RHEED and STM [225]. To hydrogen clean the samples, the samples were heated to 360 °C, as measured by a thermocouple near the sample, and exposed to a chamber pressure of 5×10^{-6} Torr of atomic hydrogen, as measured by an ion gauge in the chamber. The atomic hydrogen was generated by flowing hydrogen gas through a leak valve and into a thermal cracker (Dr. Eberl MBE-Komponenten GmbH) operated at 1700 °C. Following an Sb-soak at growth temperatures (for LuPtSb growths), an Sb-rich (2×2) surface

reconstruction is obtained. The starting (111)B face was selected due to the unreconstructed Sb-polar surface, which was expected to be less reactive with LuPtSb and LuPtBi.

The films were grown in a modified Veeco Gen-II MBE system with a base pressure $<1x10^{-10}$ Torr. Pt:Lu:Sb flux ratios were set to 1:1:1.1-1.3, and Pt:Lu:Bi flux ratios were set to 1:1:1. Nearly stoichiometric conditions were set for Bi-based growths due to the near-unity sticking coefficient at growth temperatures below 320 ^{o}C [259]. The elements Sb, Bi, and Lu were evaporated from effusion cells with a deposition rate of $2x10^{14}$ atoms/cm^{2}min, while Pt was evaporated using an e-beam evaporator. Atomic fluxes were determined by Rutherford backscattering spectrometry measurements of the elemental area atomic density of calibration samples grown on Si. These measurements were then used to calibrate *in situ* beam flux measurements using an ion gauge for Lu, Sb, and Bi and a quartz crystal microbalance for Pt. Surface crystal quality was monitored *in situ* with RHEED. The samples were transferred under vacuum for ARPES and STM measurements and were eventually capped with a 5-nm-thick AlO_x layer deposited by electron-beam evaporation of Al_2O_3 source material to prevent film oxidation when loaded out of ultrahigh-vacuum for *ex situ* characterization. Lattice parameters, film thickness, and crystallinity information were extracted from high-resolution X-ray diffraction.

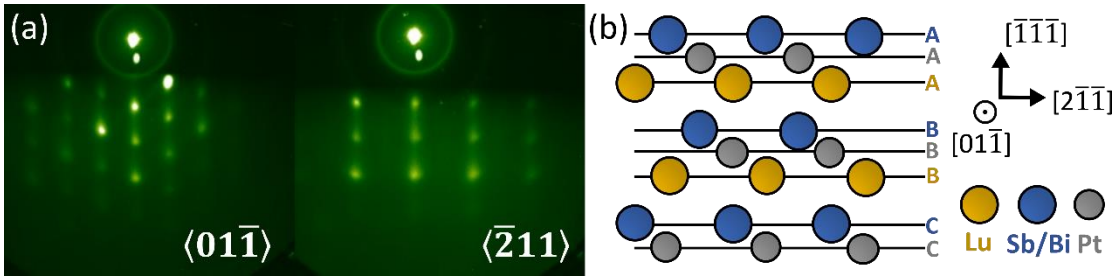

Figure 6.3. (**a**) RHEED 3D diffraction patterns of a 10 unit cell thick (11.4 nm) LuPtBi film deposited on InSb(111)B at 100 ^{o}C. (**b**) Polar stacking of atomic layeres in a (111) oriented half-Heusler film.

3D nucleation was observed via RHEED in Figure 6.3(a) for both LuPSb and LuPtBi films nucleated on InSb (111)B within the first unit cell nucleated, without significant improvement as the film thickness is increased. The 3D growth mode of both LuPtBi and LuPtSb is independent of the InSb (111)B surface reconstruction, studied for Sb-rich (2×2) and Sb-poor (3×1)/ (3×3) surfaces. 3D nucleation was observed at substrate growth temperatures ranging from room temperature to 320 ^{o}C.

While strain energy could drive early relaxation and 3D growth for LuPtBi, it does not explain the early roughening of LuPtSb on InSb (111)B. LuPtSb is only ~0.3% lattice mismatched with respect to InSb (with a lattice parameter of 6.457 Å, see Figure 6.2), and when grown directly on InSb (001) it does not relax for at least a thickness of 10 nm. One possible explanation for the early roughening of {111} oriented LuPtSb/Bi Heuslers is the high surface energy and charge polarity of the {111} planes in the half-Heusler structure [44], see Figure 6.3(b). Instead of forming highly-charged {111} layers of Lu^{3+} and V^{3-}, charge-neutral planes such as the (001) facets have a lower formation energy and would lead to 3D islands. Previous reports of bismuthide Heuslers grown on c-plane sapphire also show a pyramid island-like growth mode leading to high film roughness [254,256,260,261].

In addition to 3D roughening, we also observe phase separation for (111) oriented LuPtBi films, even at low nucleation temperatures of 100 ^{o}C. XRD in Figure 6.4 shows two sets of reflections, corresponding to a hexagonal (0001) oriented Bi film and a Bi-deficient (111) $LuPtBi_{1-x}$ phase. In the XRD θ-2θ survey scan in Figure 6.4 we found no evidence of the formation of the most stable neighboring phases: LuPt, $LuPt_3$, LuBi [257], or any In-Bi phases [262] (see Figure 6.5). Phase separation in LuPtBi is likely driven by surface segregation of Bi due to the low surface energy expected for the vdW-like Bi (111) layers

stabilized by the underlying InSb (111)B substrate. Due to the high adatom mobility of Bi, even low growth temperatures result in phase separation. The challenges faced by (111) oriented LuPtSb/LuPtBi films led us to study (001) LuPtBi synthesis.

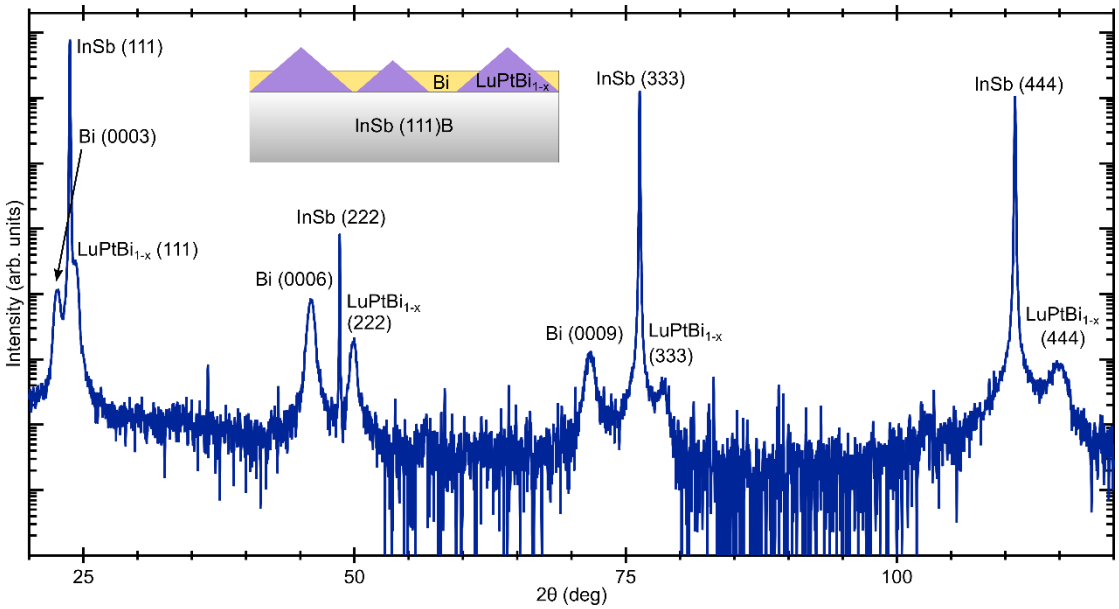

Figure 6.4. Out-of-plane θ-2θ XRD scan for a nominally 10 unit cell thick (11.4nm) LuPtBi film, grown on an InSb (111)B substrate. Inset shows the proposed phase segregation.

6.3 Growth and characterization of LuPtBi (001)

A well-ordered c(8×2) surface of unintentionally doped epi-ready InSb (001) wafers (Wafer Technology Ltd.) was prepared with atomic hydrogen cleaning similar to earlier conditions used for InSb (111)B [225]. Previous studies by S. Patel [259] have shown that LuPtBi films grown on InSb (001) require a LuPtSb barrier layer to mitigate substrate-film reactions resulting in 3D growth and the formation of unintentional $InBi_x$ phases (Figure 6.5).

The small lattice mismatch of LuPtSb with respect to InSb (Figure 6.2) allowed the growth of 10 UCs (6.5 nm) of LuPtSb without any relaxation observed via RHEED (Figure 6.6) or STM (Figure 6.8). Following LuPtSb growth, LuPtBi nucleation was studied at two temperature ranges: room temperature - 180 ^{o}C and 200-300 ^{o}C. Both LuPtBi growth

temperatures produced streaky RHEED patterns suggesting a smooth surface. However, hotter growths led to weaker pattern intensities and the appearance of an additional set of unidentified reflections (not associated with a surface reconstruction). These additional streaks suggest another phase is present and was later confirmed via XRD to originate from an $InBi_x$ phase.

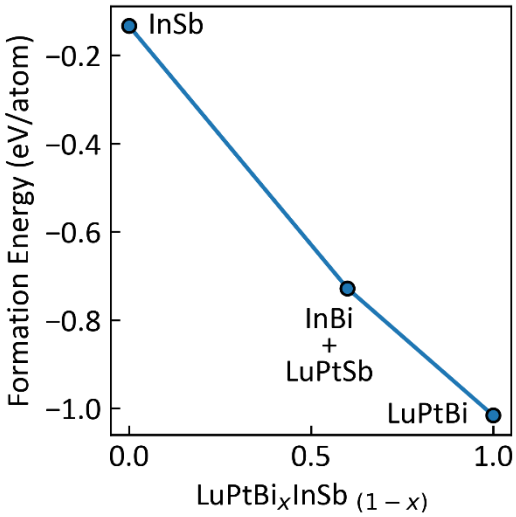

Figure 6.5. Convex hull diagram in the InSb-LuPtBi chemical space. The formation energies are calculated from the Open Quantum Materials Database (OQMD) [263,264].

While InSb-LuPtBi reactions at ~200 ^{o}C should be mitigated by the LuPtSb buffer, bismuth incorporation in the LuPtBi film appears to be reduced at high growth temperatures due to surface segregation of the highly mobile Bi atoms. Surface segregation of Bi could be due to the low surface energy of elemental Bi and is likely exacerbated by a composition-pulling effect [265,266]. The compressive strain induced by the InSb substrate promotes surface phase separation of bismuth in LuPtBi, similar to effects observed in $Ge_{1-x}Sn_x$ alloys grown on Ge [267] and $Ga_{1-x}In_xN$ grown on GaN [266]. Upon cooling below the Bi-InBi eutectic (~ 105 ^{o}C) the excess surface Bi reacts with elemental indium on the surface (present due to wafer bonding) and forms an InBi phase. This mechanism was confirmed by growing on Ga-bonded InSb which did not present the InBi phase (however did suffer from poor quality as Ga is a

known Bi anti-surfactant [268], increasing the interfacial surface energy due to a miscibility gap in the Ga-Bi phase diagram and leading to Bi dewetting).

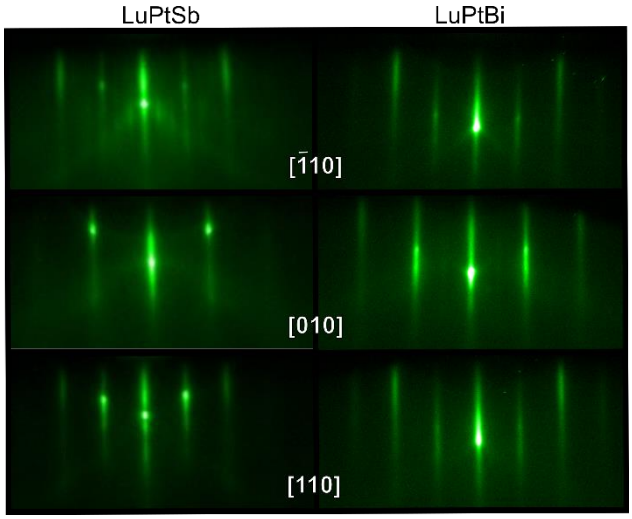

Figure 6.6. RHEED pattern evolution for the underlying (1×3) surface reconstructed LuPtSb (001) layer and the top layer of c(2×2) LuPtBi (001) along different azimuths.

Due to the low Bi incorporation and InBi defect phase forming at higher growth temperatures, room-temperature nucleation was selected for subsequent growths, followed by post-growth annealing at ~260 ^{o}C. RHEED images in Figure 6.6 show a streaky pattern for both LuPtSb and LuPtBi layers, indicating a smooth surface is obtained. The faint c(2×2) surface reconstruction observed for LuPtBi suggests a Bi-rich surface is obtained.

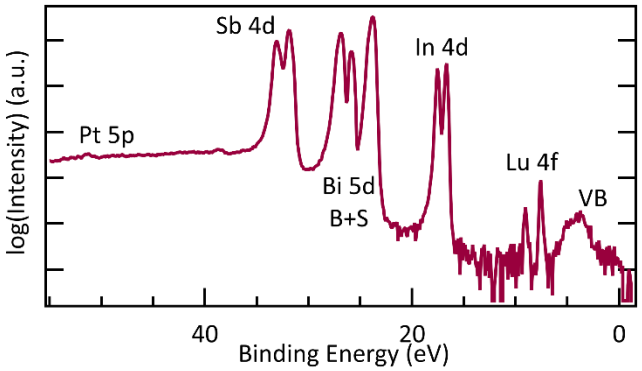

Figure 6.7. UPS scan collected for an *in vacuo* transferred film of 6.5 nm LuPtBi / 6.5 nm LuPtSb / InSb (001) measured at *hv*=100 eV.

In vacuo ultraviolet photoemission spectroscopy (UPS) scans of the LuPtBi film in Figure 6.7 show all core levels from the LuPtBi film, as well as In and Sb core levels. For the Bi 5*d*

core level, both bulk and surface state core levels are seen supporting our hypothesis of a Bi-rich surface. The In and Sb origin is unclear and could be from the underlying LuPtSb and InSb layers or the elemental In used for wafer bonding. Due to the cold growth conditions, the LuPtBi film quality was not high enough to study the electronic band structure with ARPES.

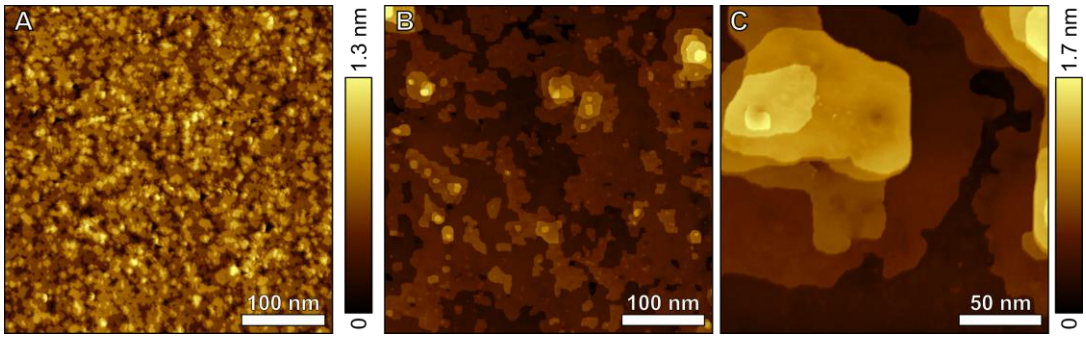

Figure 6.8. STM image of a 6.5 nm LuPtSb/InSb (001) structure measured at (**A**) bias voltage V_b: 0.5 V, current I: 3 nA and (**B-C**) 6.5 nm LuPtBi / 6.5 nm LuPtSb/InSb (001) measured at (**B**) V_b: 1.5 V, I: 5 pA and (**C**) V_b: 1 V, I: 5 pA.

The surface morphology of the films was studied by *in situ* STM. Figure 6.8(A) shows an empty-state STM image of the underlying LuPtSb buffer layer, and the LuPtBi film grown on top in Figure 6.8(B and C). A smooth surface is obtained for both films. The LuPtBi film was found to have a high density of screw dislocations (shown in Figure 6.8(C)) despite appearing unrelaxed in XRD measurements (Figure 6.9). These screw dislocations might be limited to

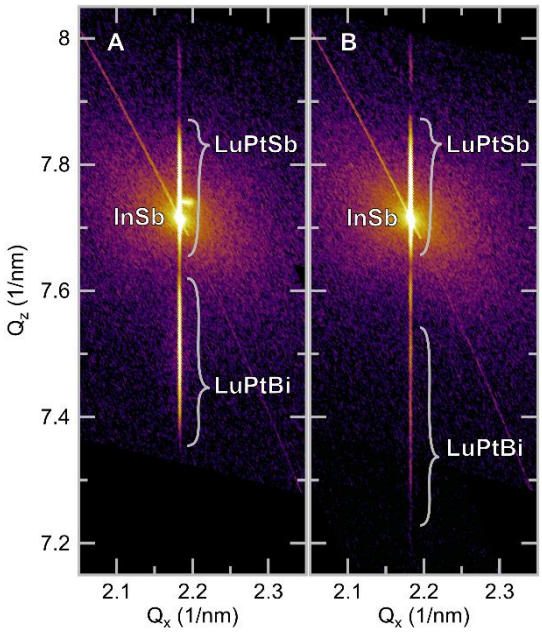

Figure 6.9. Reciprocal space maps of the (115) reflections for (**A**) 6.5 nm LuPtBi / 6.5 nm LuPtSb/InSb (001) and (**B**) 3 nm LuPtBi / 6.5 nm LuPtSb/InSb (001). In both samples all layers appear to be coherently strained.

the top Bi-rich surface, where an ultrathin Bi layer could be weakly bonded to the underlying LuPtBi film. The Bi-rich surface is likely restricted to a few monolayers as we could not see a Bi phase in our XRD scan (Figure 6.10) and our UPS scan showed the Lu and Pt core levels (Figure 6.7).

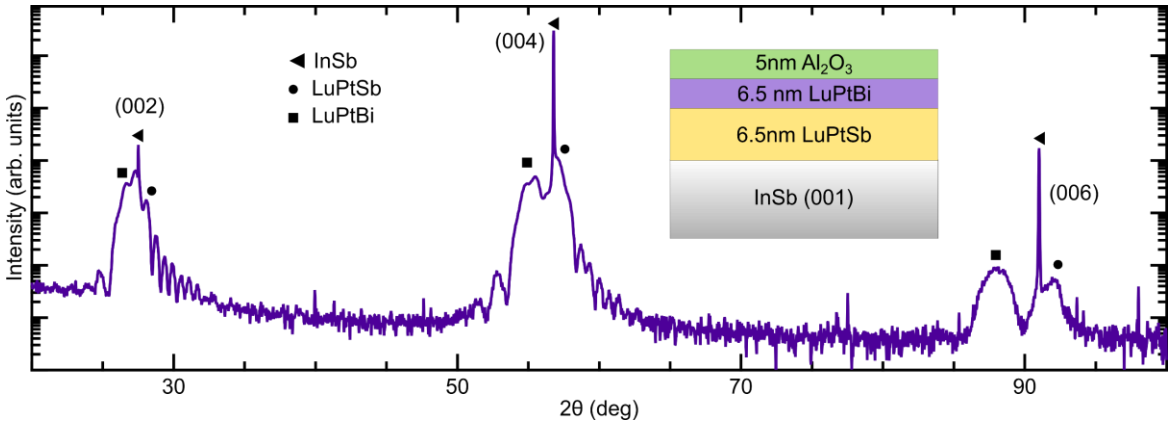

Figure 6.10. *θ-2θ* XRD scan for a 6.5 nm LuPtBi / 6.5 nm LuPtSb/InSb (001) structure showing thickness fringes indicating a sharp interface and absence of impurity phases.

6.4 Summary

In conclusion, we have studied the growth window of the Heusler compound LuPtBi for different growth orientations, (001) and (111), varying the growth temperature from room temperature to 350 ^{O}C, and nucleation interface chemistry. Bismuth-containing Heuslers have additional unique growth complications due to the low bulk incorporation of Bi atoms and lack of lattice-matched substrates. (111) oriented growths of LuPtBi and LuPtSb resulted in 3D films. One potential explanation for the high film roughness for (111) oriented half-Heuslers is the unstable (111) polar growth front. Phase separation from LuPtBi (111) to Bi (0001) and a Bi-deficient phase of $LuPtBi_{1-x}$ was observed.

InSb (001) substrates were pursued as an alternative growth front for LuPtBi films. While (001) LuPtSb can be epitaxially grown directly on InSb (001), LuPtBi (001) films require a barrier layer to mitigate substrate-film reactions forming unintentional $InBi_x$ phases. In addition, low growth temperatures <100 ^{o}C were necessary to ensure bismuth incorporation in LuPtBi, which otherwise would surface segregate at 200 ^{O}C <T_g<300 ^{O}C. Our work shows that InSb substrates do not serve as appropriate templates for bismuthide half-Heusler growth due to two main drawbacks: (1) interfacial reactions between indium and bismuth and (2) compressive strain leading to composition pulling and low Bi incorporation. Cold nucleation on a LuPtSb buffer layer resulted in smooth, coherently strained LuPtBi films with a Bi-rich surface.

7 Conclusions and outlook

In this thesis, we have investigated the relationship between epitaxial growth and electronic properties of three materials systems integrated with III-V compound semiconductors: (1) biaxially strained and lattice-matched GdSb thin films, (2) ultrathin bismuth films, and (3) LuPtBi half-Heusler films.

7.1 Strained and lattice-matched GdSb

In chapters 3 and 4 of the dissertation, we study the evolution of band topology and magnetoresistance in lattice-matched and biaxially strained GdSb (001) epitaxial films using STM, ARPES, DFT, and magnetotransport. First, we achieved high-grade epitaxial GdSb thin films, which allowed us to study the Fermi surface, magnetic ordering, and electrical properties of these GdSb films. We found that lattice-matched GdSb films show a mobility and carrier concentration imbalance, deviating from the commonly assumed compensated charge carrier densities in bulk semimetals showing XMR.

Next, we study the effect of biaxial strain on band topology. Few experimental reports visualize the electronic band structure of strain-tuned topological semimetals, and hardly any rely on epitaxial thin films. We established a clear connection between biaxial strain in GdSb films and the affected band dispersions based on their orbital composition. Biaxial strain in GdSb continuously tunes the electronic structure from a topologically trivial to a nontrivial regime, reducing the gap between the hole and the electron bands dispersing in the [001] direction.

Using a simple tight-binding model accounting for the orbital symmetry of each band, we reproduced trends seen in DFT calculations and ARPES measurements and elucidated the

origin of conduction and valence band shifts. The effect of biaxial strain on carrier compensation and magnetic ordering temperature is also explained based on the modified band structure. Our tight-binding model can be applied to other RE-Vs, alternative rocksalt compounds, and other RE-V-derived compounds such as Heusler alloys. The development of highly-quality GdSb films will have a substantial impact in the field of epitaxial semimetal growth and will serve as a foundation for additional studies aimed at integrating topological semimetals with III-V semiconductors and studying their transport behavior and applications in plasmonics, spintronics, and magnetoresistive devices. Trends in magnetic ordering temperature and the tight binding model developed for strained GdSb can also serve as a stepping stone for characterizing biaxially strained RE-N semiconductor thin films, a promising system for spintronic applications of rock salt nitride metal/semiconductor superlattices [269].

Further work is needed to map strain and thickness-mediated topological phase transitions in RE-V compounds. With their superior epitaxial quality and band inversion point well below the Fermi level, RE-V thin films make an ideal material system for studying topological transitions using ARPES. The conduction and valence band crossing in the nontrivial $\mathbb{Z}_2$ state of GdSb ~0.4 eV below the Fermi level facilitates easier analysis of strain-induced bandwidth changes but limits the contribution of topological surface states to magnetotransport characteristics. Lighter RE-Vs like LaSb, which have a band crossing closer to the Fermi level, are therefore best suited to magnetotransport studies. The biaxial strain required for band inversion in LaSb is also smaller than in GdSb [150]. Moreover, LaSb has the lowest carrier density of all RE-Sb [270], which makes it ideal for studying semimetal to semiconductor quantum size effects at ultrathin scales. A quantum spin Hall insulator phase was recently

predicted to emerge for the thickness range of 3-7 monolayers of LaSb(001) [203]. Future studies could explore the growth and electronic structure of ultrathin LaSb films on closely lattice-matched systems such as InSb.

7.2 Assigning topology in bismuth via heteroepitaxial functionalization

The second part of this dissertation reports the first ARPES investigation conclusively assigning bismuth's topological character to the trivial $\mathbb{Z}_2$ state by studying ultrathin films grown on InSb (111)B. The trivial bulk L gap would then classify Bi as a higher-order topological insulator rather than a strong one, which has remained ambiguous until now. We find that film-substrate interactions lead to inversion symmetry breaking, thereby artificially isolating the top surface layer from the bottom interface. Other 2D films could benefit from this heteroepitaxial termination approach in controlling surface state dispersions and gapping out bands. While there have been numerous computational predictions of band engineering in terminated group-V 2D films, experiments in the field have lagged due to synthesis challenges.

We achieved large-area high-quality bismuth thin films using MBE grown on atomic hydrogen cleaned InSb (111)B surfaces and studied the film surface comprehensively using electron diffraction, STM, and ARPES. Realizing single-crystal low-dimensional materials at a wafer scale and gaining a deep understanding of their basic electronic properties is important for next-generation electronic device applications. Our bismuth films experience epitaxial stabilization promoting layer-by-layer growth of the (111) orientation starting from a thickness of 1 bilayer. This finding allows us to study the predicted semimetal-to-semiconductor transition in ultrathin bismuth and could be used to characterize one-dimensional edge transport behavior in scalable devices.

In our study, we mapped the dispersion of surface states and quantum wells in Bi films, but bulk bands proved more difficult to detect due to their low cross-section in VUV-ARPES measurements. Future low-temperature magnetotransport measurements may reveal changes in the bulk band structure as a function of film strain and thickness. At low temperatures (< 2 K) and high magnetic fields the InSb substrate is expected to undergo a magnetic-field-induced metal-insulator transition [271]. Therefore, magnetotransport signatures such as quantum oscillations and Hall resistance should originate primarily from the Bi thin film.

Moving forward, to access a topological insulating phase one can study compressive strained Bi films or alloyed Bi films. Compressive strained Bi films can be grown on $In_{1-x}Al_xSb$ virtual buffer layers. Due to the vdW-like epitaxial growth mode of bismuth, maintaining compressive strain beyond the ultrathin limit might prove challenging, as evidenced by the early onset of strain relaxation observed for tensile strained Bi films synthesized on InSb(111)B. In addition to accessing a topological phase, growth on alternative substrates such as GaAs, InAs, or GaSb (111) would allow studying the evolution of a soliton network as a function of film strain and interface chemistry. Changing the substrate material will also influence the strength of interface bonds. This will affect the formation of soliton networks and even the degree of inversion symmetry breaking if the interfacial bonds are weak.

Compositional alloying can also be used to access the topological phase of Bi. $Bi_{1-x}Sb_x$ with a concentration of $0.07<x<0.21$ was shown experimentally to lie within a three-dimensional topological insulator regime [5,272]. While ultrathin films of $Bi_{1-x}Sb_x$ in the (111) orientation are challenging to synthesize on Si (111) due to an allotropic transition to the (012) orientation [273], Sb (111) was shown to be stable on InSb (111)B [240]. Therefore, the nucleation of ultrathin $Bi_{1-x}Sb_x$ on InSb (111)B will likely not suffer from the unwanted

orientation transition. Lastly, surface-state dominated transport could be achieved by removing the valence band Fermi level crossing using epitaxial tensile strain through direct growth of $Bi_{1-x}Sb_x$ on InSb (111)B.

7.3 Growth window of LuPtBi thin films

In the third part of this dissertation, the growth parameters of LuPtBi films were explored. Topological half-Heuslers have inverted bands near the Fermi level and could have TSS-dominated transport assuming the bulk bands can be gapped through epitaxial strain. We have studied the growth window of the Heusler compound LuPtBi for different growth orientations, (001) and (111), varying the growth temperature from room temperature to 350 ^{O}C, and nucleation interface chemistry. A suitable growth window could not be identified for (111) oriented LuPtBi, which was affected by 3D nucleation of phase-separated films. Room-temperature nucleation of LuPtBi on a LuPtSb/InSb (001) template produced smooth, coherently strained films. Hotter nucleation of LuPtBi at 200 ^{O}C < T_g < 300 ^{O}C, below the surface desorption temperature of Bi, still resulted in low Bi bulk incorporation due to a composition-pulling effect (where the solid composition is affected by elastic strain resulting in an alloy, or multiple alloy phases, that reduces the lattice mismatch strain energy [266]).

Future work on strained bismuthide half-Heusler thin films should also consider surface kinetics and potential phase segregation, which might impede high-quality thin film growth, a necessary condition for characterization with ARPES and magnetotransport. Exploring other non-reactive substrates that apply tensile strain or are close to lattice-matching conditions is one possible solution, as we have shown that InSb substrates are limited only to low growth temperatures. One potential substrate meeting these conditions is sapphire (a = 4.76 Å, c=12.99

Å) which is +1.2% lattice mismatched from YPtBi [256] and +2.3% mismatched from LuPtBi. Previous reports of half-Heuslers grown on c-plane sapphire show an island-like growth mode leading to high film roughness [254,256,260,261], resulting in thick relaxed films. In order to mitigate 3D growth, other orientations could be studied, such as r-plane or m-plane oriented sapphire, which might promote (001) growth in half Heuslers. Another approach to improving the epitaxial film quality of bismuthide topological Heuslers is through the growth of quaternary systems such as $LuPtBi_{1-x}Sb_x$ and $YPtBi_{1-x}Sb_x$ which should have improved thermodynamic stability and be less prone to defect phase formation.

Bibliography

[1] P. Narang, C. A. C. Garcia, and C. Felser, Nat. Mater. **20**, 293 (2021).
[2] L. Fu, C. L. Kane, and E. J. Mele, Phys. Rev. Lett. **98**, 106803 (2007).
[3] J. E. Moore and L. Balents, Phys. Rev. B - Condens. Matter Mater. Phys. **75**, 3 (2007).
[4] L. Fu and C. L. Kane, Phys. Rev. B **76**, 045302 (2007).
[5] D. Hsieh, D. Qian, L. Wray, Y. Xia, Y. S. Hor, R. J. Cava, and M. Z. Hasan, Nature **452**, 970 (2008).
[6] F. Ortmann, S. Roche, and S. O. Valenzuela, *Topological Insulators* (Wiley, 2015).
[7] J. Hu, S.-Y. Xu, N. Ni, and Z. Mao, Annu. Rev. Mater. Res. **49**, 207 (2019).
[8] I. Vobornik, A. B. Sarkar, L. Zhang, D. W. Boukhvalov, B. Ghosh, L. Piliai, C. Kuo, D. Mondal, J. Fujii, C. S. Lue, M. Vorokhta, H. Xing, L. Wang, A. Agarwal, and A. Politano, Adv. Funct. Mater. **31**, 2106101 (2021).
[9] *Press Release*. *Https://Www.Nobelprize.Org/Prizes/Physics/2016/Press-Release/* (NobelPrize.org, 2023).
[10] Y. Xia, D. Qian, D. Hsieh, L. Wray, A. Pal, H. Lin, A. Bansil, D. Grauer, Y. S. Hor, R. J. Cava, and M. Z. Hasan, Nat. Phys. **5**, 398 (2009).
[11] H. Yang, A. Liang, C. Chen, C. Zhang, N. B. M. Schroeter, and Y. Chen, Nat. Rev. Mater. **3**, 341 (2018).
[12] L. Wu, S. Patankar, T. Morimoto, N. L. Nair, E. Thewalt, A. Little, J. G. Analytis, J. E. Moore, and J. Orenstein, Nat. Phys. **13**, 350 (2017).
[13] H. Inoue, A. Gyenis, Z. Wang, J. Li, S. W. Oh, S. Jiang, N. Ni, B. A. Bernevig, and A. Yazdani, Science **351**, 1184 (2016).
[14] M. Hirschberger, S. Kushwaha, Z. Wang, Q. Gibson, S. Liang, C. A. Belvin, B. A. Bernevig, R. J. Cava, and N. P. Ong, Nat. Mater. **15**, 1161 (2016).
[15] M. G. Vergniory, L. Elcoro, C. Felser, N. Regnault, B. A. Bernevig, and Z. Wang, Nature **566**, 480 (2019).
[16] M. G. Vergniory, B. J. Wieder, L. Elcoro, S. S. P. Parkin, C. Felser, B. A. Bernevig, and N. Regnault, Science **376**, (2022).
[17] L. Šmejkal, T. Jungwirth, and J. Sinova, Phys. Status Solidi - Rapid Res. Lett. **11**, 1700044 (2017).
[18] D.-F. Shao, G. Gurung, S.-H. Zhang, and E. Y. Tsymbal, Phys. Rev. Lett. **122**, 077203 (2019).
[19] Q. Shao, P. Li, L. Liu, H. Yang, S. Fukami, A. Razavi, H. Wu, K. Wang, F. Freimuth, Y. Mokrousov, M. D. Stiles, S. Emori, A. Hoffmann, J. Akerman, K. Roy, J.-P. Wang, S.-H. Yang, K. Garello, and W. Zhang, IEEE Trans. Magn. **57**, 1 (2021).
[20] J. Tian, I. Childres, H. Cao, T. Shen, I. Miotkowski, and Y. P. Chen, Solid State Commun. **191**, 1 (2014).
[21] V. Baltz, A. Manchon, M. Tsoi, T. Moriyama, T. Ono, and Y. Tserkovnyak, Rev. Mod. Phys. **90**, 015005 (2018).
[22] P. Němec, M. Fiebig, T. Kampfrath, and A. V. Kimel, Nat. Phys. **14**, 229 (2018).
[23] T. Matsuda, N. Kanda, T. Higo, N. P. Armitage, S. Nakatsuji, and R. Matsunaga, Nat. Commun. **11**, 1 (2020).
[24] L. Zhang, C. Guo, C.-N. Kuo, H. Xu, K. Zhang, B. Ghosh, J. De Santis, D. W. Boukhvalov, I. Vobornik, V. Paolucci, C. S. Lue, H. Xing, A. Agarwal, L. Wang, and A. Politano, Phys. Status Solidi – Rapid Res. Lett. **15**, 2100212 (2021).
[25] R. Xie, T. Zhang, H. Weng, and G.-L. Chai, Small Sci. **2**, 2100106 (2022).
[26] C. Biz, M. Fianchini, and J. Gracia, ACS Catal. **11**, 14249 (2021).
[27] W. Mtangi, V. Kiran, C. Fontanesi, and R. Naaman, J. Phys. Chem. Lett. **6**, 4916 (2015).
[28] M. Brahlek, J. Lapano, and J. S. Lee, J. Appl. Phys. **128**, 210902 (2020).

[29] J. M. Kim, M. F. Haque, E. Y. Hsieh, S. M. Nahid, I. Zarin, K. Jeong, J. So, H. Park, and S. Nam, Adv. Mater. **2107362**, 2107362 (2022).
[30] P. Leubner, L. Lunczer, C. Brüne, H. Buhmann, and L. W. Molenkamp, Phys. Rev. Lett. **117**, 086403 (2016).
[31] D. Walkup, B. A. Assaf, K. L. Scipioni, R. Sankar, F. Chou, G. Chang, H. Lin, I. Zeljkovic, and V. Madhavan, Nat. Commun. **9**, 1550 (2018).
[32] A. K. Nayak, J. Reiner, R. Queiroz, H. Fu, C. Shekhar, B. Yan, C. Felser, N. Avraham, and H. Beidenkopf, Sci. Adv. **5**, 37 (2019).
[33] D. Du, S. Manzo, C. Zhang, V. Saraswat, K. T. Genser, K. M. Rabe, P. M. Voyles, M. S. Arnold, and J. K. Kawasaki, Nat. Commun. **12**, 2494 (2021).
[34] A. Barfuss, L. Dudy, M. R. Scholz, H. Roth, P. Höpfner, C. Blumenstein, G. Landolt, J. H. Dil, N. C. Plumb, M. Radovic, A. Bostwick, E. Rotenberg, A. Fleszar, G. Bihlmayer, D. Wortmann, G. Li, W. Hanke, R. Claessen, and J. Schäfer, Phys. Rev. Lett. **111**, 157205 (2013).
[35] G. N. Phan, K. Nakayama, K. Sugawara, T. Sato, T. Urata, Y. Tanabe, K. Tanigaki, F. Nabeshima, Y. Imai, A. Maeda, and T. Takahashi, Phys. Rev. B **95**, 1 (2017).
[36] L. A. Walsh and C. L. Hinkle, Appl. Mater. Today **9**, 504 (2017).
[37] D. Flötotto, Y. Bai, Y. H. Chan, P. Chen, X. Wang, P. Rossi, C. Z. Xu, C. Zhang, J. A. Hlevyack, J. D. Denlinger, H. Hong, M. Y. Chou, E. J. Mittemeijer, J. N. Eckstein, and T. C. Chiang, Nano Lett. **18**, 5628 (2018).
[38] S. Riccò, M. Kim, A. Tamai, S. McKeown Walker, F. Y. Bruno, I. Cucchi, E. Cappelli, C. Besnard, T. K. Kim, P. Dudin, M. Hoesch, M. J. Gutmann, A. Georges, R. S. Perry, and F. Baumberger, Nat. Commun. **9**, 4535 (2018).
[39] V. Sunko, E. Abarca Morales, I. Marković, M. E. Barber, D. Milosavljević, F. Mazzola, D. A. Sokolov, N. Kikugawa, C. Cacho, P. Dudin, H. Rosner, C. W. Hicks, P. D. C. King, and A. P. Mackenzie, Npj Quantum Mater. **4**, 46 (2019).
[40] C. Lin, M. Ochi, R. Noguchi, K. Kuroda, M. Sakoda, A. Nomura, M. Tsubota, P. Zhang, C. Bareille, K. Kurokawa, Y. Arai, K. Kawaguchi, H. Tanaka, K. Yaji, A. Harasawa, M. Hashimoto, D. Lu, S. Shin, R. Arita, S. Tanda, and T. Kondo, Nat. Mater. **20**, 1093 (2021).
[41] B. Burganov, C. Adamo, A. Mulder, M. Uchida, P. D. C. King, J. W. Harter, D. E. Shai, A. S. Gibbs, A. P. Mackenzie, R. Uecker, M. Bruetzam, M. R. Beasley, C. J. Fennie, D. G. Schlom, and K. M. Shen, Phys. Rev. Lett. **116**, 197003 (2016).
[42] J. P. Ruf, H. Paik, N. J. Schreiber, H. P. Nair, L. Miao, J. K. Kawasaki, J. N. Nelson, B. D. Faeth, Y. Lee, B. H. Goodge, B. Pamuk, C. J. Fennie, L. F. Kourkoutis, D. G. Schlom, and K. M. Shen, Nat. Commun. **12**, 59 (2021).
[43] T. Sands, C. J. Palmstrøm, J. P. Harbison, V. G. Keramidas, N. Tabatabaie, T. L. Cheeks, R. Ramesh, and Y. Silberberg, Mater. Sci. Reports **5**, 99 (1990).
[44] C. J. Palmstrøm, Annu. Rev. Mater. Sci. **25**, 389 (1995).
[45] C. C. Bomberger, M. R. Lewis, L. R. Vanderhoef, M. F. Doty, and J. M. O. Zide, J. Vac. Sci. Technol. B **35**, 030801 (2017).
[46] B. D. Schultz, S. G. Choi, and C. J. Palmstrøm, Appl. Phys. Lett. **88**, 243117 (2006).
[47] C. J. Palmstrøm, N. Tabatabaie, and S. J. Allen, Appl. Phys. Lett. **53**, 2608 (1988).
[48] C. J. Palmstrøm, S. Mounier, T. G. Finstad, and P. F. Miceli, Appl. Phys. Lett. **56**, 382 (1990).
[49] J. Nayak, S. C. Wu, N. Kumar, C. Shekhar, S. Singh, J. Fink, E. E. D. Rienks, G. H. Fecher, S. S. P. Parkin, B. Yan, and C. Felser, Nat. Commun. **8**, 13942 (2017).
[50] F. F. Tafti, Q. D. Gibson, S. K. Kushwaha, N. Haldolaarachchige, and R. J. Cava, Nat. Phys. **12**, 272 (2016).
[51] B. Schrunk, Y. Kushnirenko, B. Kuthanazhi, J. Ahn, L. L. Wang, E. O'Leary, K. Lee, A. Eaton, A. Fedorov, R. Lou, V. Voroshnin, O. J. Clark, J. Sánchez-Barriga, S. L. Bud'ko, R. J. Slager, P. C. Canfield, and A. Kaminski, Nature **603**, 610 (2022).
[52] S. Jang, R. Kealhofer, C. John, S. Doyle, J. Hong, J. H. Shim, Q. Si, O. Erten, J. D. Denlinger,

and J. G. Analytis, Sci. Adv. **5**, eaat7158 (2019).
[53] S. A. Solin, T. Thio, D. R. Hines, and J. J. Heremans, Science **289**, 1530 (2000).
[54] M. Holz, O. Kronenwerth, and D. Grundler, Phys. Rev. B **67**, 195312 (2003).
[55] H.-Y. Yang, T. Nummy, H. Li, S. Jaszewski, M. Abramchuk, D. S. Dessau, and F. Tafti, Phys. Rev. B **96**, 235128 (2017).
[56] J. Xu, N. J. Ghimire, J. S. Jiang, Z. L. Xiao, A. S. Botana, Y. L. Wang, Y. Hao, J. E. Pearson, and W. K. Kwok, Phys. Rev. B **96**, 075159 (2017).
[57] S. Chatterjee, S. Khalid, H. S. Inbar, A. Goswami, T. Guo, Y.-H. Chang, E. Young, A. V. Fedorov, D. Read, A. Janotti, and C. J. Palmstrøm, Sci. Adv. **7**, eabe8971 (2021).
[58] H. Inoue, M. Han, M. Hu, T. Suzuki, J. Liu, and J. G. Checkelsky, Phys. Rev. Mater. **3**, 101202(R) (2019).
[59] T. Schumann, M. Goyal, D. A. Kealhofer, and S. Stemmer, Phys. Rev. B **95**, 241113 (2017).
[60] X. Duan, F. Wu, J. Chen, P. Zhang, Y. Liu, H. Yuan, and C. Cao, Commun. Phys. **1**, 71 (2018).
[61] F. Fallah Tafti, Q. Gibson, S. Kushwaha, J. W. Krizan, N. Haldolaarachchige, and R. J. Cava, Proc. Natl. Acad. Sci. **113**, E3475 (2016).
[62] I. Aguilera, C. Friedrich, and S. Blügel, Phys. Rev. B **91**, 125129 (2015).
[63] V. Sandomirskiĭ, Sov. J. Exp. Theor. Phys. **25**, 101 (1967).
[64] T. Hirahara, T. Nagao, I. Matsuda, G. Bihlmayer, E. V. Chulkov, Y. M. Koroteev, and S. Hasegawa, Phys. Rev. B **75**, 035422 (2007).
[65] A. Takayama, T. Sato, S. Souma, T. Oguchi, and T. Takahashi, Nano Lett. **12**, 1776 (2012).
[66] P. Hofmann, Prog. Surf. Sci. **81**, 191 (2006).
[67] Z. Wu and J. Hao, Npj 2D Mater. Appl. **4**, 4 (2020).
[68] H. Du, X. Sun, X. Liu, X. Wu, J. Wang, M. Tian, A. Zhao, Y. Luo, J. Yang, B. Wang, and J. G. Hou, Nat. Commun. **7**, 10814 (2016).
[69] S. Ito, M. Arita, J. Haruyama, B. Feng, W.-C. Chen, H. Namatame, M. Taniguchi, C.-M. Cheng, G. Bian, S.-J. Tang, T.-C. Chiang, O. Sugino, F. Komori, and I. Matsuda, Sci. Adv. **6**, 1 (2020).
[70] T. Hirahara, T. Nagao, I. Matsuda, G. Bihlmayer, E. V. Chulkov, Y. M. Koroteev, P. M. Echenique, M. Saito, and S. Hasegawa, Phys. Rev. Lett. **97**, 146803 (2006).
[71] F. Schindler, Z. Wang, M. G. Vergniory, A. M. Cook, A. Murani, S. Sengupta, A. Y. Kasumov, R. Deblock, S. Jeon, I. Drozdov, H. Bouchiat, S. Guéron, A. Yazdani, B. A. Bernevig, and T. Neupert, Nat. Phys. **14**, 918 (2018).
[72] S. Ito, B. Feng, M. Arita, A. Takayama, R.-Y. Liu, T. Someya, W.-C. Chen, T. Iimori, H. Namatame, M. Taniguchi, C.-M. Cheng, S.-J. Tang, F. Komori, K. Kobayashi, T.-C. Chiang, and I. Matsuda, Phys. Rev. Lett. **117**, 236402 (2016).
[73] I. Aguilera, H.-J. Kim, C. Friedrich, G. Bihlmayer, and S. Blügel, Phys. Rev. Mater. **5**, L091201 (2021).
[74] S. Murakami, Phys. Rev. Lett. **97**, 236805 (2006).
[75] I. K. Drozdov, A. Alexandradinata, S. Jeon, S. Nadj-Perge, H. Ji, R. J. Cava, B. Andrei Bernevig, and A. Yazdani, Nat. Phys. **10**, 664 (2014).
[76] B. Jäck, Y. Xie, J. Li, S. Jeon, B. A. Bernevig, and A. Yazdani, Science **364**, 1255 (2019).
[77] T. Nagao, J. Sadowski, M. Saito, S. Yaginuma, Y. Fujikawa, T. Kogure, T. Ohno, Y. Hasegawa, S. Hasegawa, and T. Sakurai, Phys. Rev. Lett. **93**, 105501 (2004).
[78] S. Yaginuma, T. Nagao, J. T. Sadowski, M. Saito, K. Nagaoka, Y. Fujikawa, T. Sakurai, and T. Nakayama, Surf. Sci. **601**, 3593 (2007).
[79] F. Reis, G. Li, L. Dudy, M. Bauernfeind, S. Glass, W. Hanke, R. Thomale, J. Schäfer, and R. Claessen, Science **357**, 287 (2017).
[80] Y. Liu, S. Benter, C. S. Ong, R. P. Maciel, L. Björk, A. Irish, O. Eriksson, A. Mikkelsen, and R. Timm, ACS Nano **17**, 5047 (2023).
[81] P. J. Kowalczyk, O. Mahapatra, D. N. McCarthy, W. Kozlowski, Z. Klusek, and S. A. Brown, Surf. Sci. **605**, 659 (2011).

[82] S. A. Scott, M. V. Kral, and S. A. Brown, Surf. Sci. **587**, 175 (2005).
[83] Y. Lu, W. Xu, M. Zeng, G. Yao, L. Shen, M. Yang, Z. Luo, F. Pan, K. Wu, T. Das, P. He, J. Jiang, J. Martin, Y. P. Feng, H. Lin, and X. Wang, Nano Lett. **15**, 80 (2015).
[84] E. S. Walker, S. R. Na, D. Jung, S. D. March, J.-S. Kim, T. Trivedi, W. Li, L. Tao, M. L. Lee, K. M. Liechti, D. Akinwande, and S. R. Bank, Nano Lett. **16**, 6931 (2016).
[85] T. Shirasawa, M. Ohyama, W. Voegeli, and T. Takahashi, Phys. Rev. B **84**, 075411 (2011).
[86] T. Hirahara, G. Bihlmayer, Y. Sakamoto, M. Yamada, H. Miyazaki, S. Kimura, S. Blügel, and S. Hasegawa, Phys. Rev. Lett. **107**, 166801 (2011).
[87] T. Hirahara, N. Fukui, T. Shirasawa, M. Yamada, M. Aitani, H. Miyazaki, M. Matsunami, S. Kimura, T. Takahashi, S. Hasegawa, and K. Kobayashi, Phys. Rev. Lett. **109**, 227401 (2012).
[88] F. Yang, L. Miao, Z. F. Wang, M. Y. Yao, F. Zhu, Y. R. Song, M. X. Wang, J. P. Xu, A. V. Fedorov, Z. Sun, G. B. Zhang, C. Liu, F. Liu, D. Qian, C. L. Gao, and J. F. Jia, Phys. Rev. Lett. **109**, 1 (2012).
[89] L. Miao, M.-Y. Yao, W. Ming, F. Zhu, C. Q. Han, Z. F. Wang, D. D. Guan, C. L. Gao, C. Liu, F. Liu, D. Qian, and J.-F. Jia, Phys. Rev. B **91**, 205414 (2015).
[90] N. Fukui, T. Hirahara, T. Shirasawa, T. Takahashi, K. Kobayashi, and S. Hasegawa, Phys. Rev. B **85**, 115426 (2012).
[91] T. Shirasawa, J. Tsunoda, T. Hirahara, and T. Takahashi, Phys. Rev. B **87**, 075449 (2013).
[92] Y. M. Koroteev, G. Bihlmayer, E. V. Chulkov, and S. Blügel, Phys. Rev. B **77**, 045428 (2008).
[93] K.-H. Jin, H. W. Yeom, and F. Liu, Phys. Rev. B **101**, 035111 (2020).
[94] Y. Ohtsubo, L. Perfetti, M. O. Goerbig, P. Le Fèvre, F. Bertran, and A. Taleb-Ibrahimi, New J. Phys. **15**, 033041 (2013).
[95] K. Saito, H. Sawahata, T. Komine, and T. Aono, Phys. Rev. B **93**, 041301 (2016).
[96] Y. Ohtsubo and S. Kimura, New J. Phys. **18**, 123015 (2016).
[97] S. Chadov, X. Qi, J. Kübler, G. H. Fecher, C. Felser, and S. C. Zhang, Nat. Mater. **9**, 541 (2010).
[98] W. Al-Sawai, H. Lin, R. S. Markiewicz, L. A. Wray, Y. Xia, S.-Y. Xu, M. Z. Hasan, and A. Bansil, Phys. Rev. B **82**, 125208 (2010).
[99] H. Lin, L. A. Wray, Y. Xia, S. Xu, S. Jia, R. J. Cava, A. Bansil, and M. Z. Hasan, Nat. Mater. **9**, 546 (2010).
[100] T. Graf, C. Felser, and S. S. P. Parkin, Prog. Solid State Chem. **39**, 1 (2011).
[101] C. J. Palmstrøm, Prog. Cryst. Growth Charact. Mater. **62**, 371 (2016).
[102] Z. K. Liu, L. X. Yang, S.-C. Wu, C. Shekhar, J. Jiang, H. F. Yang, Y. Zhang, S.-K. Mo, Z. Hussain, B. Yan, C. Felser, and Y. L. Chen, Nat. Commun. **7**, 12924 (2016).
[103] R. Shan, S. Ouardi, G. H. Fecher, L. Gao, A. Kellock, K. P. Roche, M. G. Samant, C. E. Violbarbosa, E. Ikenaga, C. Felser, and S. S. P. Parkin, Appl. Phys. Lett. **102**, 172401 (2013).
[104] S. J. Patel, J. K. Kawasaki, J. Logan, B. D. Schultz, J. Adell, B. Thiagarajan, A. Mikkelsen, and C. J. Palmstrøm, Appl. Phys. Lett. **104**, 201603 (2014).
[105] S. Ouardi, C. Shekhar, G. H. Fecher, X. Kozina, G. Stryganyuk, C. Felser, S. Ueda, and K. Kobayashi, Appl. Phys. Lett. **98**, 211901 (2011).
[106] C. Liu, Y. Lee, T. Kondo, E. D. Mun, M. Caudle, B. N. Harmon, S. L. Bud'ko, P. C. Canfield, and A. Kaminski, Phys. Rev. B **83**, 205133 (2011).
[107] E. M. Seibel, L. M. Schoop, W. Xie, Q. D. Gibson, J. B. Webb, M. K. Fuccillo, J. W. Krizan, and R. J. Cava, J. Am. Chem. Soc. **137**, 1282 (2015).
[108] K. Manna, Y. Sun, L. Muechler, J. Kübler, and C. Felser, Nat. Rev. Mater. **3**, 244 (2018).
[109] S. Chatterjee, F. C. de Lima, J. A. Logan, Y. Fang, H. Inbar, A. Goswami, C. Dempsey, J. Dong, S. Khalid, T. Brown-Heft, Y.-H. Chang, T. Guo, D. J. Pennachio, N. Wilson, S. Chikara, A. Suslov, A. V. Fedorov, D. Read, J. Cano, A. Janotti, and C. J. Palmstrøm, Phys. Rev. Mater. **5**, 124207 (2021).
[110] J. K. Kawasaki, APL Mater. **7**, 080907 (2019).
[111] P. Larson, S. D. Mahanti, and M. G. Kanatzidis, Phys. Rev. B **62**, 12754 (2000).

[112] W. G. Zeier, J. Schmitt, G. Hautier, U. Aydemir, Z. M. Gibbs, C. Felser, and G. J. Snyder, Nat. Rev. Mater. **1**, 16032 (2016).
[113] M. A. Herman and H. Sitter, *Molecular Beam Epitaxy: Fundamentals and Current Status* (Springer Science \& Business Media, 2012).
[114] J. W. Orton and T. Foxon, *Molecular Beam Epitaxy: A Short History* (Oxford University Press, USA, 2015).
[115] H. Lüth, *Solid Surfaces, Interfaces and Thin Films*, 6th ed. (Springer Cham, 2015).
[116] W. Braun, *Applied RHEED: Reflection High-Energy Electron Diffraction during Crystal Growth* (Springer Science \& Business Media, 1999).
[117] S. Hasegawa, in *Charact. Mater.* (John Wiley & Sons, Inc., Hoboken, NJ, USA, 2012), pp. 1925–1938.
[118] Y. Horikoshi, Semicond. Sci. Technol. **8**, 1032 (1993).
[119] K. Alberi and M. A. Scarpulla, J. Phys. D. Appl. Phys. **51**, 023001 (2018).
[120] K. Jousten, F. Boineau, N. Bundaleski, C. Illgen, J. Setina, O. M. N. D. Teodoro, M. Vicar, and M. Wüest, Vacuum **179**, 109545 (2020).
[121] J. Y. Tsao, *Materials Fundamentals of Molecular Beam Epitaxy* (Academic Press, 2012).
[122] C. J. K. Richardson and M. L. Lee, MRS Bull. **41**, 193 (2016).
[123] J. H. Van Der Merwe, J. Appl. Phys. **34**, 117 (1963).
[124] J. W. Matthews and A. E. Blakeslee, J. Cryst. Growth **27**, 118 (1974).
[125] D. J. Dunstan, J. Mater. Sci. Mater. Electron. **8**, 337 (1997).
[126] R. Beanland, D. J. Dunstan, and P. J. Goodhew, Adv. Phys. **45**, 87 (1996).
[127] J. A. Sobota, Y. He, and Z.-X. Shen, Rev. Mod. Phys. **93**, 025006 (2021).
[128] S. Hüfner, *Photoelectron Spectroscopy* (Springer Berlin Heidelberg, Berlin, Heidelberg, 2003).
[129] A. Damascelli, Phys. Scr. **T109**, 61 (2004).
[130] S. Tanuma, C. J. Powell, and D. R. Penn, Surf. Interface Anal. **17**, 911 (1991).
[131] T.-C. Chiang, Surf. Sci. Rep. **39**, 181 (2000).
[132] M. Milun, P. Pervan, and D. P. Woodruff, Reports Prog. Phys. **65**, 99 (2002).
[133] J. A. Sobota, K. Kim, H. Takatsu, M. Hashimoto, S.-K. Mo, Z. Hussain, T. Oguchi, T. Shishidou, Y. Maeno, B. I. Min, and Z.-X. Shen, Phys. Rev. B **88**, 125109 (2013).
[134] N. V. Smith, Phys. Rev. B **32**, 3549 (1985).
[135] Thomas Ihn, *Semiconductor Nanostructures: Quantum States and Electronic Transport* (Oxford University Press, 2010).
[136] D. K. Schroder, *Semiconductor Material and Device Characterization*, 3rd ed. (John Wiley \& Sons, 2015).
[137] J. Lindemuth, *Hall Effect Measurement Handbook: A Fundamental Tool for Semiconductor Material Characterization* (Lake Shore Cryontronics, Incorporated, 2020).
[138] A. S. F76-08, in *Annu. B. ASTM Stand.*, 2016th ed. (ASTM International West Conshohocken, PA, 2011).
[139] N. D. M. Neil W. Ashcroft, in *Solid State Phys.*, 2022nd ed. (Cengage Learning, 1976).
[140] J. Hu and T. F. Rosenbaum, Nat. Mater. **7**, 697 (2008).
[141] D. X. Li, Y. Haga, H. Shida, T. Suzuki, Y. S. Kwon, and G. Kido, J. Phys. Condens. Matter **9**, 10777 (1997).
[142] D. X. Li, Y. Haga, H. Shida, T. Suzuki, and Y. S. Kwon, Phys. Rev. B **54**, 10483 (1996).
[143] E. M. Krivoy, S. Rahimi, H. P. Nair, R. Salas, S. J. Maddox, D. J. Ironside, Y. Jiang, V. D. Dasika, D. A. Ferrer, G. Kelp, G. Shvets, D. Akinwande, and S. R. Bank, Appl. Phys. Lett. **101**, 221908 (2012).
[144] N. L. Eatough and H. T. Hall, Inorg. Chem. **8**, 1439 (1969).
[145] H. Taub and S. J. Williamson, Solid State Commun. **13**, 1021 (1973).
[146] P. Li, Z. Wu, F. Wu, C. Cao, C. Guo, Y. Wu, Y. Liu, Z. Sun, C.-M. Cheng, D.-S. Lin, F. Steglich, H. Yuan, T.-C. Chiang, and Y. Liu, Phys. Rev. B **98**, 085103 (2018).

[147] T. J. Nummy, J. A. Waugh, S. P. Parham, Q. Liu, H.-Y. Yang, H. Li, X. Zhou, N. C. Plumb, F. F. Tafti, and D. S. Dessau, Npj Quantum Mater. **3**, 24 (2018).
[148] K. Kuroda, M. Ochi, H. S. Suzuki, M. Hirayama, M. Nakayama, R. Noguchi, C. Bareille, S. Akebi, S. Kunisada, T. Muro, M. D. Watson, H. Kitazawa, Y. Haga, T. K. Kim, M. Hoesch, S. Shin, R. Arita, and T. Kondo, Phys. Rev. Lett. **120**, 086402 (2018).
[149] S. Khalid, F. P. Sabino, and A. Janotti, Phys. Rev. B **98**, 220102 (2018).
[150] S. Khalid and A. Janotti, Phys. Rev. B **102**, 035151 (2020).
[151] B. D. Schultz, H. H. Farrell, M. M. R. Evans, K. Lüdge, and C. J. Palmstrøm, J. Vac. Sci. Technol. B Microelectron. Nanom. Struct. **20**, 1600 (2002).
[152] J. K. Kawasaki, R. Timm, K. T. Delaney, E. Lundgren, A. Mikkelsen, and C. J. Palmstrøm, Phys. Rev. Lett. **107**, 036806 (2011).
[153] E. M. Krivoy, A. P. Vasudev, S. Rahimi, R. A. Synowicki, K. M. McNicholas, D. J. Ironside, R. Salas, G. Kelp, D. Jung, H. P. Nair, G. Shvets, D. Akinwande, M. L. Lee, M. L. Brongersma, and S. R. Bank, ACS Photonics **5**, 3051 (2018).
[154] H. S. Inbar, D. Q. Ho, S. Chatterjee, M. Pendharkar, A. N. Engel, J. T. Dong, S. Khalid, Y. H. Chang, T. Guo, A. V. Fedorov, D. Lu, M. Hashimoto, D. Read, A. Janotti, and C. J. Palmstrøm, Phys. Rev. Mater. **6**, L121201 (2022).
[155] H. Yamada, T. Fukawa, T. Muro, Y. Tanaka, S. Imada, S. Suga, D.-X. Li, and T. Suzuki, J. Phys. Soc. Japan **65**, 1000 (1996).
[156] Z. Wu, F. Wu, P. Li, C. Guo, Y. Liu, Z. Sun, C. M. Cheng, T. C. Chiang, C. Cao, H. Yuan, and Y. Liu, Phys. Rev. B **99**, 035158 (2019).
[157] J. He, C. Zhang, N. J. Ghimire, T. Liang, C. Jia, J. Jiang, S. Tang, S. Chen, Y. He, S.-K. Mo, C. C. Hwang, M. Hashimoto, D. H. Lu, B. Moritz, T. P. Devereaux, Y. L. Chen, J. F. Mitchell, and Z.-X. Shen, Phys. Rev. Lett. **117**, 267201 (2016).
[158] Y. Wu, Y. Lee, T. Kong, D. Mou, R. Jiang, L. Huang, S. L. Bud'Ko, P. C. Canfield, and A. Kaminski, Phys. Rev. B **96**, 035134 (2017).
[159] J. K. Kawasaki, C. H. Kim, J. N. Nelson, S. Crisp, C. J. Zollner, E. Biegenwald, J. T. Heron, C. J. Fennie, D. G. Schlom, and K. M. Shen, Phys. Rev. Lett. **121**, 176802 (2018).
[160] N. Trivedi and N. W. Ashcroft, Phys. Rev. B **38**, 12298 (1988).
[161] T. Kasuya and D. X. Li, J. Magn. Magn. Mater. **166**, (1997).
[162] D. X. Li, Y. Haga, H. Shida, and T. Suzuki, J. Appl. Phys. **80**, 264 (1996).
[163] S. J. Allen, N. Tabatabaie, C. J. Palmstrøm, G. W. Hull, T. Sands, F. DeRosa, H. L. Gilchrist, and K. C. Garrison, Phys. Rev. Lett. **62**, 2309 (1989).
[164] S. Chatterjee, S. Khalid, H. S. Inbar, A. Goswami, F. C. de Lima, A. Sharan, F. P. Sabino, T. L. Brown-Heft, Y.-H. Chang, A. V Fedorov, D. Read, A. Janotti, and C. J. Palmstrøm, Phys. Rev. B **99**, 125134 (2019).
[165] D. D. Liang, Y. J. Wang, C. Y. Xi, W. L. Zhen, J. Yang, L. Pi, W. K. Zhu, and C. J. Zhang, APL Mater. **6**, 086105 (2018).
[166] J. Jiang, N. B. M. Schröter, S.-C. Wu, N. Kumar, C. Shekhar, H. Peng, X. Xu, C. Chen, H. F. Yang, C.-C. Hwang, S.-K. Mo, C. Felser, B. H. Yan, Z. K. Liu, L. X. Yang, and Y. L. Chen, Phys. Rev. Mater. **2**, 024201 (2018).
[167] Y. Wang, J. H. Yu, Y. Q. Wang, C. Y. Xi, L. S. Ling, S. L. Zhang, J. R. Wang, Y. M. Xiong, T. Han, H. Han, J. Yang, J. Gong, L. Luo, W. Tong, L. Zhang, Z. Qu, Y. Y. Han, W. K. Zhu, L. Pi, X. G. Wan, C. Zhang, and Y. Zhang, Phys. Rev. B **97**, 115133 (2018).
[168] J. M. Ziman, *Electrons and Phonons* (Oxford University Press, 2001).
[169] L. Ye, T. Suzuki, C. R. Wicker, and J. G. Checkelsky, Phys. Rev. B **97**, 081108 (2018).
[170] S. Chatterjee, S. Khalid, H. S. Inbar, A. Goswami, F. C. de Lima, A. Sharan, F. P. Sabino, T. L. Brown-Heft, Y. H. Chang, A. V Fedorov, D. Read, A. Janotti, and C. J. Palmstrøm, Phys. Rev. B **99**, 125134 (2019).
[171] P. D. C. King, T. D. Veal, and C. F. McConville, Phys. Rev. B **77**, 125305 (2008).

[172] R. Daou, A. Haase, M. Doerr, M. Rotter, F. Weickert, M. Nicklas, and F. Steglich, J. Phys. Conf. Ser. **273**, 012111 (2011).
[173] Y. Nakanishi, T. Sakon, M. Motokawa, M. Ozawa, and T. Suzuki, Phys. Rev. B **69**, 024412 (2004).
[174] G. Dwari, S. Sasmal, B. Maity, V. Saini, R. Kulkarni, and A. Thamizhavel, Http://Arxiv.Org/Abs/2111.13836 (2021).
[175] N. V. Kozlova, N. Mori, O. Makarovsky, L. Eaves, Q. D. Zhuang, A. Krier, and A. Patanè, Nat. Commun. **3**, (2012).
[176] H. Y. Yang, J. Gaudet, A. A. Aczel, D. E. Graf, P. Blaha, B. D. Gaulin, and F. Tafti, Phys. Rev. B **98**, (2018).
[177] P. Hohenberg and W. Kohn, Phys. Rev. **136**, B864 (1964).
[178] W. Kohn and L. J. Sham, Phys. Rev. **140**, A1133 (1965).
[179] P. E. Blöchl, Phys. Rev. B **50**, 17953 (1994).
[180] V. Popescu and A. Zunger, Phys. Rev. Lett. **104**, 236403 (2010).
[181] V. Popescu and A. Zunger, Phys. Rev. B **85**, 085201 (2012).
[182] P. M. C. Rourke and S. R. Julian, Comput. Phys. Commun. **183**, 324 (2012).
[183] G. Pizzi, V. Vitale, R. Arita, S. Blügel, F. Freimuth, G. Géranton, M. Gibertini, D. Gresch, C. Johnson, T. Koretsune, J. Ibañez-Azpiroz, H. Lee, J.-M. Lihm, D. Marchand, A. Marrazzo, Y. Mokrousov, J. I. Mustafa, Y. Nohara, Y. Nomura, L. Paulatto, S. Poncé, T. Ponweiser, J. Qiao, F. Thöle, S. S. Tsirkin, M. Wierzbowska, N. Marzari, D. Vanderbilt, I. Souza, A. A. Mostofi, and J. R. Yates, J. Phys. Condens. Matter **32**, 165902 (2020).
[184] F. F. Tafti, M. S. Torikachvili, R. L. Stillwell, B. Baer, E. Stavrou, S. T. Weir, Y. K. Vohra, H.-Y. Yang, E. F. McDonnell, S. K. Kushwaha, Q. D. Gibson, R. J. Cava, and J. R. Jeffries, Phys. Rev. B **95**, 014507 (2017).
[185] C. Q. Xu, B. Li, M. R. van Delft, W. H. Jiao, W. Zhou, B. Qian, N. D. Zhigadlo, D. Qian, R. Sankar, N. E. Hussey, and X. Xu, Phys. Rev. B **99**, 024110 (2019).
[186] M. Zhang, X. Wang, A. Rahman, R. Dai, Z. Wang, and Z. Zhang, Phys. Rev. B **101**, 064106 (2020).
[187] H. Inoue, M. Han, M. Hu, T. Suzuki, J. Liu, and J. G. Checkelsky, Phys. Rev. Mater. **3**, 101202 (2019).
[188] J. Kim, H.-S. Kim, and D. Vanderbilt, Phys. Rev. B **98**, 155122 (2018).
[189] C. Kadow, S. B. Fleischer, J. P. Ibbetson, J. E. Bowers, A. C. Gossard, J. W. Dong, and C. J. Palmstrøm, Appl. Phys. Lett. **75**, 3548 (1999).
[190] J. F. O'Hara, J. M. O. Zide, A. C. Gossard, A. J. Taylor, and R. D. Averitt, Appl. Phys. Lett. **88**, 251119 (2006).
[191] W. Kim, J. Zide, A. Gossard, D. Klenov, S. Stemmer, A. Shakouri, and A. Majumdar, Phys. Rev. Lett. **96**, 045901 (2006).
[192] H. Lu, P. G. Burke, A. C. Gossard, G. Zeng, A. T. Ramu, J.-H. Bahk, and J. E. Bowers, Adv. Mater. **23**, 2377 (2011).
[193] H. S. Inbar, D. Q. Ho, S. Chatterjee, A. N. Engel, S. Khalid, P. Connor, M. Pendharkar, Y. H. Chang, S. Nishihaya, A. V Fedorov, and D. Lu, ArXiv:2211.15806 (2023).
[194] B. R. York, Crit. Rev. Solid State Mater. Sci. **20**, 125 (1995).
[195] S. H. Mir, P. C. Jha, M. S. Islam, A. Banerjee, W. Luo, S. D. Dabhi, P. K. Jha, and R. Ahuja, Sci. Rep. **6**, 29309 (2016).
[196] C. Duan, R. F. Sabiryanov, J. Liu, W. N. Mei, P. A. Dowben, and J. R. Hardy, Phys. Rev. Lett. **94**, 237201 (2005).
[197] S. Klemenz, S. Lei, and L. M. Schoop, Annu. Rev. Mater. Res. **49**, 185 (2019).
[198] J. Heyd, G. E. Scuseria, and M. Ernzerhof, J. Chem. Phys. **118**, 8207 (2003).
[199] J. Heyd, G. E. Scuseria, and M. Ernzerhof, J. Chem. Phys. **124**, 219906 (2006).
[200] G. Kresse and J. Hafner, Phys. Rev. B **47**, 558 (1993).

[201] G. Kresse and J. Hafner, Phys. Rev. B **49**, 14251 (1994).
[202] M. N. Abdusalyamova, H. S. Shokirov, and O. I. Rakhmatov, J. Less Common Met. **166**, 221 (1990).
[203] D. Q. Ho, R. Hu, D. Q. To, G. W. Bryant, and A. Janotti, ArXiv: 2302.02049 (2023).
[204] R. S. K. Mong, A. M. Essin, and J. E. Moore, Phys. Rev. B **81**, 245209 (2010).
[205] C. Y.-P. Chao and S. L. Chuang, Phys. Rev. B **46**, 4110 (1992).
[206] Y. Sun, S. E. Thompson, and T. Nishida, J. Appl. Phys. **101**, 104503 (2007).
[207] F. Herman and S. Skillman, *Atomic Structure Calculations* (Prentice-Hall, Englewood Cliffs, New Jersey, 1963).
[208] J. C. Slater and G. F. Koster, Phys. Rev. **94**, 1498 (1954).
[209] R. P. Day, B. Zwartsenberg, I. S. Elfimov, and A. Damascelli, Npj Quantum Mater. **4**, 54 (2019).
[210] W. A. Harrison, *Electronic Structure and the Properties of Solids: The Physics of the Chemical Bond* (Dover Publications, 2012).
[211] Y. Q. Jia, J. Solid State Chem. **95**, 184 (1991).
[212] C. Schindler, S. Galeski, W. Schnelle, R. Wawrzyńczak, W. Abdel-Haq, S. N. Guin, J. Kroder, N. Kumar, C. Fu, H. Borrmann, C. Shekhar, C. Felser, T. Meng, A. G. Grushin, Y. Zhang, Y. Sun, and J. Gooth, Phys. Rev. B **101**, 125119 (2020).
[213] C.-G. Duan, R. F. Sabiryanov, W. N. Mei, P. A. Dowben, S. S. Jaswal, and E. Y. Tsymbal, Appl. Phys. Lett. **88**, 182505 (2006).
[214] W. Nolting and A. Ramakanth, *Quantum Theory of Magnetism* (Springer Berlin Heidelberg, Berlin, Heidelberg, 2009).
[215] J. Zaanen and G. A. Sawatzky, Can. J. Phys. **65**, 1262 (1987).
[216] J. J. Song, F. Tang, W. Zhou, Y. Fang, H. L. Yu, Z. D. Han, B. Qian, X. F. Jiang, D. H. Wang, and Y. W. Du, J. Mater. Chem. C **6**, 3026 (2018).
[217] H. Kępa, G. Springholz, T. M. Giebultowicz, K. I. Goldman, C. F. Majkrzak, P. Kacman, J. Blinowski, S. Holl, H. Krenn, and G. Bauer, Phys. Rev. B **68**, 024419 (2003).
[218] B. Biswas and B. Saha, Phys. Rev. Mater. **3**, 020301 (2019).
[219] F. Song, J. W. Wells, Z. Jiang, M. Saxegaard, and E. Wahlström, ACS Appl. Mater. Interfaces **7**, 8525 (2015).
[220] P. Zhang, P. Richard, T. Qian, Y.-M. Xu, X. Dai, and H. Ding, Rev. Sci. Instrum. **82**, 043712 (2011).
[221] H. S. Inbar, M. Zubair, J. T. Dong, A. N. Engel, C. P. Dempsey, Y. H. Chang, S. Nishihaya, S. Khalid, A. V Fedorov, A. Janotti, and others, ArXiv Prepr. ArXiv2302.00803 (2023).
[222] T.-R. Chang, Q. Lu, X. Wang, H. Lin, T. Miller, T.-C. Chiang, and G. Bian, Crystals **9**, 510 (2019).
[223] I. N. Yakovkin, J. Phys. Chem. Solids **129**, 277 (2019).
[224] M. Alcantara-Ortigoza and T. S. Rahman, ArXiv:2011.14879 1 (2020).
[225] J. T. Dong, H. S. Inbar, M. Pendharkar, T. A. J. van Schijndel, E. C. Young, C. P. Dempsey, and C. J. Palmstrøm, J. Vac. Sci. Technol. B **41**, (2023).
[226] S. Cho, Y.-H. Um, Y. Kim, G. K. L. Wong, J. B. Ketterson, and J.-I. Hong, J. Vac. Sci. Technol. A Vacuum, Surfaces, Film. **20**, 1191 (2002).
[227] J. Wever, H. L. Meyerheim, W. Moritz, V. Jahns, D. Wolf, H. Schulz, L. Seehofer, and R. L. Johnson, Surf. Sci. **321**, L225 (1994).
[228] H. Mönig, J. Sun, Y. M. Koroteev, G. Bihlmayer, J. Wells, E. V. Chulkov, K. Pohl, and P. Hofmann, Phys. Rev. B **72**, 085410 (2005).
[229] C. Liu, Y. Zhou, G. Wang, Y. Yin, C. Li, H. Huang, D. Guan, Y. Li, S. Wang, H. Zheng, C. Liu, Y. Han, J. W. Evans, F. Liu, and J. Jia, Phys. Rev. Lett. **126**, 176102 (2021).
[230] A. Kushima, X. Qian, P. Zhao, S. Zhang, and J. Li, Nano Lett. **15**, 1302 (2015).
[231] J. T. Dong, Unpublished (n.d.).
[232] Y. Eckstein, A. W. Lawson, and D. H. Reneker, J. Appl. Phys. **31**, 1534 (1960).

[233] G. Cantele and D. Ninno, Phys. Rev. Mater. **1**, 014002 (2017).
[234] S. Ito, B. Feng, M. Arita, T. Someya, W.-C. Chen, A. Takayama, T. Iimori, H. Namatame, M. Taniguchi, C.-M. Cheng, S.-J. Tang, F. Komori, and I. Matsuda, Phys. Rev. B **97**, 155423 (2018).
[235] L. Ö. Olsson, J. Kanski, L. Ilver, C. B. M. Andersson, M. Björkqvist, M. Göthelid, U. O. Karlsson, and M. C. Håkansson, Phys. Rev. B **50**, 18172 (1994).
[236] C. L. Littler and D. G. Seiler, Appl. Phys. Lett. **46**, 986 (1985).
[237] V. Hinkel, L. Sorba, and K. Horn, Surf. Sci. **194**, 597 (1988).
[238] J. P. Perdew, K. Burke, and M. Ernzerhof, Phys. Rev. Lett. **77**, 3865 (1996).
[239] U. Herath, P. Tavadze, X. He, E. Bousquet, S. Singh, F. Muñoz, and A. H. Romero, Comput. Phys. Commun. **251**, 107080 (2020).
[240] B. Liu, T. Wagner, S. Enzner, P. Eck, M. Kamp, G. Sangiovanni, and R. Claessen, Nano Lett. **23**, 3189 (2023).
[241] C. König, J. C. Greer, and S. Fahy, Phys. Rev. B **104**, 035127 (2021).
[242] A. Takayama, T. Sato, S. Souma, T. Oguchi, and T. Takahashi, Phys. Rev. Lett. **114**, 066402 (2015).
[243] Z.-Q. Huang, F.-C. Chuang, C.-H. Hsu, Y.-T. Liu, H.-R. Chang, H. Lin, and A. Bansil, Phys. Rev. B **88**, 165301 (2013).
[244] L. Apker, E. Taft, and J. Dickey, Phys. Rev. **76**, 270 (1949).
[245] C. König, J. C. Greer, and S. Fahy, Phys. Rev. B **104**, 045432 (2021).
[246] A. J. Mannix, B. Kiraly, M. C. Hersam, and N. P. Guisinger, Nat. Rev. Chem. **1**, 0014 (2017).
[247] M. Meinert, Phys. Rev. Lett. **116**, 26 (2016).
[248] T. Schwemmer, D. Di Sante, J. Schmalian, and R. Thomale, **1**, 1 (2022).
[249] F. F. Tafti, T. Fujii, A. Juneau-Fecteau, S. René De Cotret, N. Doiron-Leyraud, A. Asamitsu, and L. Taillefer, Phys. Rev. B **87**, 184504 (2013).
[250] H. Kim, K. Wang, Y. Nakajima, R. Hu, S. Ziemak, P. Syers, L. Wang, H. Hodovanets, J. D. Denlinger, P. M. R. Brydon, D. F. Agterberg, M. A. Tanatar, R. Prozorov, and J. Paglione, Sci. Adv. **4**, eaao4513 (2018).
[251] Y. Nakajima, R. Hu, K. Kirshenbaum, A. Hughes, P. Syers, X. Wang, K. Wang, R. Wang, S. R. Saha, D. Pratt, J. W. Lynn, and J. Paglione, Sci. Adv. **1**, e1500242 (2015).
[252] N. P. Butch, P. Syers, K. Kirshenbaum, A. P. Hope, and J. Paglione, Phys. Rev. B - Condens. Matter Mater. Phys. **84**, 1 (2011).
[253] S. D. Harrington, A. D. Rice, T. L. Brown-Heft, B. Bonef, A. Sharan, A. P. McFadden, J. A. Logan, M. Pendharkar, M. M. Feldman, O. Mercan, A. G. Petukhov, A. Janotti, L. Colakerol Arslan, and C. J. Palmstrøm, Phys. Rev. Mater. **2**, 1 (2018).
[254] H. Narita, Y. Niimi, T. Miyawaki, N. Tanaka, and H. Asano, Jpn. J. Appl. Phys. **54**, 093002 (2015).
[255] O. Polat, I. Mohelský, J. A. Arregi, M. Horák, J. Polčák, K. Bukvišová, J. Zlamal, and T. Sikola, Mater. Res. Bull. **149**, (2022).
[256] J. Kim, K. M. Fijalkowski, J. Kleinlein, C. Schumacher, A. Markou, C. Gould, S. Schreyeck, C. Felser, and L. W. Molenkamp, Phys. Rev. Mater. **7**, 024802 (2023).
[257] S. Khalid, H. S. Inbar, S. Chatterjee, C. J. Palmstrom, and A. Janotti, ArXiv: 2208.05415 (2022).
[258] M. K. Rajpalke, W. M. Linhart, K. M. Yu, M. Birkett, J. Alaria, J. J. Bomphrey, S. Sallis, L. F. J. Piper, T. S. Jones, M. J. Ashwin, and T. D. Veal, Appl. Phys. Lett. **105**, (2014).
[259] S. J. Patel, Growth and Electronic Structure of Heusler Compounds for Use in Electron Spin Based Devices, University of California, Santa Barbara, 2015.
[260] M. T. Vaughan, Thin Films Containing Heavy Group V Elements as Systems for Topological Materials, University of Leeds, 2020.
[261] T. Shirokura and P. N. Hai, AIP Adv. **12**, 125116 (2022).
[262] P. Dang, S. Rouvimov, H. G. Xing, and D. Jena, J. Appl. Phys. **126**, 103901 (2019).

[263] J. E. Saal, S. Kirklin, M. Aykol, B. Meredig, and C. Wolverton, Jom **65**, 1501 (2013).
[264] S. Kirklin, J. E. Saal, B. Meredig, A. Thompson, J. W. Doak, M. Aykol, S. Rühl, and C. Wolverton, Npj Comput. Mater. **1**, 1 (2015).
[265] G. B. Stringfellow, J. Appl. Phys. **43**, 3455 (1972).
[266] G. B. Stringfellow, J. Cryst. Growth **312**, 735 (2010).
[267] O. Nakatsuka, S. Fujinami, T. Asano, T. Koyama, M. Kurosawa, M. Sakashita, H. Kishida, and S. Zaima, Jpn. J. Appl. Phys. **56**, 01AB05 (2017).
[268] G. Vardar, S. W. Paleg, M. V. Warren, M. Kang, S. Jeon, and R. S. Goldman, Appl. Phys. Lett. **102**, 042106 (2013).
[269] B. Saha, A. Shakouri, and T. D. Sands, Appl. Phys. Rev. **5**, 021101 (2018).
[270] S. Khalid, A. Sharan, and A. Janotti, Phys. Rev. B **101**, 125105 (2020).
[271] R. G. Mani, L. Ghenim, and J. B. Choi, Phys. Rev. B **43**, 12630 (1991).
[272] H. M. Benia, C. Straßer, K. Kern, and C. R. Ast, Phys. Rev. B **91**, 161406 (2015).
[273] E. S. Walker, S. Muschinske, C. J. Brennan, S. R. Na, T. Trivedi, S. D. March, Y. Sun, T. Yang, A. Yau, D. Jung, A. F. Briggs, E. M. Krivoy, M. L. Lee, K. M. Liechti, E. T. Yu, D. Akinwande, and S. R. Bank, Phys. Rev. Mater. **3**, 064201 (2019).